



**COMPLEX FIELD ANALYSIS OF TEMPORAL AND
SPATIAL TECHNIQUES IN DIGITAL HOLOGRAPHIC
INTERFEROMETRY**

BY

CHEN HAO

(B. Eng)

A THESIS SUBMITTED

FOR THE DEGREE OF MASTER OF ENGINEERING

DEPARTMENT OF MECHANICAL ENGINEERING

NATIONAL UNIVERSITY OF SINGAPORE

2007

ACKNOWLEDGEMENTS

I would like to thank my supervisors **A/Prof. Quan Chenggen** and **A/Prof. Tay Cho Jui** for their advice and guidance throughout his research. I would like to take this opportunity to express my appreciation for their constant support and encouragement which have ensured the completion of this study.

Special thanks to all staffs of the Experimental Mechanics Laboratory. Their hospitality makes me enjoy my study in Singapore as an international student.

I would also like to thank my peer research students, who contribute to perfect research atmosphere by exchanging their ideas and experience.

My thanks also extend to my family for all their support.

Last but not least, I wish to thank National University of Singapore for providing a research scholarship which makes this study possible.

TABLE OF CONTENTS

ACKNOWLEDGEMENTS		i
TABLE OF CONTENTS		ii
SUMMARY		v
NOMENCALTURE		vii
LIST OF FIGURES		ix
LIST OF TABLES		xiii
CHAPTER 1	INTRODUCTION	1
1.1	Background	1
1.2	The Scope of work	6
1.3	Thesis outline	7
CHAPTER 2	LITERATURE REVIEW	8
2.1	Foundations of holography	8
2.1.1	Hologram recording	8
2.1.2	Optical reconstruction	10
2.2	Holographic interferometry (HI)	11
2.3	Digital holography (DH)	14
2.3.1	Types of digital holography	15
2.3.1.1	General Principles	15
2.3.1.2	Reconstruction by the Fresnel Approximation	16
2.3.1.3	Digital Fourier holography	18
2.3.1.4	Phase shifting digital holography	19
2.4	Digital holographic interferometry	22
2.5	Phase unwrapping	22
2.5.1	Spatial Phase Unwrapping	23
2.5.2	Temporal Phase Unwrapping	24
2.6	Temporal phase unwrapping of digital holograms	24
2.7	Short time Fourier transform (STFT)	26

2.7.1	An introduction to STFT	26
2.7.2	STFT in optical metrology	27
2.7.2.1	Filtering by STFT	28
2.7.2.1	Ridges by STFT	28
CHAPTER 3	THEORY OF COMPLEX FIELD ANALYSIS	30
3.1	D.C.-term of the Fresnel transform	30
3.2	Spatial frequency requirements	34
3.3	Deformation measurement by HI	39
3.4	Shape measurement by HI	41
3.5	Temporal phase unwrapping algorithm	42
3.6	Complex field analysis	42
3.7	Temporal phase retrieval from complex field	41
3.7.1	Temporal Fourier transform	41
3.7.2	Temporal STFT analysis	47
3.7.2.1	Temporal filtering by STFT	47
3.7.2.2	Temporal phase extraction from a ridge	48
3.7.2.3	Window Selection	51
3.7.3	Spatial phase retrieval from a complex field	54
3.7.4	Combination of temporal phase retrieval and spatial phase retrieval	57
CHAPTER 4	DEVELOPMENT OF EXPERIMENTATION	58
4.1	Equipment for dynamic measurement	58
4.1.1	High speed camera	58
4.1.2	PZT translation stage	59
4.1.3	Stepper motor travel linear stage	60
4.1.4	Specimens	61
4.2	Equipment for Static Measurement	63
4.2.1	High resolution digital still camera	63
4.2.2	Specimen	63
4.3	Experimental setup	64
4.3.1	Multi-illumination method	64

4.3.2	Measurement of continuously deforming object	64
CHAPTER 5	RESULTS AND DISCUSSION	67
5.1	D.C-term removal	68
5.2	Spatial CP method	71
5.3	Temporal CP method in dynamic measurement	75
5.3.1	Surface profiling on an object with step change	75
5.3.2	Measurements on continuously deforming object	83
5.3.3	A comparison of three temporal CP algorithms	89
CHAPTER 6	CONCLUSIONS AND FUTURE WORK	97
6.1	Conclusions	97
6.2	Future work	99
REFERENCES		101
APPENDICES		108
A.	SHORT TIME FOURIER TRANSFORM RIDGES	108
B.	C++ SOURCE CODE FOR TEMPORAL RIDGE	112
ALGORITHM		
C.	LIST OF PUBLICATIONS DURING M.ENG PERIOD	118

SUMMARY

In this thesis, a novel concept of complex phasor method to process the digital holographic interference phase maps in complex field is proposed. Based on this concept, three temporal phase retrieval algorithms and one spatial retrieval approach are developed. Temporal complex phasor method is highly immune to noise and allows accurate measurement of dynamic object. A series of digital holograms is recorded by a high-speed camera during the continuously illumination changing or deformation process of the tested specimen. Each digital hologram is numerically reconstructed in the computer instead of optically, thus a sequence of complex-valued interference phase maps are obtained by the proposed concept. The complex phasor variation of each pixel is measured and analyzed along the time axis.

The first temporal complex phasor algorithm based on Fourier transform is specially developed for dynamic measurement in which the phase is linearly dependent on time. By transforming the sequence of complex phasors into frequency domain, the peak corresponding to the rate of phase changing is readily picked up. The algorithm works quite well even when the data is highly noise-corrupted. But the requirement on linear changing phase constrains its real application.

The short time Fourier transform (STFT) which is highly adaptive to exponential field is employed to develop the second and third algorithms. The second algorithm also transforms the sequence of complex phasors into frequency domain, and discards coefficients whose amplitude is lower than preset threshold. The filtered coefficients are inverse transformed. Due to the local transformation, bad data has no effect on data beyond the window width, which is a great improvement over the global transform, e.g.

Fourier transform. Another advantage of STFT is that it is able to tell when or where certain frequency components exist. The instantaneous frequency retrieval of the complex phasor variation of a pixel is therefore possible by the maximum modulus-the ridge-of a STFT coefficient. The continuous interference phase is then obtained by integration. It is possible to calculate the first derivative of the measured physical quantity using this method, e.g. velocity in deformation measurement.

To demonstrate the validity of proposed temporal and spatial methods, two dynamic experiments and one static experiment are conducted: the profiling of surface with height step, instantaneous velocity and deformation measurement of continuously deforming object and deformation measurement of an aluminum plate. The commonly used method of directly processing phase values in digital holographic interferometry is employed for comparison. It is observed that the proposed methods give a better performance.

The complex phasor processing as proposed in this study demonstrates a high potential for robust processing of continuous sequence of images. The study on different temporal phase analysis techniques will broaden the applications in optical, nondestructive testing area, and offer more precise results and bring forward a wealth of possible research directions.

NOMENCLATURE

E	Electrical field form of light waves
a	Real of amplitude of light wave
φ	The phase of light wave
I	Intensity of light wave
h	Amplitude transmission
$\Delta\varphi$	Interference phase
Γ	Complex field of light wave
d	Distance between object and hologram plane
Re	Real part of a complex function
Im	Imaginary part of a complex function
$\Delta\xi$	Pixel size along x direction
$\Delta\eta$	Pixel size along y direction
f_{\max}	Maximum spatial frequency
θ_{\max}	Maximum angle between object and reference wave
δ	Optical path length difference
Sf	Short time Fourier transform
$P_s f$	Spectrogram of short time Fourier transform
ξ	Spatial frequency along x direction
η	Spatial frequency along y direction
A	Complex field by conjugate multiplication

$\Delta\varphi_w$	Wrapped interference phase
\mathfrak{F}	Fourier transform
$\Delta\varphi'$	First derivative of interference phase
T_x	Time width of signal
B_x	Frequency domain bandwidth
g_{TBP}	Optimized window

LIST OF FIGURES

Fig. 2.1	Schematic layout of the hologram recording setup	9
Fig. 2.2	Schematic layout of optical reconstruction	10
Fig. 2.3	Recording of a double exposure hologram	12
Fig. 2.4	Reconstruction	13
Fig. 2.5	Coordinate system for numerical hologram reconstruction	15
Fig. 2.6	Digital lensless Fourier holography	19
Fig. 2.7	Phase shifting digital holography	20
Fig. 2.8	Procedure for temporal phase unwrapping of digital holograms (Pedrini et al., 2003)	25
Fig. 2.9	Phase retrieval from phase-shifted fringes: (a) one of four phase-shifted fringe patterns; (b) phase by phase-shifting technique and (c) phase by WFR (Qian, 2007)	29
Fig. 2.10	WFR for strain extraction: (a) Original moiré fringe pattern; (b) strain contour in x direction using moiré of moiré technique and (c) strain field by WFR (Qian, 2007)	29
Fig. 3.1	A reconstructed intensity distribution by Fresnel transform without clipping	30
Fig. 3.2	Digital lensless Fourier holography	34
Fig. 3.3	Spatial frequency spectra of an off-axis holography	36
Fig. 3.4	Geometry for recording an off-axis digital Fresnel hologram	37
Fig. 3.5	Geometry for recording an off-axis digital lensless Fourier hologram	38
Fig. 3.6	Schematic illustration of the angle between the object wave and reference wave in digital lensless Fourier holography setup (Wagner et al., 1999)	38
Fig. 3.7	Sensitivity vector for digital holographic interferometric measurement of displacement	40

Fig. 3.8	Two-illumination point contouring	41
Fig. 3.9	A linearly changing phase	45
Fig. 3.10	The spectrum of a complex phasor with linearly changing phase	45
Fig. 3.11	Comparison of STFT resolution: (a) a better time solution; (b) a better frequency solution	52
Fig. 3.12	Spectrograms with different window width: (a) 25 ms; (b) 125 ms; (c) 375 ms; (d) 1000 ms	54
Fig. 3.13	Unfiltered interference phase distribution	55
Fig. 3.14	(a) Effect of filtering a phasor image; (b) effect of sine/cosine transformation	56
Fig. 3.15	Flow chart of (a) conventional method (b) proposed method	57
Fig. 4.1	Kodak Motion Corder Analyzer, Monochrome Model SR-Ultra	59
Fig. 4.2	PZT translation stage (Piezosystem Jena, PX 300 CAP) and its controller	60
Fig. 4.3	Newport UTM 150 mm mid-range travel steel linear stage	60
Fig. 4.4	Melles Griot 17 MDU 002 NanoStep Motor Controller	61
Fig. 4.5	(a) Dimension of a step-change object; (b) top view of the specimen with step-change.	61
Fig. 4.6	(a) A cantilever beam and its loading device; (b) Schematic description of loading process and inspected area	62
Fig. 4.7	Pulnix TM-1402	63
Fig. 4.8	A circular plate centered loaded	63
Fig. 4.9	Optical arrangement for profile measurement using multi-illumination-point method	65
Fig. 4.10	Digital holographic setup for dynamic deformation measurement	66
Fig. 5.1	A typical digital hologram	68
Fig. 5.2	Intensity display of a reconstruction with D.C.-term eliminated	69
Fig. 5.3	Intensity distribution display of reconstruction: (a) with average	

	value subtraction only; (b) with high-pass filter only	69
Fig. 5.4	(a) digital hologram in digital lensless Fourier holography; (b) Its corresponding intensity display of reconstruction with D.C.-term eliminated	70
Fig. 5.5	Intensity display of reconstruction: (a) with average value subtraction; (b) with high-pass filter only	70
Fig. 5.6	Process flow of digital holographic interferometry	72
Fig. 5.7	Spatial phase unwrapping	73
Fig. 5.8	Spatial phase retrieval by CP method	74
Fig. 5.9	Digital hologram in surface profiling experiment (particles are highlighted by circles)	75
Fig. 5.10	Reconstruction of Figure 5.9	76
Fig. 5.11	DPS method	77
Fig. 5.12	(a) Wrapped phase for a given point; (b) Unwrapped phase for a given point	79
Fig. 5.13	(a) Unwrapped phase; (b) corresponding 3D plot	79
Fig. 5.14	(a) Phase variation of a pixel; (b) intensity variation of a pixel	80
Fig. 5.15	Frequency spectrum of a pixel	80
Fig. 5.16	Unwrapped phase by integration	80
Fig. 5.17	Results calculated by temporal Fourier transform algorithm: (a) unwrapped phase; (b) 3D plot	81
Fig. 5.18	Result for a pixel by temporal STFT filtering: (a) Wrapped phase; (b) Unwrapped phase	82
Fig. 5.19	Results calculated temporal STFT filtering algorithm: (a) unwrapped phase; (b) 3D plot	82
Fig. 5.20	Triangular wave by PZT stage	84
Fig. 5.21	Digital hologram and its intensity display of reconstruction	84
Fig. 5.22	Interference phase variations with time	85
Fig. 5.23	Schematic description of temporal phase unwrapping of digital	

	holograms	86
Fig. 5.24	A typical interference phase pattern of the cantilever beam	86
Fig. 5.25	Unwrapped phase by DPS method	86
Fig. 5.26	(a) Instantaneous velocity of point B using numerical differentiation of unwrapped phase difference; (b) Instantaneous velocity of points A, B and C by proposed ridge algorithm	88
Fig. 5.27	Flow chart of instantaneous velocity calculation using CP method	90
Fig. 5.28	2D distribution and 3D plots of instantaneous velocity at various instants	91
Fig. 5.29	Displacement of point B: (a) by temporal phase unwrapping of wrapped phase difference using DPS method; (b) by temporal phase unwrapping of wrapped phase difference from $t = 0.4s$ to $t = 0.8s$ using DPS method; (c) by integration of instantaneous velocity using CP method; (d) by integration of instantaneous velocity from $t = 0.4s$ to $t = 0.8s$ using CP method	93
Fig. 5.30	3D plot of displacement distribution at various instants. (a), (c), (e) by integration of instantaneous velocity using CP method; (b), (d), (f) by temporal phase unwrapping using DPS method	94

LIST OF TABLES

Table 5.1	A comparison of different temporal algorithms from CP concept	96
-----------	---	----

CHAPTER ONE

INTRODUCTION**1.1 Background**

Dennis Gabor (1948) invented holography as a lensless means for image formation by reconstructed wavefronts. He created the word holography from the Greek words ‘holo’ meaning whole and ‘graphein’ meaning to write. It is a clever method of combining interference and diffraction for recording the reconstructing the whole information contained in an optical wavefront, namely, amplitude and phase, not just intensity as conventional photography does. A wavefield scattered from the object and a reference wave interferes at the surface of recording material, and the interference pattern is photographically or otherwise recorded. The information about the whole three-dimensional wave field is coded in form of interference stripes usually not visible for the human eye due to the high spatial frequencies. By illuminating the hologram with the reference wave again, the object wave can be reconstructed with all effects of perspective and depth of focus.

Besides the amazing display of three-dimensional scenes, holography has found numerous applications due to its unique features. One major application is Holographic Interferometry (HI), discovered by Stetson (1965) in the late sixties of last century. Two or more wave fields are compared interferometrically, with at least one of them is holographically recorded and reconstructed. Traditional interferometry has the most stringent limitation that the object under investigation be optically smooth, however, HI removes such a limitation. Therefore, numerous papers indicating new general

theories and applications were published following Stetsons' publication. Thus HI not only preserves the advantages of interferometric measurement, such as high sensitivity and non-contacting field view, but also extends to the investigation of numerous materials, components and systems previously impossible to measure by classical optical method. The measurement of the changes of phase of the wavefield and thus the change of any physical quantity that affects the phase are made possible by such a technique. Applications ranged from the first measurement of vibration modes (Powell and Stetson, 1965), over deformation measurement (Haines and Hilderbrand, 1966a), (1966b), contour measurement (Haines and Hilderbrand, 1965), (Heflinger, 1969), to the determination of refractive index changes (Horman, 1965), (Sweeney and Vest, 1973).

The results from HI are usually in the form of fringe patterns which can be interpreted in a first approximation as contour lines of the amplitude of the change of the measured quantity. For example, a locally higher deformation results in a locally higher fringe density. Besides this qualitative evaluation expert interpretation is needed to convert these fringes into desired information. In early days, fringes were manually counted, later on interference patterns were recorded by video cameras (nowadays CCD or CMOS cameras) for digitization and quantization. Interference phases are then calculated from those stored interferograms, with initially developed algorithms resembling the former fringe counting. The introduction of the phase shifting methods of classic interferometric metrology into HI was a big step forward, making it possible to measure the interference phase between the fringe intensity maxima and minima and at the same time resolving the sign ambiguity. However, extra experimental efforts were required for the increased accuracy. Fourier transform evaluation (Kreris, 1986)

is an alternative without the need for generating several phase shifted interferograms and without the need to introduce a carrier (Taketa et al., 1982).

While holographic interferograms were successfully evaluated by computer, the fabrication of the interference pattern was still a clumsy work. The wet chemical processing of the photographic plates, photothermoplastic film, photorefractive crystals, and other recording media all had their inherent drawbacks. With the development of computer technology, it was possible to transfer either the recording process or reconstruction process into the computer. Such an endeavor led to the first resolution: Computer Generated Holography (Lee, 1978), which generates holograms by numerical method. Afterwards these computer generated holograms are reconstructed optically.

Goodman and Lawrence (1967) proposed numerical hologram reconstruction and later followed by Yaroslavski et al. (1972). They sampled optically enlarged parts of in-line and Fourier holograms recorded on a photographic plate and reconstructed these digitized conventional holograms. Onural and Scott (1987, 1992) improved the reconstruction algorithm and used this approach for particle measurement.

Direct recording of Fresnel holograms with CCD by Schnars (1994) was a significant step forward, which enables full digital recording and processing of holograms, without the need of photographic recording as an intermediate step. Later on the term **Digital Holography (DH)** was accepted in the optical metrology community for this method. Although it is already a known fact that numerically the complex wave field can be reconstructed by digital holograms, previous experiments (Goodman and Lawrence, 1967) (Yaroslavski et al, 1972) concentrated only on intensity distribution. It is the realization of the potential of the digitally reconstructed

phase distribution that led to digital holographic interferometry (Schnars, 1994). The phases of stored wave fields can be accessed directly once the reconstruction is done using digitally recorded holograms, without any need for generating phase-shifted interferograms. In addition, other techniques of interferometric optical metrology, such as shearography or speckle photography, can be derived numerically from digital holography. Sharing the advantages of conventional optical holographic interferometry, DH also has its own distinguished features:

- No such strict requirements as conventional holography on vibration and mechanical stability during recording, for CCD sensors have much higher sensitivity within the working wavelength than that of photographic recording media.
- Reconstruction process is done by computers, no need for time-consuming wet chemical processing and a reconstruction setup.
- Direct phase accessibility. High quality interference phase distributions are available easily by simply subtraction between phases of different states. Therefore, avoiding processing of often noise disturbed intensity fringe patterns.
- Complete description of wavefield, not only intensity but also phase is available. Thus a more flexible way to simulate physical procedures with numerical algorithms. What is more, powerful image processing algorithms can be used for better reconstructed results.

Digital holography (DH) is much more than a simple extension of conventional optical holography to digital version. It offers great potentials for non-destructive measurement and testing as well as 3D visualization. Employing CCD sensors as recording media, DH is able to digitalize and quantize the optical information of holograms. The reconstruction and metrological evaluations are all accomplished by

computers with corresponding numerical algorithms. It simplifies both the system configuration and evaluation procedure for phase determination, which requires much more efforts, both experimentally and mathematically. Digital holography can now be a more competing and promising technique for interferometric measurement in industrial applications, which are unimaginable for the traditional optical holography.

In experimental mechanics, high precision 3D displacement measurement of object subject to impact loading and vibration is an area of great interest and is one of the most appealing applications of DH. Those displacement results can later be used to access engineering parameters such as strain, vibration amplitude and structural energy flow. Only a single hologram needs to be recorded in one state and the transient deformation field can be obtained quite easily by comparing wavefronts of different states interferometrically. In addition, there is no need at all for the employment of troublesome phase-shifting (Huntley et al., 1999) or a temporal carrier (Fu et al., 2005) to determine the phase unambiguously. By employing a pulsed laser, fast dynamic displacements can be recorded quite easily, provided that each pulse effectively freezes the object movement. Such a combination of DH and a pulsed ruby laser has been reported for: vibration measurements (Pedrini et al., 1997), shape measurements (Pedrini et al., 1999), defect recognition (Schedin et al., 2001) and dynamic measurements of rotating objects (Perez-lopez, 2001). However, this technique has its own limitation. An experiment has to be repeated several times before the evolution of the transient deformation can be obtained, each time with a different delay. Problems will arise when an experiment is difficult to repeat. Due to the rapid development of CCD and CMOS cameras speed, it is now possible to record speckle patterns with rates exceeding 10,000 frames per second. Therefore, one solution to those problems is to record a sequence of holograms during the whole process (Pedrini, 2003).

The quantitative evaluation of the resulting fringe pattern is usually done by carrying out spatial phase unwrapping. However, it suffers an inherent drawback that absolute phase values are not available. Phase value relative to some other point is what it all can achieve. In addition, large phase errors will be generated if the pixels of the wrapped interference phase map are not well modulated. An alternative is the one dimensional approach to unwrap along the time axis was proposed by Huntley (1993). Each pixel of the camera acts as an independent sensor and the phase unwrapping is done for each pixel in the time domain. Such kind of method is particularly useful when processing speckle patterns, and can avoid the spatial prorogation of phase errors. In addition, temporal phase unwrapping allows absolute phase value to be obtained, which is impossible by spatial phase unwrapping.

1.2 The Scope of work

The scope of this dissertation work is focused on temporal phase retrieval techniques combined with digital holographic interferometry and applying them for dynamic measurement. Specifically, (1) Study the mechanisms and properties of digital holography with emphasis on dynamic measurement; (2) Propose a novel complex field processing method; (3) Develop three temporal phase retrieval algorithms using powerful time-frequency tools based on the proposed method; (4) Compare spatial filtering techniques using the proposed method with commonly used ones; (5) Verify those proposed methods, algorithms and techniques with different digital holographic interferometric experiments.

1.3 Thesis outline

An outline of the thesis is as follows:

Chapter 1 provides an introduction of this dissertation.

Chapter 2 reviews the foundations of optical and digital holography. In digital holographic interferometry, the basis of the two-illumination-point method for surface profiling and deformation measurement are discussed. This chapter also discusses the advantage of digital holographic interferometry's application to dynamic measurement.

Chapter 3 presents the theory of the proposed complex phasor method, under which the temporal Fourier analysis, temporal STFT filtering, temporal ridge algorithm are developed.

Chapter 4 describes the practical aspects of a dynamic phase measurement. The setups are described.

Chapter 5 compares the results obtained by the conventional and proposed methods. The advantages, disadvantages and accuracy of the proposed methods are analyzed in detail.

Chapter 6 summarizes this project work and shows potential development on dynamic measurements.

CHAPTER TWO

LITERATURE REVIEW

2.1 Foundations of holography**2.1.1 Hologram recording**

An optical setup composed of a light source (laser), mirrors and lenses to guide beam and a recording device, e. g. a photographic plate is usually used to record holograms. A typical setup (Schnars, 2005) is shown in Figure 2.1. A laser beam with sufficient coherence length is split into two parts by a beam splitter. One part of the wave illuminates the object, scattered and reflected to the recording medium. The other one acting as the reference wave illuminates the light sensitive medium directly. Both waves interfere. The resulting interference pattern is recorded and chemically developed.

The complex amplitude of the object wave is described by

$$E_o(x, y) = a_o(x, y) \exp[i\varphi_o(x, y)] \quad (2.1)$$

with real amplitude a_o and phase φ_o .

$$E_r(x, y) = a_r(x, y) \exp[i\varphi_r(x, y)] \quad (2.2)$$

is the complex amplitude of the reference wave with real amplitude a_r and phase φ_r .

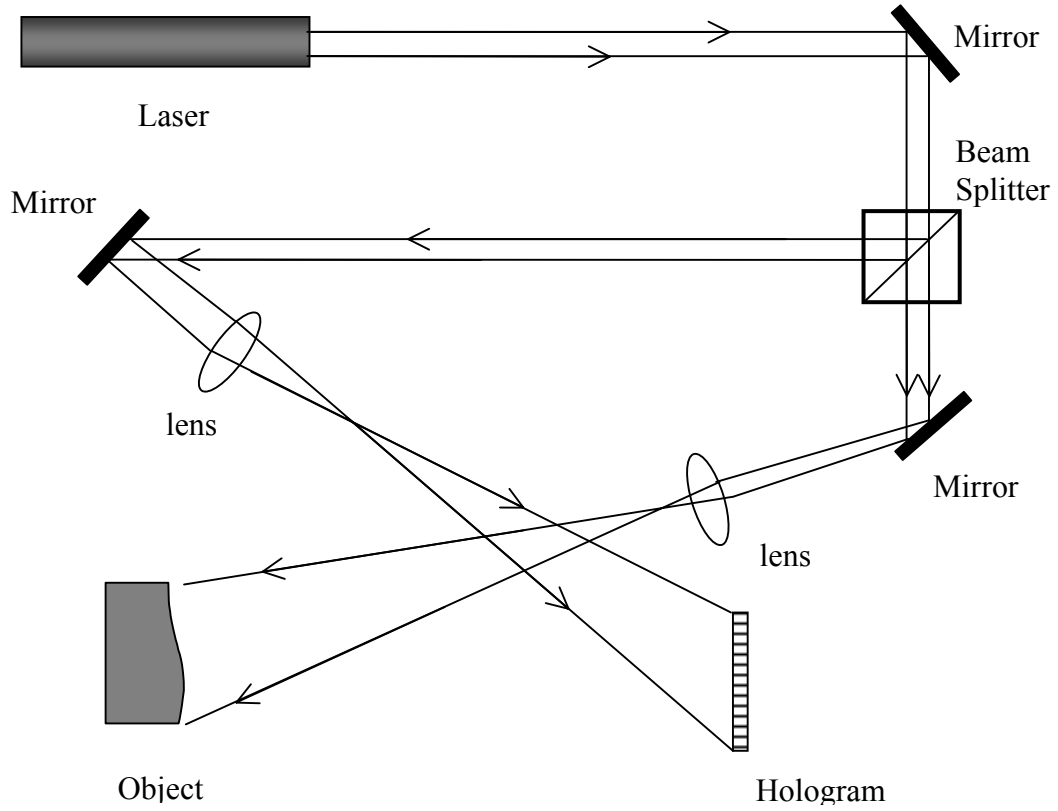


Figure 2.1 Schematic layout of the hologram recording setup

Both waves interfere at the surface of the recording medium. The intensity is given as

$$\begin{aligned}
 I(x, y) &= |E_O(x, y) + E_R(x, y)|^2 \\
 &= [E_O(x, y) + E_R(x, y)][E_O^*(x, y) + E_R^*(x, y)] \\
 &= a_O^2(x, y) + a_R^2(x, y) + E_O(x, y)E_R^*(x, y) + E_O^*(x, y)E_R(x, y)
 \end{aligned} \tag{2.3}$$

The amplitude transmission $h(x, y)$ of the developed photographic plated is proportional to $I(x, y)$:

$$h(x, y) = h_0 + \beta\tau I(x, y) \tag{2.4}$$

The constant β is the slope of the amplitude transmittance versus exposure characteristic of the light sensitive material. τ is the exposure time and h_0 is the amplitude transmission of the unexposed plate.

2.1.2 Optical reconstruction

The developed photographic plate is illuminated by the reference wave E_R , as shown in Figure 2.2, for optical reconstruction of the object wave. This gives a modulation of the reference wave by the transmission $h(x, y)$:

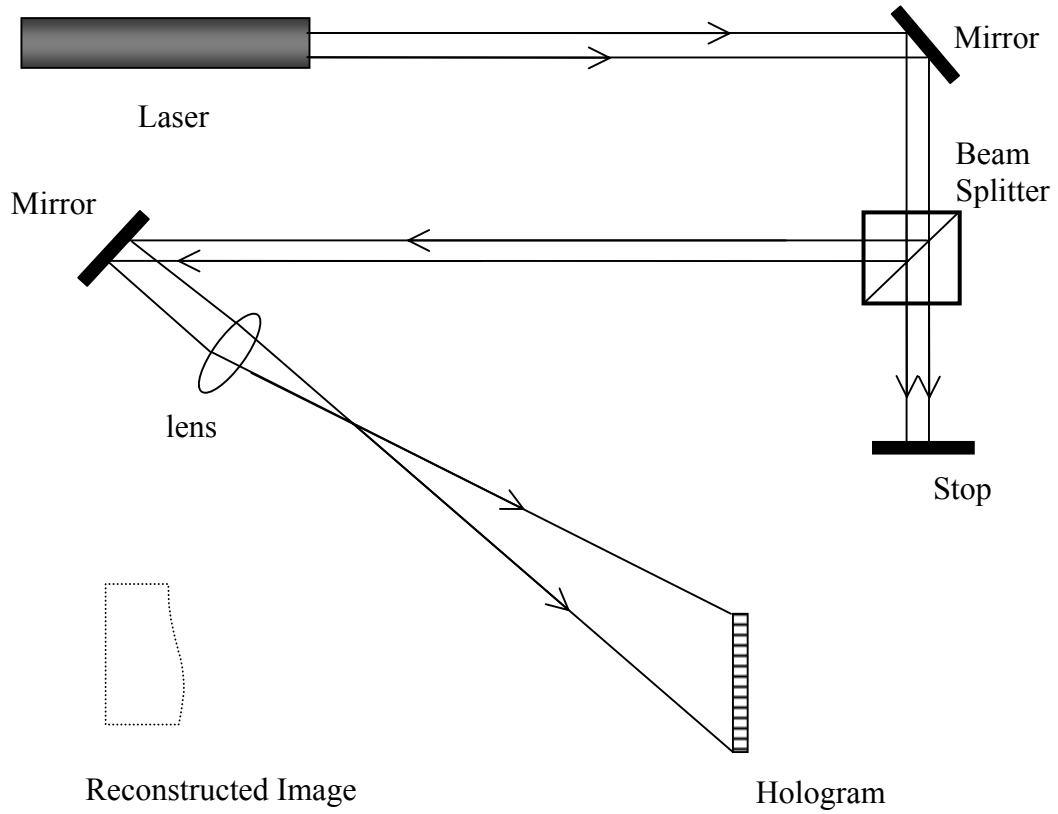


Figure 2.2 Schematic layout of optical reconstruction

$$E_R(x, y)h(x, y) = \left[h_0 + \beta\tau(a_R^2 + a_O^2) \right] E_R(x, y) + \beta\tau a_R^2 E_O(x, y) + \beta\tau E_R^2(x, y) E_O^*(x, y) \quad (2.5)$$

The first term on the right side of the equation is the zero diffraction order, it is just the reference wave multiplied with the mean transmittance. The second term is the reconstructed object wave, forming the virtual image. The factor before it only influences the brightness of the image. The third term produces a distorted real image of the object.

2.2 Holographic interferometry (HI)

By holographic recording and reconstruction of a wave field, it is possible to compare such a wave field interferometrically either with a wave field scattered directly by the object, or with another holographically reconstructed wave field. HI is defined as the interferometric comparison of two or more wave fields, at least one of which is holographically reconstructed (Vest, 1979). HI is a non-contact, non-destructive method with very high sensitivity. The resolution is able to reach up to one hundredth of a wavelength.

Only slight differences between the wave fields to be compared by holographic interferometry are allowed:

1. The same microstructure of object is demanded;
2. The geometry for all wave fields to be compared must be the same;
3. The wavelength and coherence for optical laser radiation used must be stable enough;
4. The change of the object to be measured should be in a small range.

In double exposure method of HI, two wave fields scattered from the same object in two different states are recorded consecutively by the same recording media

(Sollid and Swint, 1970), shown in Figure 2.3. The first exposure corresponds to initial state of object while the second the state of object after a physical parameter changes.

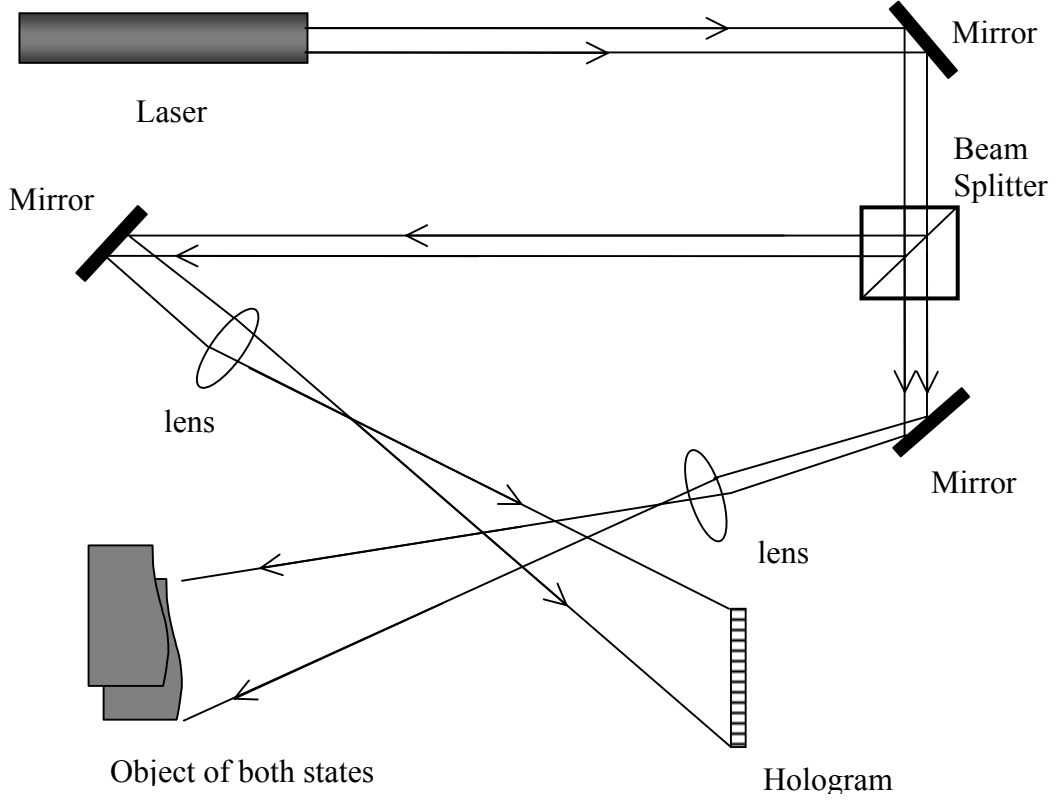


Figure 2.3 Recording of a double exposure hologram

The complex amplitude of the object wave in its initial state is:

$$O_1 = o(x, y) \exp[i\varphi(x, y)] \quad (2.6)$$

where $o(x, y)$ is the real amplitude and $\varphi(x, y)$ the phase distribution of the object wave. Due to the microstructure of the diffusely reflecting or refracting object, $\varphi(x, y)$ changes randomly in space. The variation of the physical parameter to be measured leads to a change of the phase distribution from $\varphi(x, y)$ to $\varphi + \Delta\varphi$. $\Delta\varphi$ referred to interference phase, describes the difference between the initial state and the changed state. The complex amplitude of second state is therefore given as:

$$O_2 = o(x, y) \exp \left\{ i \left[\varphi(x, y) + \Delta\varphi(x, y) \right] \right\} \quad (2.7)$$

We illuminate the developed photographic plate with the reference wave E_R , both recorded wave fields are reconstructed simultaneously, as shown in Figure 2.4.

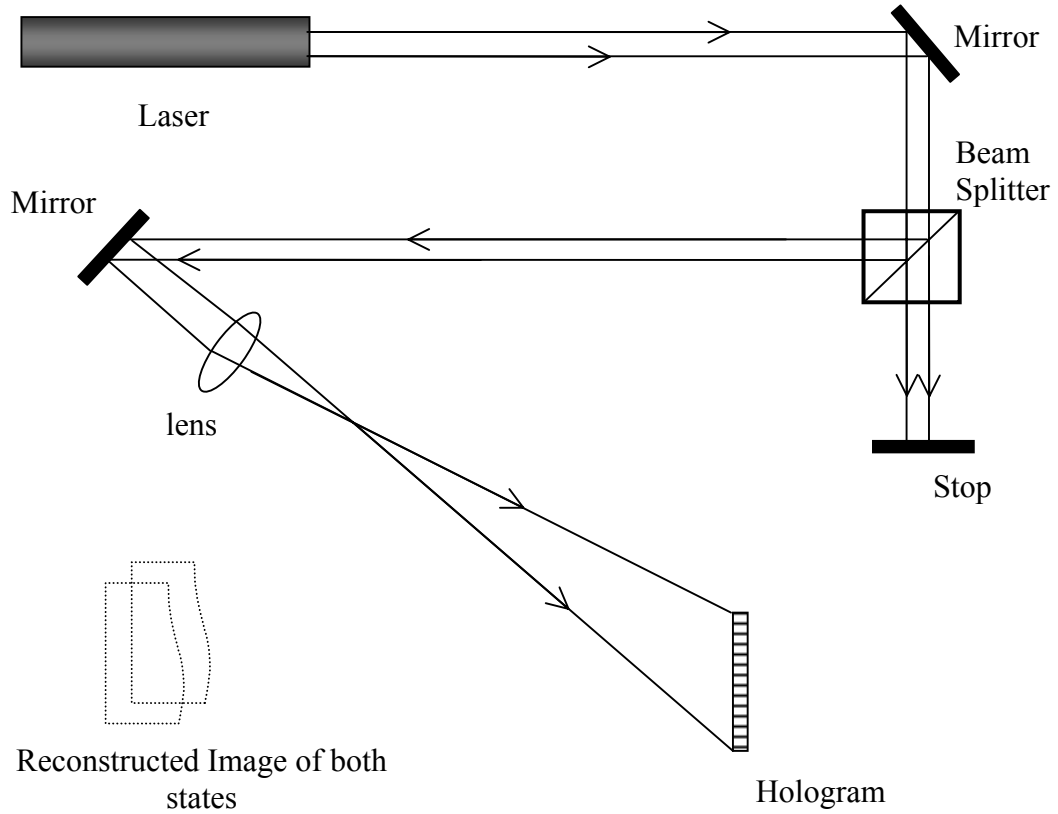


Figure 2.4 Reconstruction

They interfere and result in a stationary intensity distribution:

$$\begin{aligned} I(x, y) &= |O_1 + O_2|^2 = (O_1 + O_2)(O_1 + O_2)^* \\ &= 2o^2 [1 + \cos(\Delta\varphi)] \end{aligned} \quad (2.8)$$

Therefore the general expression for the intensity of an interference pattern is:

$$I(x, y) = A(x, y) + B(x, y) \cos \Delta\varphi(x, y) \quad (2.9)$$

It is generally impossible to calculate $\Delta\varphi$ directly from the recorded intensity, for the items $A(x, y)$ and $B(x, y)$ are unknown. What's more the cosine is an even function and the sign of $\Delta\varphi$ cannot be determined unambiguously. Therefore several techniques have been introduced to calculate the interference phase with the help of additional information. The most commonly used method of them is phase shifting.

2.3 Digital holography (DH)

In spite of the obvious advantages, classic holographic interferometry has always been regarded as a tool only applicable in laboratories. The reasons are as follows: First, the strong stability requirement of optical holography becomes the obstacle for industrial environments unless pulsed lasers are employed. Second, the photographic recording and the following chemical developments makes the on-line inspection very difficult due to the annoying time delays. Third, optical reconstruction has to be done in optical setup, for the case of real-time measurement, the exact repositioning of holographic plates after chemical development is required. Last, one thing is still missing in optical holography: the phase of the object wave could be reconstructed optically, however, not be measured directly. With respect to dynamic measurement, optical holography appears quite clumsy.

The last huge step to the complete access of the object wave was digital holography. An exciting new tool to measure, store, transmit, manipulate those electromagnetical wave fields in the computer. In digital holography, the holographic image is replaced by a CCD-target, at the surface of which the reference wave and the object wave are interfering. The resulting hologram is digitally sampled and transferred to the computer by the framegrabber. The digital hologram is reconstructed

solely in the computer by diffraction theory and numerical algorithms. The relatively troublesome process of developing and replacing of a photographic plate is no longer needed.

2.3.1 Types of digital holography

2.3.1.1 General Principles

Let the geometry for the numerical description be as in Figure 2.5. The CCD target with the coordinates (ξ, η) has a distance d apart from the object surface.

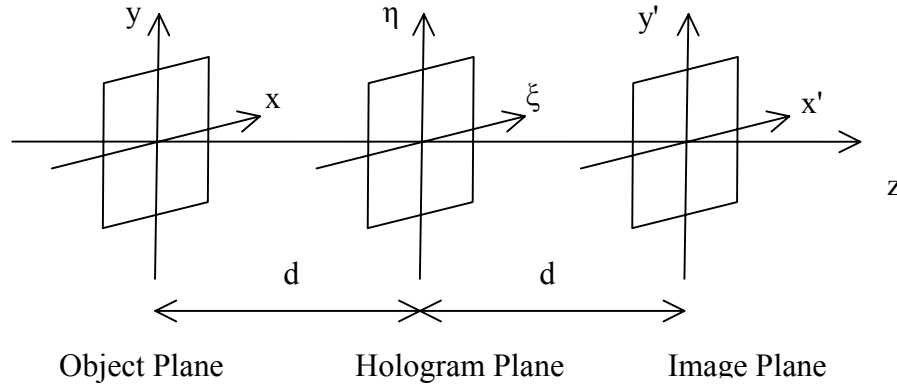


Figure 2.5 Coordinate system for numerical hologram reconstruction

The image plane where the real image can be reconstructed is also d away from hologram plane. This plane has the coordinates of (x', y') . A hologram with the intensity distribution $h(\xi, \eta)$ is produced by the interference of object wave and the reference wave $E_R(\xi, \eta)$ at the surface of the CCD target. Then $h(\xi, \eta)$ is quantized and digitized to be stored in the computer.

The diffracted wave field in the image plane is given by Fresnel-Kirchhoff integral (Goodman, 1996):

$$\Gamma(x', y') = \frac{i}{\lambda} \int_{-\infty}^{+\infty} \int_{-\infty}^{+\infty} h(\xi, \eta) E_R(\xi, \eta) \frac{\exp\left(-i \frac{2\pi}{\lambda} \rho'\right)}{\rho'} dx dy \quad (2.10)$$

with

$$\rho' = \sqrt{(x' - \xi)^2 + (y' - \eta)^2 + d^2} \quad (2.11)$$

ρ' is the distance between a point in the hologram plane and a point in the reconstruction plane. Eq. (2.10) is the basis for numerical hologram reconstruction. It can be seen that the reconstructed wave field $\Gamma(x', y')$ is a complex function, from which both the intensity as well as the phase can be calculated (Schnars, 1993). This is a huge improvement over the optical holography in which only the intensity is visible. The direct phase access makes up a real advantage when coming to digital holographic interferometry.

Two different approaches (Kreis and Jüptner, 1997) have been introduced for the numerical solution of Eq. (2.10). In Fresnel-approximation, ρ' in the denominator is replaced by the distance d , which is valid when the distance d is large compared with CCD chip size. Another approach making use of the convolution theorem considers the integral as a convolution. It was first applied by Demetrakopoulos and Mittra (1974) for numerical reconstruction of sub optical holograms for the first time. Later Kreis (1997) applied this method to optical holography. Only the Fresnel-approximation will be treated in this study along with conditions that, if fulfilled, can simplify calculations.

2.3.1.2 Reconstruction by the Fresnel Approximation

The expression of Eq. (2.11) can be expanded to a Taylor series:

$$\rho' = d + \frac{(\xi - x')^2}{2d} + \frac{(\eta - y')^2}{2d} - \frac{1}{8} \frac{[(\xi - x')^2 + (\eta - y')^2]^2}{d^3} + \dots \quad (2.12)$$

The fourth item can be neglected, if it is small compared to the wavelength (Klein and Furtak, 1986). Then the distance ρ' consists of linear and quadratic terms:

$$\rho' = d + \frac{(\xi - x')^2}{2d} + \frac{(\eta - y')^2}{2d} \quad (2.13)$$

A further approximation of replacing the denominator in Eq. (2.10) by d gives rise to the following expression for reconstruction of a real image:

$$\begin{aligned} \Gamma(x', y') &= \frac{i}{\lambda d} \exp\left(-i \frac{2\pi}{\lambda} d\right) \exp\left[i \frac{\pi}{\lambda d} (x'^2 + y'^2)\right] \\ &\times \int_{-\infty}^{+\infty} \int_{-\infty}^{+\infty} E_R(\xi, \eta) h(\xi, \eta) \exp\left[i \frac{\pi}{\lambda d} (\xi^2 + \eta^2)\right] \exp\left[i \frac{2\pi}{\lambda d} (x' \xi + y' \eta)\right] d\xi d\eta \end{aligned} \quad (2.14)$$

This equation is called Fresnel approximation or Fresnel transformation because of the mathematical similarity between the Fourier Transform and itself.

The intensity is calculated by squaring:

$$I(x', y') = |\Gamma(x', y')|^2 \quad (2.15)$$

The phase is calculated by arctan:

$$\varphi(x', y') = \arctan \frac{\text{Im}[\Gamma(x', y')]}{\text{Re}[\Gamma(x', y')]} \quad (2.16)$$

where Re denotes the real part while Im the imaginary part. Assuming the hologram function $h(\xi, \eta)$ is sampled on a CCD target of $M \times N$ points with steps $\Delta\xi \times \Delta\eta$

along the coordinates. With these discrete values the integral of (2.14) converts to finite sums (Schnars and Jüptner, 2005):

$$\begin{aligned} \Gamma(m, n) = & \frac{i}{\lambda d} \exp\left(-i \frac{2\pi}{\lambda} d\right) \exp\left[i\pi\lambda d \left(\frac{m^2}{M^2\Delta\xi^2} + \frac{n^2}{N^2\Delta\eta^2}\right)\right] \\ & \times \sum_{k=0}^{M-1} \sum_{l=0}^{N-1} E_R(k, l) h(k, l) \exp\left[i \frac{\pi}{\lambda d} (k^2\Delta\xi^2 + l^2\Delta\eta^2)\right] \exp\left[i2\pi\left(\frac{km}{M} + \frac{ln}{N}\right)\right] \end{aligned} \quad (2.17)$$

It can be seen that Eq. (2.17) is a discrete inverse Fourier transform of $E_R(k, l)$ multiplied by $h(k, l)$ and $\exp\left[i\pi/(\lambda d)(k^2\Delta\xi^2 + l^2\Delta\eta^2)\right]$. This calculation is done most effectively by the Fast Fourier Transform (FFT) algorithm. The factor in front of the sum only affects the overall phase and can therefore be neglected if only the intensity is of concerned.

2.3.1.3 Digital Fourier holography

Digital lensless Fourier holography has been realized by Wagner et al. (1999). The specialty of lensless Fourier holography lies in the fact that the point source of the spherical reference wave is located in the same plane with the object. The reference wave at the CCD plane is therefore described as:

$$\begin{aligned} E_R(\xi, \eta) = & \frac{\exp\left(-i \frac{2\pi}{\lambda} \sqrt{d^2 + \xi^2 + \eta^2}\right)}{\sqrt{d^2 + \xi^2 + \eta^2}} \\ & \approx \frac{1}{d} \exp\left(-i \frac{2\pi}{\lambda} d\right) \exp\left[-i \frac{\pi}{\lambda d} (\xi^2 + \eta^2)\right] \end{aligned} \quad (2.18)$$

Digital lensless Fourier holography recording setup is shown in Figure 2.6.

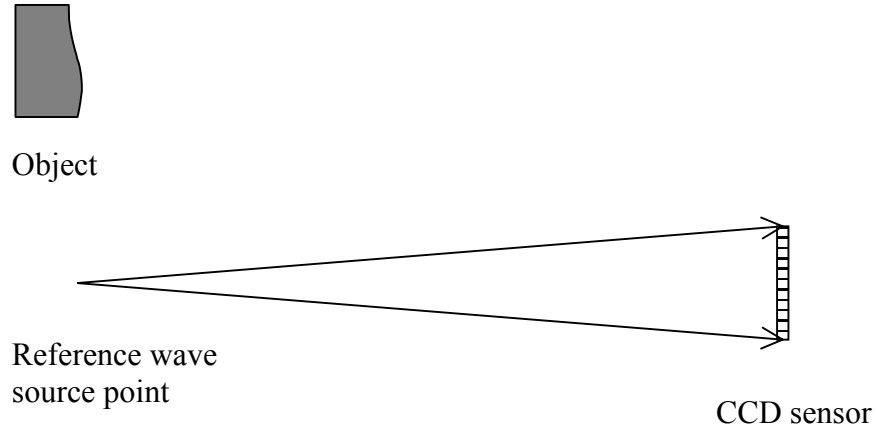


Figure 2.6 Digital lensless Fourier holography

The approximation used here is the same as the one used in the derivation of Fresnel transform. Inserting Eq. (2.18) into Eq. (2.14) results in following expression:

$$\Gamma(x', y') = C \exp \left[+i \frac{\pi}{\lambda d} (x'^2 + y'^2) \right] \mathfrak{F}^{-1} [h(\xi, \eta)] \quad (2.19)$$

where C denotes constant. Digital lensless Fourier holography has a simpler reconstruction algorithm. However, it loses the ability to refocus, as the reconstruction distance d does not appear.

2.3.1.4 Phase shifting digital holography

By using the methods described above, we can reconstruct the complex amplitude of the object wave field from a single hologram. However, Skarman (1994), (1996) proposed a completely different method. He employed a phase shifting method to calculate the initial complex amplitude and thus the complex amplitude in any plane can be calculated using the Fresnel-Kirchhoff formulation of diffraction. Later this phase shifting method was improved and applied to opaque by Yamaguchi et al. (1997), (2001), and (2002).

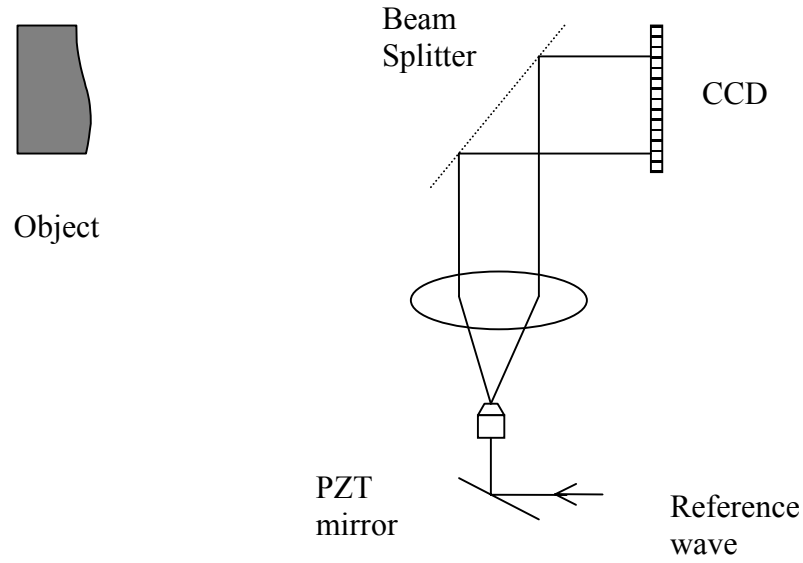


Figure 2.7 Phase shifting digital holography

The principal setup for phase shifting digital holography is illustrated in Figure 2.7. A mirror mounted on a piezoelectric transducer (PZT) guides the reference wave and shifts the phase of the reference with step. The object phase φ_0 is calculated from these phase shifted interferograms recorded by the CCD camera. As to the real amplitude a_0 of the object wave, it can be measured from the intensity by blocking the reference wave.

The complex amplitude of the object wave is therefore determined:

$$E_o(\xi, \eta) = a_o(\xi, \eta) \exp[i\varphi_o(\xi, \eta)] \quad (2.20)$$

The complex amplitude in the image plane is calculated using Eq. (2.14):

$$E_o(x', y') = C \exp\left[\frac{i\pi}{\lambda d}(x'^2 + y'^2)\right] \times \int_{-\infty}^{+\infty} \int_{-\infty}^{+\infty} E_o(\xi, \eta) \exp\left[\frac{i\pi}{\lambda d}(\xi^2 + \eta^2)\right] \exp\left[i\frac{2\pi}{\lambda d}(x'\xi + y'\eta)\right] d\xi d\eta \quad (2.21)$$

Now that we know the complex amplitude in the hologram plane, we can then invert the recording process to reconstruct the object wave (Seebacher, 2001).

Hologram recording process is described:

$$E_o(\xi, \eta) = \frac{i}{\lambda} \int_{-\infty}^{+\infty} \int_{-\infty}^{+\infty} E_o(x, y) \frac{\exp\left(-i \frac{2\pi}{\lambda} \sqrt{d^2 + (x - \xi)^2 + (y - \eta)^2}\right)}{\sqrt{d^2 + (x - \xi)^2 + (y - \eta)^2}} dx dy \quad (2.22)$$

$$= \mathfrak{I}^{-1} \left\{ \mathfrak{I} [E_o(x, y)] \cdot \mathfrak{I} [g(x, y, \xi, \eta)] \right\}$$

with

$$g(x, y, \xi, \eta) = \frac{i}{\lambda} \frac{\exp\left[-i \frac{2\pi}{\lambda} \sqrt{d^2 + (x - \xi)^2 + (y - \eta)^2}\right]}{\sqrt{d^2 + (x - \xi)^2 + (y - \eta)^2}} \quad (2.23)$$

$E_o(x, y)$ is the complex amplitude of the object wave. By inversion of Eq. (2.22), it can be calculated directly:

$$E_o(x, y) = \mathfrak{I}^{-1} \left\{ \frac{\mathfrak{I} [E_o(\xi, \eta)]}{\mathfrak{I} [g(x, y, \xi, \eta)]} \right\} \quad (2.24)$$

The advantage of phase shifting digital holography is a reconstructed image of the object free of the D.C term and the twin image. Additional experimental efforts are needed to achieve this: phase shifted interferograms have to be generated and recorded. Thus such a method restricts itself to the measurement of slowly varying phenomena with constant phase during the recording cycle.

2.4 Digital holographic interferometry

Instead of the optical reconstruction of a double exposure hologram and an evaluation of the resulting intensity pattern, the reconstructed phase fields can now be compared directly (Schnars, 1994) in digital holography. The cumbersome and error prone computer-aided evaluation methods to determine the interference phase from intensity patterns are out of date. Sign correct interference phases are obtained with minimum noise, high resolution, and an experimental effort significantly less than any phase shifting methods (Kreis, 2005).

In each state of the object, one digital hologram is recorded. Those digital holograms are then reconstructed separately using the reconstruction algorithms above. From the resulting complex amplitudes $\Gamma_1(x, y)$ and $\Gamma_2(x, y)$ the phase distributions are obtained:

$$\varphi_1(x, y) = \arctan \frac{\text{Im}\Gamma_1(x, y)}{\text{Re}\Gamma_1(x, y)} \quad (2.25)$$

$$\varphi_2(x, y) = \arctan \frac{\text{Im}\Gamma_2(x, y)}{\text{Re}\Gamma_2(x, y)} \quad (2.26)$$

where the index 1 denotes the first state and index 2 the second state. The interference phase is then determined in a pointwise manner by a modulo 2π subtraction:

$$\Delta\varphi = \begin{cases} \varphi_1 - \varphi_2 & \text{if } \varphi_1 \geq \varphi_2 \\ \varphi_1 - \varphi_2 + 2\pi & \text{if } \varphi_1 < \varphi_2 \end{cases} \quad (2.27)$$

2.5 Phase unwrapping

The previous sections show that the interference phase by digital holographic interferometry is indefinite to an additive multiple of 2π , i. e. it is wrapped modulo

2π . The processing of converting the interference phase modulo 2π into a continuous phase distribution is called phase unwrapping. This can be defined in the following expression (Creath, et al. 1993):

“Phase unwrapping is the process by which the absolute value of the phase angle of a continuous function that extends over a range of more than 2π (relative to a predefined starting point) is recovered. This absolute value is lost when the phase term is wrapped upon itself with a repeat distance of 2π due to the fundamental sinusoidal nature of the wave function (electromagnetic radiation) used in the measurement of physical properties.”

2.5.1 Spatial Phase Unwrapping

The unwrapping process consists, in one way or another, in comparing pixels or groups of pixels to detect and remove the 2π phase jumps. Numerous approaches have been proposed to process single wrapped phase maps (Ghiglia and Pritt, 1998), such as branch cut method (Just et al. 1995), quality-guided path following algorithm (Bone, 1991), mask cut algorithm (Priti et al. 1990), minimum discontinuity approach (Flynn, 1996), cellular automata (Ghiglia et al. 1987), neural networks and so on. They all have their own advantages and disadvantages, emphasizing the fact again that no single tool is able to solve all the problems (Robinson and Reid, 1993).

This process also involves kinds of problems, in particular if the wrapped phase map contains lots of noises. Generally, a proper filtering of the wrapped phase map can greatly improve the results. However, if the object contains physical discontinuities such as the abrupt step change on an object in shape measurement, or cracks of the object surface in deformation measurement, phase unwrapping will result in the propagation of errors. This problem also arises when fringes are in unconnected zones.

Another inherent disadvantage of such a method is that only relative phase values can be obtained, and no absolute measurement is possible.

2.5.2 Temporal Phase Unwrapping

The algorithms mentioned above are “spatial” algorithms in the sense that a phase map is unwrapped by comparing adjacent pixels or pixel regions within a single image. An alternative approach was proposed by Huntley and Saldner (1993) where the unwrapping process is carried out along the time axis. A series of interferograms are recorded and each pixel of the camera acts as an independent sensor. This procedure is particularly useful for an important subclass of interferometric applications where a series of incremental phase maps can be obtained. The advantages of such a procedure are obvious: First, erroneous phase values do not propagate spatially within a single image. Second, physical discontinuities can be dealt with automatically. The isolated regions can be correctly unwrapped, without any uncertainty concerning their relative phase order. Third, it allows the absolute phase values to be obtained. Although it suffers the limitation that the experiment has to be conducted step by step and may introduce loading problem, this novel concept leads to a family of phase extraction methods-temporal analysis techniques.

2.6 Temporal phase unwrapping of digital holograms

As mentioned in the introduction chapter, digital holographic interferometry is highly suitable for dynamic measurement. An interesting combination of digital holographic interferometry with temporal phase unwrapping to measure absolute deformation of the object has been reported (Pedrini et al., 2003). Figure 2.8 shows the procedure.

Such a method offers a unique advantage to determine unambiguously the direction of motion over the most commonly employed temporal digital speckle pattern interferometry that uses one dimensional Fourier transform (Joenathan et al., 1998a), (Joenathan et al., 1998b). In addition, it also avoids the troublesome phase-shifting (Huntley, 1999) technique which requires the phase to be constant during the acquisition of the phase-shifted interferograms.

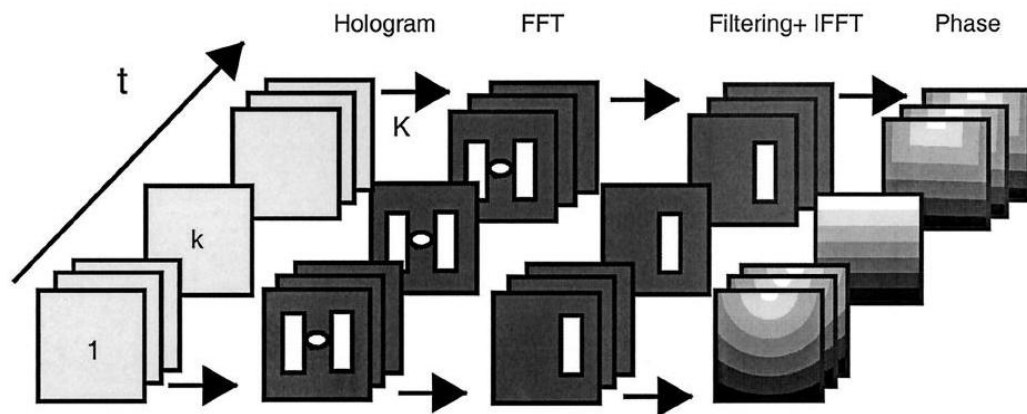


Figure 2.8 Procedure for temporal phase unwrapping of digital holograms (Pedrini et al., 2003)

A sequence of digital holograms of an object subjected to continuous deformation is recorded. Each hologram is then reconstructed and the phase distribution is calculated. As we know, the calculated phase distribution are all wrapped into $-\pi$ to π , therefore, a temporal phase unwrapping (Huntley and Saldner, 1993) is needed to carry out pixel by pixel. The 2D evolution of phase as function of time can be obtained. It is noticed that before the unwrapping process pixels having low intensity modulation are removed.

2.7 Short time Fourier transform (STFT)

2.7.1 An introduction to STFT

The Fourier transform has been the standard tool for signal processing in the spectral domain for many years. Although not accepted at the first time it is introduced, Fourier transform later became the cornerstones of contemporary mathematics and engineering.

The definition of Fourier transform is given as:

$$\hat{f}(w) = \int_{-\infty}^{+\infty} f(t) e^{-iwt} dt \quad (2.28)$$

However, such a tool appears clumsy when the signal is nonstationary. Since many signals in practice have spectra which vary with time. Due to the nature of classic Fourier transform, only the overall frequency is revealed. Therefore the information at which a frequency occurs at a certain time is lost. One solution of this problem is to introduce time dependency and at the same time preserve the linearity. The short time Fourier transform looks at the signal through a window over which the signal is approximately stationary (Goudemand, 2006).

The STFT splits the signal into many segments, which are then Fourier transformed. A window function $g(t-u)$ located at instant u isolates a small portion of the signal. The resulting STFT is (Mallat, 1999):

$$Sf(u, \xi) = \int_{-\infty}^{+\infty} f(t) g(t-u) e^{-i\xi t} dt \quad (2.29)$$

The only difference between Eq. (2.37) and standard Fourier transform is the presence of a window function $g(t)$. As the name implies, small durations of the signal are Fourier transformed. Alternatively, the STFT can also be interpreted as the

projection of the signal onto a set of bases $g^*(t-u)e^{-i\xi t}$ with the parameters t and w . Those bases don't have infinite extent in time any more (Chen and Ling, 2002). Hence it is possible to observe how the signal frequency changes with time. This is accomplished by translating the window with time. A 2D joint time-frequency representation can thus be resulted.

An energy density called spectrogram is then defined (Mallat, 1999):

$$P_s f(u, \xi) = |Sf(u, \xi)|^2 \quad (2.30)$$

It measures the energy of the signal in the time-frequency neighborhood of (u, ξ) specified by the Heisenberg box of $g_{u, \xi}$.

In STFT, the time-frequency uncertainty principle states that the product of the temporal duration Δt and frequency bandwidth $\Delta \omega$ is necessarily larger than a constant factor: $\Delta t \Delta \omega \geq 1/2$. Equality holds if and only if the window function w is Gaussian.

2.7.2 STFT in optical metrology

Two advantages of STFT make it a powerful tool when applied to optical metrology: (1) STFT is performed locally contrast to the global operation of Fourier transform. Hence a signal in one position will not affect the signal of another place, if the distance between them is larger than the effective radius of the window; (2) the spectrum of a local signal tends to be simpler than the spectrum of the whole signal. Thus more effective operation is possible (Qian, 2004). Compared with most commonly used Fourier transform, STFT is able to reduce the noise more effectively and prevent the propagation of bad pixels. Furthermore, it is more adaptive to exponential field and

more robust to noise due to its redundancy compared with discrete orthogonal wavelet transform (Qian et al., 2005). Two spatial methods were proposed by Qian (2004). One is to filter the phase field by STFT and the other is to extract phase derivation by ridge algorithm of STFT. The main application of STFT includes phase and frequency retrieval, strain estimation in moiré interferometry, fault detection, edge detection and fringe segmentation.

2.7.2.1 Filtering by STFT

A fringe is first transformed into its spectrum. The noise distributes all over the spectrum due to the randomness and incoherence with the STFT basis. It can be suppressed by discarding the coefficients if their values are smaller than the preset threshold. A smooth image will be obtained after the inverse STFT. The scheme is described as:

$$\bar{f}(x, y) = \frac{1}{4\pi^2} \int_{-\infty}^{+\infty} \int_{-\infty}^{+\infty} \int_{\eta_l}^{\eta_h} \int_{\xi_l}^{\xi_h} \overline{Sf}(u, v, \xi, \eta) \times g_{u,v,\xi,\eta}(x, y) d\xi d\eta dudv \quad (2.31)$$

with

$$\overline{Sf}(u, v, \xi, \eta) = \begin{cases} Sf(u, v, \xi, \eta) & \text{if } |Sf(u, v, \xi, \eta)| \geq thr \\ 0 & \text{if } |Sf(u, v, \xi, \eta)| \leq thr \end{cases} \quad (2.32)$$

Figure 2.9 shows an example from Qian (2007). It can be seen that a much better result is obtained by STFT.

2.7.2.2 Ridges by STFT

Consider a small block of a fringe pattern. A windowed element $g_{u,v,\xi,\eta}(x, y)$ is used to compare with it. The element that gives the highest similarity is called ridge. The

values of ξ and η that maximize the similarity are taken as the local frequency of pixel (ξ, η) . Local frequencies are expressed as:

$$\left[w_x(u, v), w_y(u, v) \right] = \arg \max |Sf(u, v, \xi, \eta)| \quad (2.33)$$

Figure 2.10 shows an example of strain exaction from moiré interferograms by WFR.

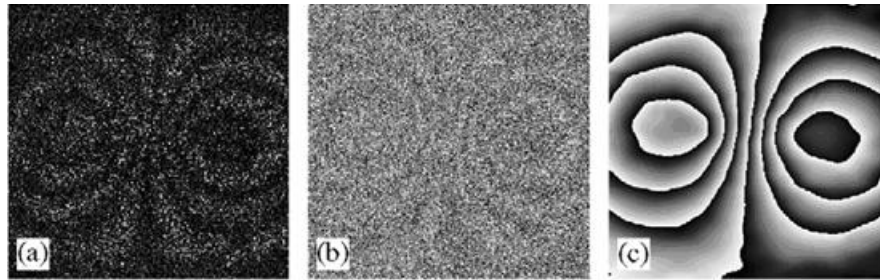


Figure 2.9 Phase retrieval from phase-shifted fringes: (a) one of four phase-shifted fringe patterns; (b) phase by phase-shifting technique and (c) phase by WFR. (Qian, 2007)

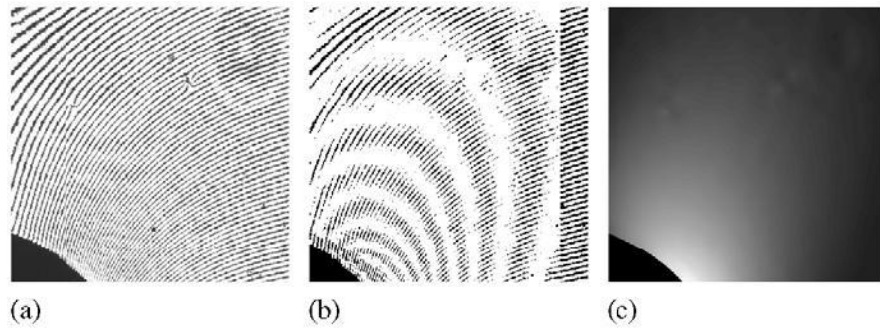


Figure 2.10 WFR for strain extraction: (a) Original moiré fringe pattern; (b) strain contour in x direction using moiré of moiré technique and (c) strain field by WFR (Qian, 2007)

CHAPTER THREE

THEORY DEVELOPMENT

3.1 D.C.-term of the Fresnel transform

As shown in the intensity display of a holographic reconstruction in Figure 3.1, a bright center square is recognized, which is much brighter than the reconstructed image. Nothing is done to enhance the eligibility of the overall pattern. Therefore no images will be observed. The bright center can be explained as the undiffracted part of the reconstructing reference wave from the optical point of view; it is D.C.-term of the Fresnel transform from the computational point view.

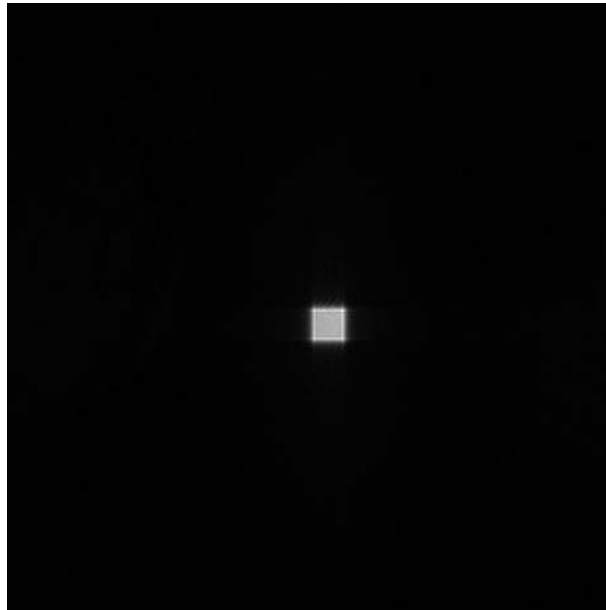


Figure 3.1 A reconstructed intensity distribution by Fresnel transform without clipping

If the factors affecting the phase in a way independent of the specific hologram before the integrals of Eq. (2.14) or Eq. (2.17) are neglected, the Fresnel transform is

nothing but a Fourier transform of a product. The product is the result of hologram timing the reference wave and a chirp function. According to the convolution theorem, a same result will be obtained as the convolution of the Fourier transforms of individual factors. The Fourier transform of the hologram multiplied with reference wave $E_R(k,l)h(k,l)$ generally is a trimodal with a high-amplitude peak at the spatial frequency $(0,0)$. The D.C. - term whose value is calculated by

$$H(0,0) = \sum_{k=0}^{M-1} \sum_{l=0}^{N-1} E_R(k,l)h(k,l) \quad (3.1)$$

can be modeled by a Dirac delta function. The D.C.-term of the Fresnel transform now becomes the D.C.-term of the Fourier transform of the digital hologram multiplied by the reference wave convolved with the Fourier transform of the two-dimensional chirp function. Since a Dirac delta function is assumed for Eq. (3.1), D.C.-term for the Fresnel transform is the Fourier transform of the finite chirp function

$$\exp\left[i \frac{\pi}{\lambda d} (k^2 \Delta \xi^2 + l^2 \Delta \eta^2)\right] \quad (3.2)$$

In two dimensions, the area of D.C.-term is given as

$$\frac{M^2 \Delta \xi^2}{d \lambda} \times \frac{N^2 \Delta \eta^2}{d \lambda} \quad (3.3)$$

where $M^2 \Delta \xi^2 / d \lambda$ is along x direction and $N^2 \Delta \eta^2 / d \lambda$ along y direction. It is observed that the width of D.C.-term increases with increasing pixel dimensions and pixel number of the CCD sensor while decreases with increasing distance d .

As shown above, D.C.-term is of no practical use at all, however, due to its high intensity, it disturbs the dynamic range of the display seriously. Nothing can be done to

the D.C.-term in optical holography, however, there indeed exists some effective numerical methods to eliminate D.C.-term.

Takaki et al. (1999) described a separate recording method, in which the object wave intensity and the reference wave intensity are recorded separately besides recording the hologram. The object wave intensity and the reference wave intensity are then subtracted from the hologram before reconstruction. A stochastic phase (Demoli et al., 2003) is introduced during the recording. The digital hologram is then subtracted from the one without this phase, which can also result in a suppression of the unwanted terms. These hybrid methods require extra experimental efforts such as shutter, phase modulator as well as the multi-recording of digital hologram of the same scene. Thus they are not suitable for holographic interferometric applications, especially dynamic measurement.

A combination of purely numerical methods only using a single digital hologram is mainly used in this study. A mean value subtraction method is introduced by Kreis and Jüptner (1997). Rewrite Eq. (2.3) as follows:

$$\begin{aligned} I(x, y) &= |E_O(x, y) + E_R(x, y)|^2 \\ &= a_O^2(x, y) + a_R^2(x, y) + 2a_O a_R \cos(\varphi_O - \varphi_R) \end{aligned} \quad (3.4)$$

We can see that the first two terms lead to D.C.-term in the reconstruction process. The third term is statically varying between $\pm 2a_O a_R$ from pixel to pixel at the CCD sensor surface. The average intensity of the digital hologram is

$$I_{av} = \frac{1}{MN} \sum_{k=0}^{M-1} \sum_{l=0}^{N-1} I(k, l) \quad (3.5)$$

The first two items now can be suppressed by subtracting this average intensity I_{av} from the original digital hologram.

$$I'(k, l) = I(k, l) - I_{av}(k, l) \quad (3.6)$$

As a consequence, D.C.-term in the Fourier spectrum of $I'(k, l)$ by Eq. (3.1) is zero. The convolution of a zero with the transform of the chirp function is zero. It is noteworthy that $I'(k, l)$ will exhibit negative values, which are impossible in optical holography. This concept, however, is possible in digital holography. Since the relationship between each pixel is the same, with the only difference that the digital hologram is downshifted.

The above method can be interpreted as the application of a high-pass filter with a cut off frequency just equal to the smallest nonzero frequency. Therefore other high-pass filters can also be employed. In this way, good results have been realized by the high pass filter subtracting the averages over 3×3 pixel neighborhood from the origin digital hologram:

$$I'(k, l) = I(k, l) - \frac{1}{9} \left[I(k-1, l-1) + I(k-1, l) + I(k-1, l+1) \right. \\ \left. + I(k, l-1) + I(k, l) + I(k, l+1) \right. \\ \left. + I(k+1, l-1) + I(k+1, l) + I(k+1, l+1) \right] \quad (3.7)$$

where $k = 2, \dots, M-1$ and $l = 2, \dots, N-1$.

As mentioned in previous chapter, digital lensless Fourier holography is just a simple 2D Fourier transform of the recorded digital hologram. Figure 3.2 illustrates the intensity display of a reconstructed image. The recorded object is a die. D.C.-term for this special setup restricts only to a pixel lying at the spatial frequency $(0,0)$.

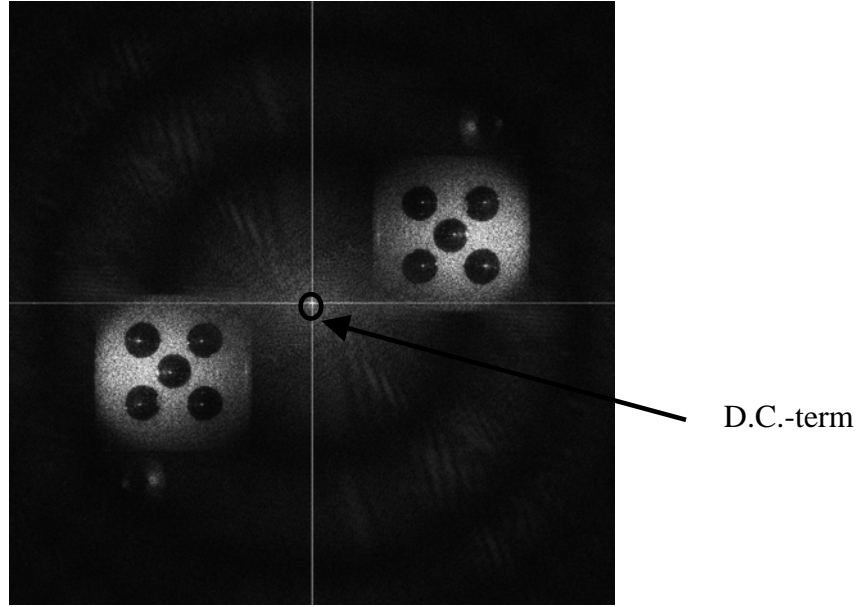


Figure 3.2 Digital lensless Fourier holography

3.2 Spatial frequency requirements

The biggest difference of digital holography from optical holography is the employment of CCD to record holograms which are then stored and reconstructed in a computer. The angle α between the object and reference wave determines the spatial frequency of this interference pattern. The maximum spatial frequency to be resolved is therefore:

$$f_{\max} = \frac{2}{\lambda} \sin \frac{\alpha_{\max}}{2} \quad (3.8)$$

A sampling of the intensity distribution of the hologram is meaningful only if the sampling theorem is satisfied. The sampling theorem requires that the sampling rate must be at least two times larger than the maximum frequency:

$$\frac{1}{\Delta \xi} > 2f_{\max} \quad (3.9)$$

Because α in all practical cases remain small, an approximation $\sin \alpha/2 = \alpha/2$ in the calculations can be adopted. From Eq. (3.8) and (3.9), an upper limit to the angle is set:

$$\alpha_{\max} = \frac{\lambda}{2\Delta\xi} \quad (3.10)$$

In holography, no matter optical or digital, the configurations of the recording system can be categorized into two kinds: in-line and off-axis. Applications of in-line system are generally limited due to its interactive influence of coaxial diffraction wave components, while it is off-axis setups that have been always active. **Therefore, in this study, we restrict ourselves to the discussion of off-axis systems.** In the off-axis setup, an offset angle θ is generally introduced to separate the various diffraction wave components in space. In digital Fresnel holography, such an angle is made by placing the object a distance b_{off} away from the optical axis of the system, while the collimated reference wave incidents normally onto the CCD sensor surface.

To separate the twin images from each other and from D.C.-term, the offset angle θ between the object wave and the reference wave must be greater than a minimum value θ_{\min} .

Suppose that the spatial frequency bandwidth of the object is W_o . The spectrum of the diffraction terms of an off-axis system is shown in Figure 3.3. $|G_1|$ term lying at the origin of the frequency plane is just the spectrum of direct transmitting reference wave, while the term $|G_2|$ is the halo wave component. It is the autocorrelation of the object spectrum in the spatial frequency domain and has a bandwidth of $2W_o$. $|G_3|$

term whose center is located at position $(\sin \theta / \lambda, 0)$ is proportional to the object spectrum. It is actually the real image wavefield in the spatial domain, while $|G_4|$ is the spectrum of the virtual image. In order to separate $|G_3|$ or $|G_4|$ term from $|G_2|$ term, the condition of $\sin \theta / \lambda > 3W_o/2$, the minimum allowable offset angel θ_{\min} is therefore:

$$\theta_{\min} = \sin^{-1}(3W_o\lambda/2) \quad (3.11)$$

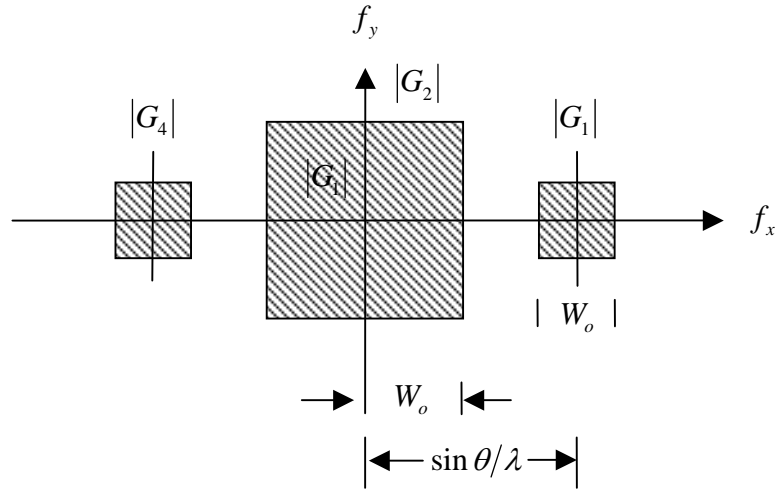


Figure 3.3 Spatial frequency spectra of an off-axis holography

Suppose that the object has the lateral extensions of $L_x \times L_y$. Figure 3.4 illustrates the geometry of off-axis Fresnel digital holography. Consider the case that the object is placed offset along the X-axis.

The bandwidth of the object along the X-axis in frequency domain is $L_x/\lambda D$. Compared with the distance between object and CCD sensor, the size of the CCD sensor is quite small. Therefore, an approximation is adopted:

$$\theta_{\min} = \frac{3L_x}{2D} \quad (3.12)$$

The maximum interference angle α_{\max} and the minimum offset angle θ_{\min} determine the digital recording geometry interactively (Xu et al., 1999):

$$D_{\min} = \frac{\Delta\xi}{\lambda} (M\Delta\xi + 4L_x) \quad (3.13)$$

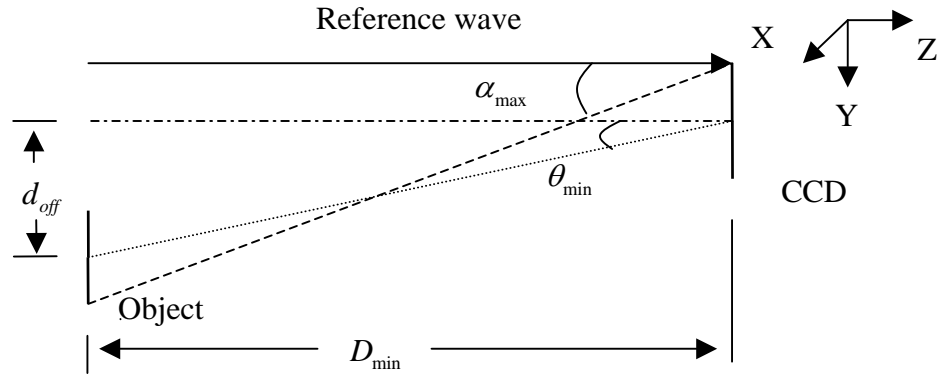


Figure 3.4 Geometry for recording an off-axis digital Fresnel hologram

Figure 3.5 is the geometry of off-axis lensless Fourier holography. Similarly, two interactive factors determine the minimum recording distance as (Xu, 1999):

$$D_{\min} = \frac{4\Delta\xi \cdot L_x}{\lambda} \quad (3.14)$$

It can be observed from the above equation that digital lensless Fourier holography has the favorable feature of smaller recording distance compared with Fresnel holography. Due to limited spatial resolution of modern digital recording device, it is important to fully use the bandwidth of the CCD sensor. In digital lensless Fourier holography, the spherical reference wave is employed. Therefore, the angle between the object wave and the reference wave is nearly constant all over the sensor surface, as illustrated in Figure 3.6(Wagner et al., 1999).

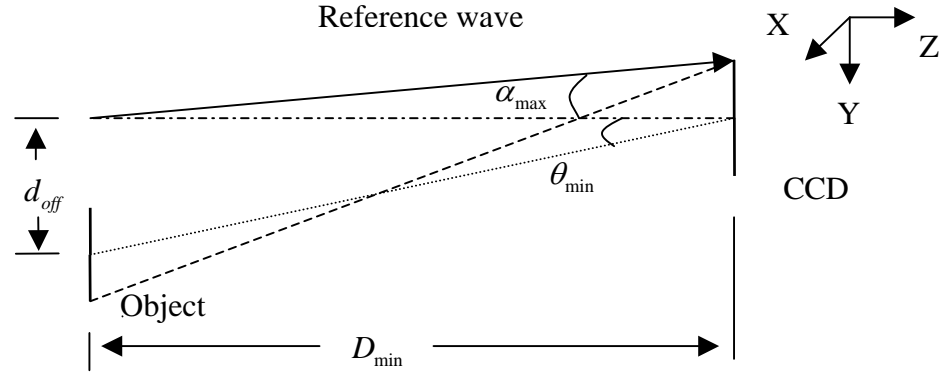


Figure 3.5 Geometry for recording an off-axis digital lensless Fourier hologram

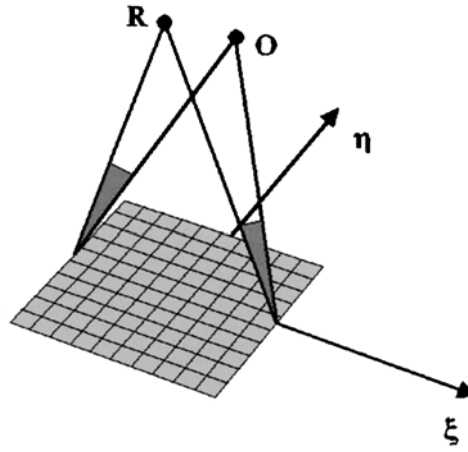


Figure 3.6 Schematic illustration of the angle between the object wave and reference wave in digital lensless Fourier holography setup (Wagner et al., 1999)

The sampling theorem is obeyed over the whole area. In addition, this kind of setup makes full use of the spatial-frequency spectrum of the CCD sensor at any point. The micro interference pattern by this setup is a sinusoid fringe with a unique vector spatial frequency of that object point. For a plane reference wave, however, the angle varies over the sensor surface. The bandwidth in some places of the sensor is therefore not fully used, taking into consideration of the sampling theorem. Each object point is encoded into an elementary sinusoidal zone plate consisted of an entire range of spatial frequency components.

3.3 Deformation measurement by HI

In the holographic interferometric measurement of deformation, the displacement of each surface point P results in an optical path difference $\delta(P)$. The interference phase $\Delta\phi(P)$ relates to this path difference (Kreis, 2005) by:

$$\Delta\phi(P) = \frac{2\pi}{\lambda} \delta(P) \quad (3.15)$$

The geometric quantities are explained in Figure 3.7. The displacement vector \vec{d} describes the shift of surface point P from its original position P_1 to its new position P_2 . The optical path difference $\delta(P)$ is then given by:

$$\begin{aligned} \delta(P) &= \overline{SP_1} + \overline{P_1B} - (\overline{SP_2} + \overline{P_2B}) \\ &= \vec{s}_1 \cdot \overline{SP_1} + \vec{b}_1 \cdot \overline{P_1B} - \vec{s}_2 \cdot \overline{SP_2} - \vec{b}_2 \cdot \overline{P_2B} \end{aligned} \quad (3.16)$$

where \vec{s}_1 and \vec{s}_2 are unit vectors along the illumination direction, \vec{b}_1 and \vec{b}_2 are unit vectors in the observation direction, and $\overline{SP_i}$ and $\overline{P_iB}$ are the vectors from S to P or P to B , which are usually in the range of meter. And the \vec{d} is in the range of several micrometers. The vectors \vec{s}_1 and \vec{s}_2 can therefore be replaced by a unit vector \vec{s} pointing into the bisector of angle between them.

$$\vec{s}_1 = \vec{s}_2 = \vec{s} \quad (3.17)$$

Similarly for the vectors \vec{b}_1 and \vec{b}_2

$$\vec{b}_1 = \vec{b}_2 = \vec{b} \quad (3.18)$$

By definition of the displacement vector \vec{d} , we have

$$\vec{d} = \vec{P_1B} - \vec{P_2B} \quad (3.19)$$

$$\vec{d} = \vec{SP_2} - \vec{SP_1} \quad (3.20)$$

Inserting Eq. (3.17) to (3.20) into (3.16) gives:

$$\delta = (\vec{b} - \vec{s}) \vec{d} \quad (3.21)$$

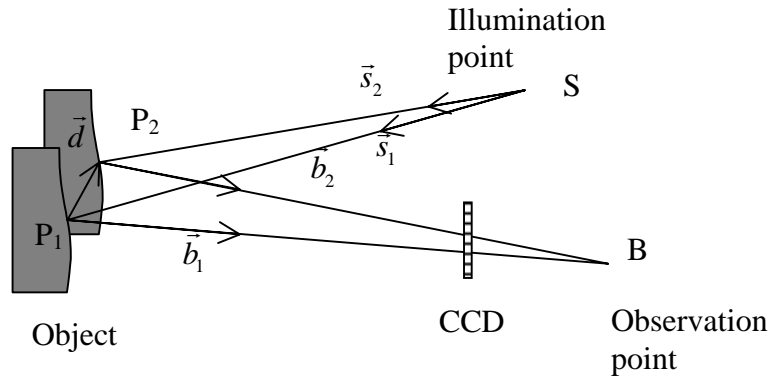


Figure 3.7 Sensitivity vector for digital holographic interferometric measurement of displacement

Therefore we have the expression for the interference phase (Schnars and Jüptner, 2005):

$$\Delta\varphi(P) = \frac{2\pi}{\lambda} \vec{d}(P) (\vec{b} - \vec{s}) = \vec{d}(P) \vec{S} \quad (3.22)$$

The vector \vec{S} is called sensitivity vector, which is determined by the geometry of the holographic arrangement. It gives the direction along which the setup has the maximum sensitivity. It is the projection of the displacement vector onto the sensitivity

vector. Eq. (3.22) constitutes the basis of all quantitative measurements of the deformation of opaque bodies by holographic interferometry.

3.4 Shape measurement by HI

In two-illumination-method, the illumination point S is shifted to S' between the two recording of digital holograms, as shown in Figure 3.8. The resulting optical path length difference δ is:

$$\begin{aligned}\delta &= \overline{SP} + \overline{PB} - (\overline{S'P} + \overline{PB}) = \overline{SP} - \overline{S'P} \\ &= \vec{s}_1 \overline{SP} - \vec{s}_2 \overline{S'P}\end{aligned}\quad (3.23)$$

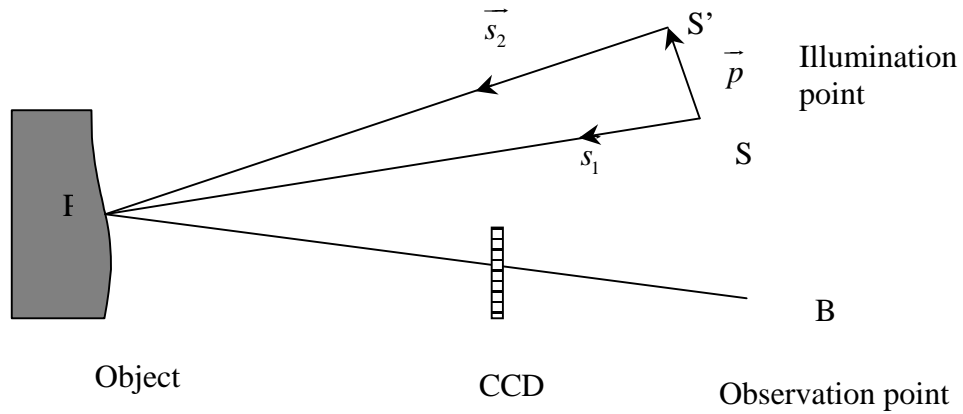


Figure 3.8 Two-illumination point contouring

The unit vectors have the same definition as the ones in deformation derivation.

And the same approximation is used here:

$$\vec{s}_1 = \vec{s}_2 = \vec{s} \quad (3.24)$$

The optical path length difference is then given as:

$$\delta = \vec{s} (\overline{SP} - \overline{S'P}) = \vec{s} \overline{p} \quad (3.25)$$

The corresponding interference phase is:

$$\Delta\varphi = \frac{2\pi}{\lambda} \vec{p} \cdot \vec{s} \quad (3.26)$$

3.5 Temporal phase unwrapping algorithm

Spatial smoothing is always necessary when analyzing data from speckle interferometers. It is usually best to carry out the smoothing before unwrapping rather than after (Huntley, 2002). Therefore, another algorithm was proposed by Huntley et al. (1999) to overcome the previous problems. The number of 2π phase jumps between two successive wrapped interference phases is then determined by:

$$d(t) = \text{NINT} \left\{ \left[\Delta\varphi_w(t, 0) - \Delta\varphi_w(t-1, 0) \right] / 2\pi \right\} \quad (3.27)$$

The total number of phase jumps $v(t)$, is calculated by:

$$v(t) = \sum_{t'=2}^t d(t') \quad t = 2, 3, \dots, N-1 \quad (3.28)$$

$$v(1) = 0 \quad (3.29)$$

and the unwrapped interference phase is obtained as:

$$\Delta\varphi_u(t, 0) = \Delta\varphi(t, 0)_w - 2\pi v(t) \quad t = 1, 2, \dots, N-1 \quad (3.30)$$

3.6 Complex field analysis

One of the most attractive features of DH is that it allows the intensity and the phase the electromagnetical wave fields to be measured, stored, transmitted, applied to

simulations and manipulated in the computer. In reality, there is always certain amount of noise in experimental data, especially in speckle interferometry (e.g. digital holography). In the unwrapping process, the most critical step is to prevent the propagation of erroneous phase values. Therefore, it is necessary to obtain correct phase values before phase unwrapping. In previous works of digital holography, phase values calculated from a reconstructed complex field are processed and manipulated directly, without taking into consideration any intensity information. The intensity information of a reconstructed wave field is a good measure of the phase values (Yamaguchi et al., 2001), (Pedrini et al., 2003). In this study, a complex phasor method (CP) is proposed, in which both the amplitude and the phase information are considered.

Using this method, the interference phase is calculated by another way. The coordinate system adopted here is the same as shown in Figure 2.5. Digital holograms at different states are recorded on the hologram plane (ξ, η) and the reconstructed complex wave field on an object plane (x, y) is given by:

$$\Gamma(x, y, n) = a(x, y, n) \exp[i\varphi(x, y, n)] \quad (3.31)$$

where $a(x, y, n)$ is the real amplitude and $\varphi(x, y, n)$ is the phase of the object wave. Subsequently, two reconstructed complex wave fields of different states can be brought to interfere with each other by conjugate multiplication, and the resulting complex phasor distribution is to be processed. For simplicity, only one pixel is considered:

$$A(n) = \Gamma(n) \Gamma^*(0) = a(n)a(0) \exp\{i[\varphi(n) - \varphi(0)]\} = |A(n)| \exp[i\Delta\varphi(n, 0)] \quad (3.32)$$

where $n = 1, 2, \dots, N - 1$

The interference phase is given as:

$$\Delta\phi_w(n, 0) = \arctan \frac{\text{Im}[A(n)]}{\text{Re}[A(n)]} \quad (3.33)$$

where subscript w denotes a wrapped phase value. Each pixel of an interference phase map no longer presents a real-value phase but a complex-value phasor. Processing CP instead of phase offers the following advantages: (1) There is no need to discriminate the cases as in Eq. (2.27); (2) Processing a CP not only preserves the advantage of Eq. (2.27) it also provides more accurate results; (3) The real and imaginary parts of a CP are weighted implicitly by the square of the intensity modulation, which is a new filtering approach.

3.7 Temporal phase retrieval from complex field

Similar to temporal phase unwrapping, our proposed temporal phase retrieval methods analyze the fringe patterns pixel by pixel in which the complex phasor at each pixel is measured and analyzed as a function of time. Each pixel of the sensor acts as an independent sensor, the signal is processed temporally instead of spatially.

3.7.1 Temporal Fourier transform

Consider now a special case in which the interference phase is linearly dependent on time, as shown in Figure 3.9. The complex phasor will then be in the form of $|A(n)|\exp(i\omega t)$. After the complex phasor is transformed, a high amplitude peak whose position is determined by the phase changing rate ω appears in the spectrum as shown in Figure 3.10.

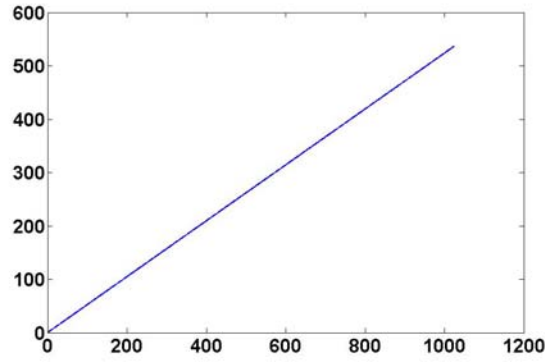


Figure 3.9 A linearly changing phase

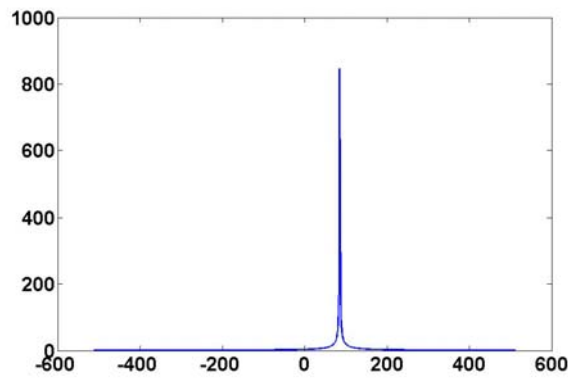


Figure 3.10 The spectrum of a complex phasor with linearly changing phase

Fourier transform is calculated most efficiently with FFT algorithm, however, the resulting frequency k are limited to integers. This is not sufficient just to calculate w and an algorithm for evaluating k which is not constrained to integer values is proposed. The main principle is based on Huntley's (1997) method for temporal unwrapping of a sequence of interference phase maps. An initial value of k_e is used to obtain the exact value k_p . This is carried out by getting the position of the peak from the resulting spectrum. The Search for the exact value k_p is carried out as follows:

- (1) $A(n)$ is expressed as $a_n + ib_n$ and the Fourier transform of $A(n)$ is given by:

$$\begin{aligned}
\mathfrak{I}(k) &= \sum_{n=1}^N (a_n + ib_n) \{ \cos[-2\pi k(n-1)/N] + i \sin[-2\pi k(n-1)/N] \} \\
&= \sum_{n=1}^N (a_n \cos \alpha_{n-1} + b_n \sin \alpha_{n-1}) + i \sum_{n=1}^N (b_n \cos \alpha_{n-1} - a_n \sin \alpha_{n-1}) \\
&= \text{Re}[\mathfrak{I}(k)] + i \text{Im}[\mathfrak{I}(k)]
\end{aligned} \tag{3.34}$$

where $\alpha_{n-1} = 2\pi k(n-1)/N$, the real and imaginary parts of $\mathfrak{I}(k)$ are denoted by $\text{Re}[\mathfrak{I}(k)]$ and $\text{Im}[\mathfrak{I}(k)]$ respectively.

(2) The intensity of the transform can be calculated from the real and imaginary part of the resulting complex phasor:

$$|\mathfrak{I}(k)|^2 = \text{Re}^2[\mathfrak{I}(k)] + \text{Im}^2[\mathfrak{I}(k)] \tag{3.35}$$

and its first derivative

$$\frac{\partial}{\partial k} |\mathfrak{I}(k)|^2 = 2 \{ \text{Re}[\mathfrak{I}(k)] d \text{Re}[\mathfrak{I}(k)] + \text{Im}[\mathfrak{I}(k)] d \text{Im}[\mathfrak{I}(k)] \} \tag{3.36}$$

where $d \text{Re}[\mathfrak{I}(k)]$ and $d \text{Im}[\mathfrak{I}(k)]$ are the first derivatives of the real and imaginary parts, respectively.

(3) An iterative algorithm (Press et al., 2002) is then employed to determine k_p . Compared with the bounded Newton-Raphson algorithm (Huntley, 1986), the proposed algorithm offers less programming code and lighter calculation burden. The rate of phase change is given by:

$$w = 2\pi k_p / N \tag{3.37}$$

3.7.2 Temporal STFT analysis

Fourier transform utilizes the global information of a signal and shows the overall frequency. Therefore, a signal in one position will definitely affect one signal in another place. As discussed in the previous chapter, the window function employed by STFT is to avoid such a problem. Furthermore, it can locate when or where a certain frequency occurs. This offers an alternative for interpretation of phase values.

3.7.2.1 Temporal filtering by STFT

Similar to Qian's spatial filtering approach, the proposed temporal filtering method is as follows: Provide a threshold value for the spectrum and set spectral components with low amplitude to zero. It is assumed that noise is widely distributed with low coefficients in the spectrum. After eliminating the noise, a high-quality signal can be reconstructed from the filtered spectrum.

A complex phasor denoted by $f(t)$ varies with time t and its STFT is:

$$Sf(u, v) = \int_{-\infty}^{+\infty} f(t)g(t-u)\exp(-ivt)dt \quad (3.38)$$

where $g(t)$ is a window function. Generally, it is a Gaussian function that gives the smallest Heisenberg box. As it is assumed that white noise is distributed over the whole frequency domain, however, the STFT of the input signal usually has a smaller band of distribution. Therefore, the signal and white noise in the frequency domain are well separated. As for the overlapped part, the coefficient is taken as white noise if its amplitude is smaller than a preset threshold. Thus, the noise can be removed more effectively. This procedure is somewhat similar to filtering by wavelet transform. The

filtered sequence of complex phasors can be obtained by an inverse STFT of the filtered coefficients:

$$f(t) = \frac{1}{2\pi} \int_{-\infty}^{+\infty} \int_L^U S f(u, v) g(t-u) \exp(i v t) dv du \quad (3.39)$$

where U and L are the upper and lower integration limits of v . The integration limits can be estimated by the following procedure: Firstly, 1D Fourier transform the sequence of complex phasors into Frequency domain. Secondly, manually set the bandwidth. Thirdly, pick up the peak. The upper limit and lower limit can then be decided by adding and subtracting half the bandwidth from the peak. The wrapped phases can be calculated by Eq. (3.33) and the temporal phase unwrapping is carried out.

3.7.2.2 Temporal phase extraction from a ridge

Often, it is more important to know when or where those frequency components happen and how they change with time. The concept of instantaneous frequency (IF) has been created in response to such kind of problem. The IF is defined:

$$f_i(t) = \frac{1}{2\pi} \cdot \frac{\partial}{\partial t} \varphi(t) \quad (3.40)$$

where the signal is in the form of $A(t) \cdot \exp[i\varphi(t)]$.

If the instantaneous frequencies of the phases are known, more useful information can be obtained, for example velocity measurement is possible in deformation measurement. There are currently two methods for instantaneous frequency estimation: either filter-based or time-frequency-representation (TFR)-based. Most existing approaches can be categorized into these two methods. However, the

filter-based methods are often difficult to converge and appear clumsy when tracking rapidly varying instantaneous frequency. In TFR, time and frequency information of a signal is jointly displayed on a 2D plane. STFT and Winger distribution (WD) are two popular choices among existing TFRs. However, large cross terms of WD are major handicap. Thus, STFT technique which is free of cross terms is a good choice over WD.

The STFT of complex phasor variation can also be expressed as the following (Mallat, 1999):

$$SA(u, \xi) = \frac{\sqrt{s}}{2} |A(u)| \exp \{i[\Delta\varphi(u) - \xi u]\} \left\{ \hat{g}(s[\xi - \Delta\varphi'(u)]) + \varepsilon(u, \xi) \right\} \quad (3.41)$$

where ε is a corrective term. It can be neglected if both $A(u)$ and $\Delta\varphi'(t)$ have small relative variations over the support of window g_s (Mallat, 1999). The term “small relative variations” is not precisely defined, therefore, in our experiment “small relative” is determined through experience. In this study, scale s is actually not used and assigned to 1. It is verified that the value of the term $A'(u)/A(u)$ in the range of window g_s is around 0.1, hence $A(u)$ is considered to have a relatively small variation in our study and linear assumption of Eq. (3.41) is satisfied. A similar result is shown by Delprat et al. (1992) using a stationary phase approximation when $g(t)$ is Gaussian. It can be seen that $\Delta\varphi'(t)$ is possible to be calculated by neglecting the corrective term from Eq. (3.11). In Eq. (3.11), the term $|\hat{g}(w)|$ reaches its maximum at $w = 0$, therefore for each u the spectrogram $|SA(u, \xi)|^2$ is maximum at $\xi(u) = \Delta\varphi'(u)$. The corresponding time-frequency points $[u, \xi(u)]$ are known as ridges (Mallat, 1999).

At each instant, a frequency with the highest energy density is regarded as the most probable instantaneous frequency. The most popular approach introduced by Delprat to calculate instantaneous frequencies is to pick the peak from a locally transformed signal $|SA(u, \xi)|^2$. Mathematically, $\Delta\phi'(u)$ is expressed as

$$\Delta\phi'(u) = \arg \max_{\xi} |SA(u, \xi)| \quad (3.42)$$

The discrete version of STFT is given as

$$SA(m, l) = \sum_{n=0}^{N-1} A(n) g_s(n-m) \exp\left(\frac{-i2\pi ln}{N}\right) \quad (3.43)$$

where $n = t - 1$ and N is the total number of sampled points. Due to digitalization of time and frequency in the implementation, the output changes from continuous to discrete values which are generally integers.

$$\Delta\phi'(u) = 2\pi \frac{l}{N} \quad (3.44)$$

In order to find the exact position of l_e which usually lies between frequency plots within a certain tolerance, the analysis is carried out as follows:

- (1) For a given time instant m , Eq. (3.43) is first calculated by FFT algorithm. The value of l that maximizes $|SA(m, l)|^2$ is then used as an initial estimate.
- (2) Express a windowed signal $A(n)g_s(n-m)$ as $a_w(n) + ib_w(n)$, therefore the $SA(m, l)$ is calculated as follows:

$$\begin{aligned}
SA(m, l) &= \sum_{n=0}^{N-1} [a_w(n) + ib_w(n)] [\cos(-2\pi ln / N) + i \sin(-2\pi ln / N)] \\
&= \sum_{n=0}^{N-1} [a_w(n) \cos \alpha_n + b_w(n) \sin \alpha_n] + i \sum_{n=0}^{N-1} [b_w(n) \cos \alpha_n - a_w(n) \sin \alpha_n] \\
&= \text{Re}[SA(m, l)] + i \text{Im}[SA(m, l)]
\end{aligned} \tag{3.45}$$

where $\alpha_n = 2\pi ln / N$, $\text{Re}[SA(m, l)]$ and $\text{Im}[SA(m, l)]$ are the real and imaginary parts of $SA(m, l)$.

(3) The intensity of the transform is then given by

$$|SA(m, l)|^2 = \text{Re}^2[SA(m, l)] + \text{Im}^2[SA(m, l)] \tag{3.46}$$

and its first derivative is

$$\begin{aligned}
\frac{\partial}{\partial l} |SA(m, l)|^2 &= 2 \text{Re}[SA(m, l)] \frac{\partial}{\partial l} \text{Re}[SA(m, l)] \\
&\quad + 2 \text{Im}[SA(m, l)] \frac{\partial}{\partial l} \text{Im}[SA(m, l)]
\end{aligned} \tag{3.47}$$

(4) A modified Brent algorithm using first derivatives is employed to determine the exact value of l_e within the given tolerance.

Phase unwrapping process can be avoided by integration of the instantaneous frequency instead of temporal phase unwrapping.

3.7.2.3 Window Selection

It is well known that an uncertainty relationship between time and frequency resolution exists in STFT. A shorter window provides poorer frequency resolution but is able to show rapidly changing signal and vice versa. A schematic demonstration is shown in

Figure 3.11. Hence, a tradeoff between time and frequency resolution has to be made when choosing an appropriate window. Choosing an optimal window for each sequence is the most critical part of the whole processing.

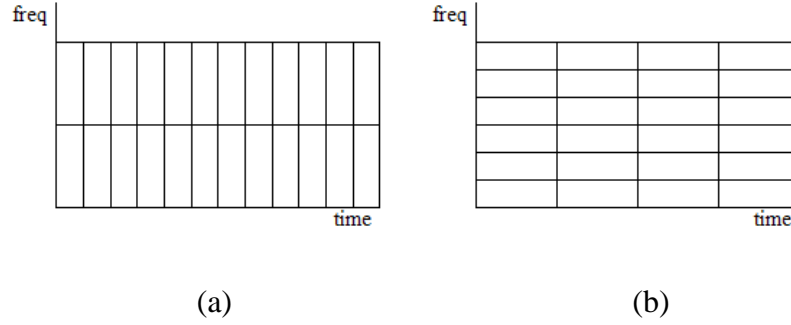


Figure 3.11 Comparison of STFT resolution: (a) a better time solution; (b) a better frequency solution

Consider a sample signal composed of a set of frequencies in a sequence. The definition of the signal is:

$$S(t) = \begin{cases} \exp(i10\pi t) & 0 \leq t < 0.1s \\ \exp(i25\pi t) & 0.1 \leq t < 0.2s \\ \exp(i50\pi t) & 0.2 \leq t < 0.3s \\ \exp(i100\pi t) & 0.3 \leq t < 0.4s \end{cases} \quad (3.48)$$

Following spectrograms in Figure 3.12 are obtained with different window length.

It is observed that the shortest window provides the most precise time at which the signals change while the frequencies are hard to identify. The longest window allows a precise observation of the frequency content. However, the time information is blurred.

The ability of STFT to preserve the time-frequency domain support of signals (Durak and Arikan, 2003) is an important criterion to measure the success of STFT representations. The time-frequency domain support of a signal $x(t)$ is commonly

measured by its time-width T_x and its frequency domain bandwidth B_x , which are defined as

$$T_x = \frac{\left[\int (t - \eta_t)^2 |x(t)|^2 dt \right]^{1/2}}{\|x\|} \quad (3.49)$$

$$B_x = \frac{\left[\int (f - \eta_f)^2 |X(f)|^2 df \right]^{1/2}}{\|x\|} \quad (3.50)$$

where

$$\eta_t = \frac{\int t |x(t)|^2 dt}{\|x\|^2} \quad (3.51)$$

$$\eta_f = \frac{\int f |X(f)|^2 df}{\|x\|^2} \quad (3.52)$$

In this study, the time bandwidth product is chosen as a measure of the support and the corresponding optimal Gaussian window is calculated as follows (Durak and Arikan, 2003):

$$g_{TBP}(t) = \exp\left(\frac{-\pi t^2 B_x}{T_x}\right) \quad (3.53)$$

Such an approach offers great convenience in processing all the sequences. Manually choosing a window for each process is not practical in reality. Another way is to pre-choose a window for the sequences in advance. It is simple but gives poorer results.

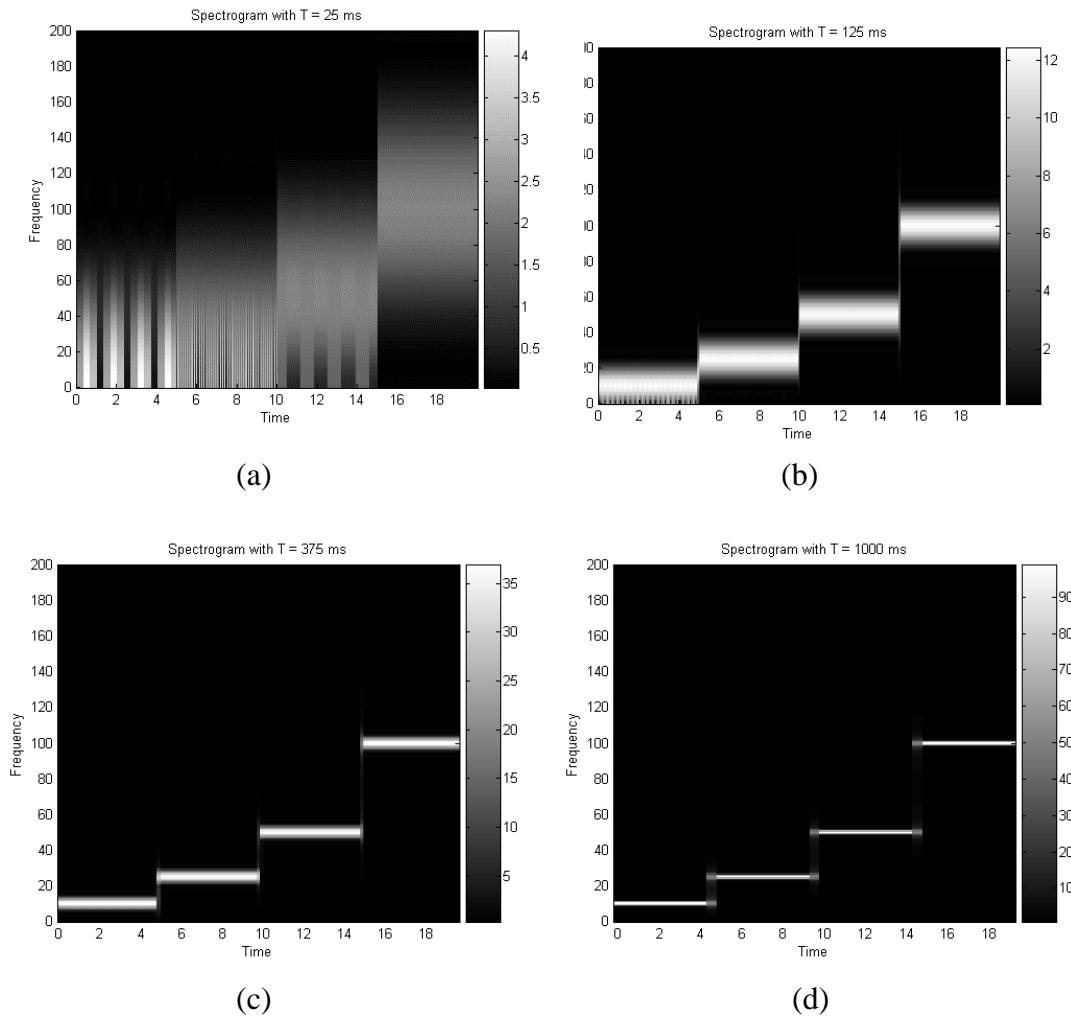


Figure 3.12 Spectrograms with different window width: (a) 25 ms; (b) 125 ms; (c) 375 ms; (d) 1000 ms

3.7.3 Spatial phase retrieval from a complex field

The interference phase distribution as shown in Figure 3.11 by digital holographic interferometry exhibits already low noise. It typically has a signal-to-noise ratio that is in the same range as that of an interference phase generated by a phase shifting method. In the interference phase distribution, a single correct value below π that is shifted slightly above π will appear as an isolated dark point in a neighborhood of bright points and vice versa. In order to produce a visually attractive interference phase

distribution and to permit a reliable phase unwrapping, a smoothing of the interference phase by digital filtering should be performed (Kreis, 2005).

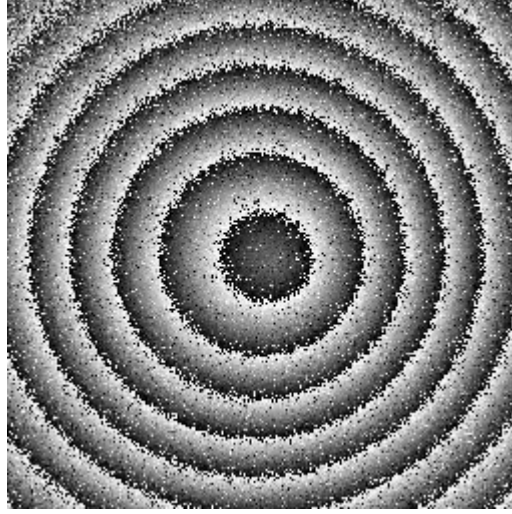


Figure 3.13 Unfiltered interference phase distribution

The most commonly used method is to subject the interference phase to a sine/cosine transformation before the filtering is accomplished (Creath, 1985). For such a filter, the distributions $s(n, m)$ and $c(n, m)$ are first calculated by:

$$s(n, m) = \sin[\Delta\varphi(n, m)] \quad (3.54)$$

$$c(n, m) = \cos[\Delta\varphi(n, m)] \quad (3.55)$$

They are both smoothed by a low-pass filter, e.g. one replacing each value by the average value over square $k \times k$ pixel neighbor. After filtering, the interference phase is then determined by:

$$\Delta\varphi_f(n, m) = \arctan \frac{s_f(n, m)}{c_f(n, m)} \quad (3.56)$$

However, the disadvantage is that each pixel is given an equal weight without considering the reliability of the pixel. As already mentioned, the intensity of each pixel is a good measure of the pixel's reliability. The real and imaginary part of the generated complex phasor is weighted implicitly by the square of the intensity modulation. Therefore, a more reliable smoothing technique is possible by using a low-pass filtering of the real and imaginary part.

A low-pass filtering of the real and imaginary part is actually a phasor average process to find the gravity of the phasors, as illustrated in Figure 3.14 (a). It is observed that a phasor with low amplitude and therefore less reliable phase values has less influence on the final results. The hollow circles represent phasors needed to be averaged while the filled circle is the resulting phasor. The sine/cosine transformation equals to a transformation into the complex field with amplitude 1 for all the pixels. It can be seen that the final result is dominated by less reliable phasors, as shown in Figure 3.14 (b).

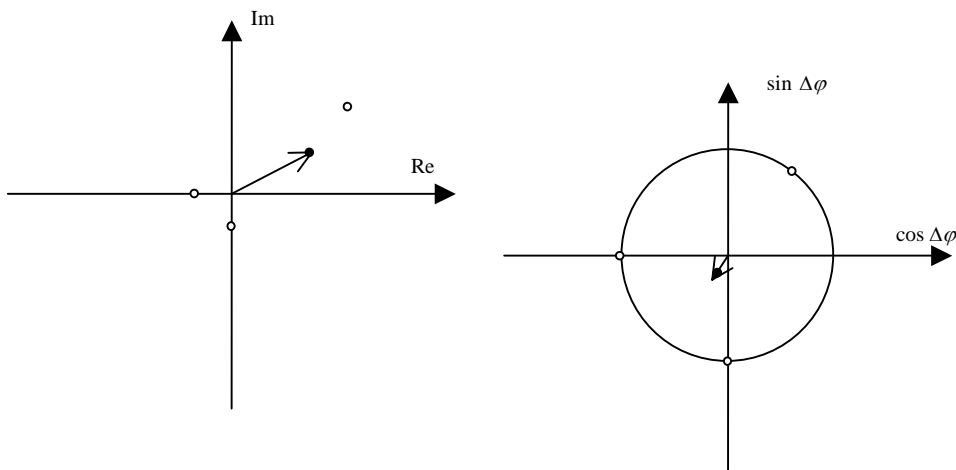


Figure 3.14 (a) Effect of filtering a phasor image; (b) effect of sine/cosine transformation

3.7.4 Combination of temporal phase retrieval and spatial phase retrieval

A distinguished feature of temporal phase unwrapping concept is its ability to retrieve absolute phase value. It makes no sense if the temporal phase retrieval procedure is done before spatial smoothing, since the erroneous spatial phase values will be temporally propagated. Actually, this agrees with the results of Huntley (1999). A modified temporal phase unwrapping process employed by Huntley shows much better results than those methods to implement spatial filtering before temporal phase unwrapping.

In this study, a comparison is always between the conventional method and the proposed methods in all experiments conducted. A flow chart of conventional method and proposed methods is given in Figure 3.15.

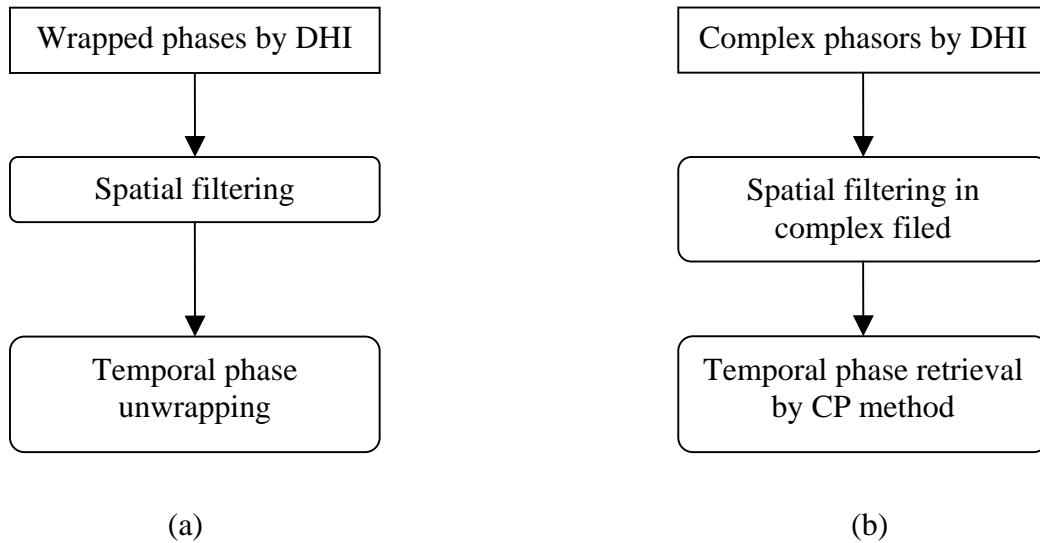


Figure 3.15 Flow chart of (a) conventional method (b) proposed method

Another advantage of filtering complex phasors spatially first is that it does not violate the linear assumption in Eq. (3.41) and the real amplitude of a particular pixel is prevented from changing drastically.

CHAPTER FOUR

DEVELOPMENT OF EXPERIMENTATION

To verify the proposed theoretical work, experimental systems for digital holographic interferometric measurement of the shape of a step-change object and a continuously deforming cantilever beam were developed. Other than that, a static deformation experiment is also conducted to verify the proposed spatial phase retrieval method. In the first section of this chapter, some equipment and specimen used in dynamic and static measurements are introduced. In the subsequent sections, experimental techniques used in these methods are described in detail.

4.1 Equipment for dynamic measurement**4.1.1 High speed camera**

The recording rate of a normal CCD camera is about 30 frames per second (fps). However, this is insufficient for most dynamic measurements as the low sampling rate means a violation of Nyquist sampling theorem and will probably lead to undersampling. A high speed camera is thus indispensable. In this investigation a high speed camera, Kodak Motion Corder Analyzer, Monochrome Model SR-Ultra is used (shown in Fig. 4.1). It is a compact monochrome high speed motion analyzing system designed for high speed application. It includes a full range of standard features, and optional accessories to record, view, measure and store the information required for high speed manufacturing.



Figure 4.1 Kodak Motion Corder Analyzer, Monochrome Model SR-Ultra

The sensor of the high speed camera has a pixel size of $7.4 \mu\text{m} \times 7.4 \mu\text{m}$ and an array of $658 \text{ pixels} \times 496 \text{ pixels}$. Its recording rate ranges from 30, to 10,000 fps. The size of an output image varies with the recording rate. At a recording rate of 125 fps which is commonly used in experiments, the output images have $512 \text{ pixels} \times 480 \text{ pixels}$. If using the highest recording rate of 10,000 fps, the image size will reduced to $128 \text{ pixels} \times 34 \text{ pixels}$ and 30,832 images can be recorded within 3.0 seconds. The camera has a standard 8-bit monochrome BMP or TIFF output with 256 gray levels. It is also compatible with all C-mount camera lenses.

4.1.2 PZT translation stage

A piezoelectric translation stage with a computer controlled system is one of the key equipment to ensure precise loading of the beam in dynamic digital holographic measurement. It can be used to prescribe a linear or nonlinear displacement. The translation stage used is a Piezosystem Jena, PX 300 CAP PZT stage, as shown in Figure 4.2. It is capable of generating a maximum horizontal displacement of $300 \mu\text{m}$. It contains a closed loop capacitive control system with a position accuracy of 0.05%

at a full motion of 300 μm . It has a resolution of 1 nm and works well for high precision positioning. It has a maximum load of 10N.

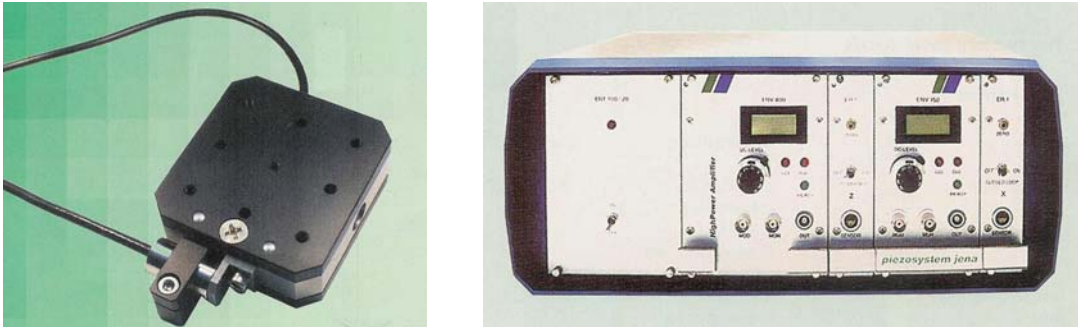


Figure 4.2 PZT translation stage (Piezosystem Jena, PX 300 CAP) and its controller

4.1.3 Stepper motor travel linear stage

The linear stage is used to mount and move the fiber optics at a constant speed to illuminate the object in shape measurement. A Newport UTM 150 mm mid-range travel steel linear stage, as shown in Figure 4.3, is used. It is a high-power DC-servo version with a resolution of 1 μm . The stage features a built-in tachometer to provide superior speed stability, with a travel range of 150 mm and a maximum speed up to 20 mm/s.

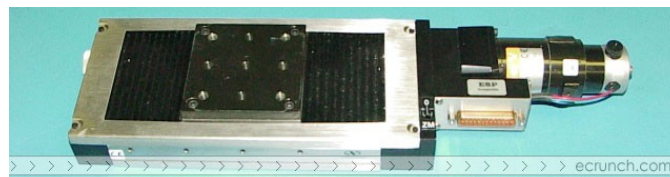


Figure 4.3 Newport UTM 150 mm mid-range travel steel linear stage

The Melles Griot 17 MDU 002 shown in Figure 4.4 is designed to drive and control the linear stage. The operation of the stepper actuator is controlled by software within the primary and satellite processors. A simple communications protocol

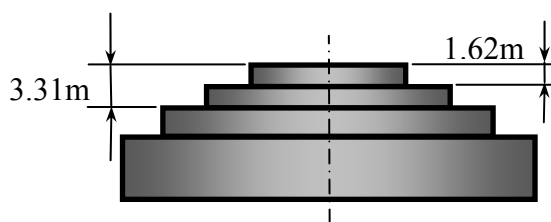
provides the user access to positioning functions. Furthermore, the software automatically compensates for positioning errors, producing accuracy comparable to that of a linear encoder system.



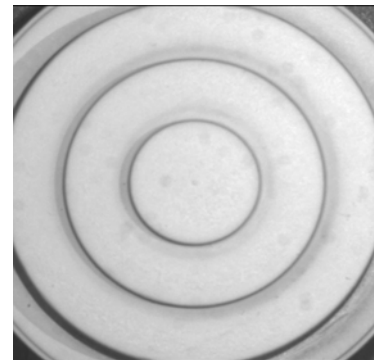
Figure 4.4 Melles Griot 17 MDU 002 NanoStep Motor Controller

4.1.4 Specimens

The specimen tested in the multi-illumination-point is an object with a step-change profile. Figure 4.5 (a) shows the dimensions of the object. The heights of the steps are respectively 1.62 ± 0.01 mm and 3.31 ± 0.01 . Figure 4.5 (b) shows the top view of the object.



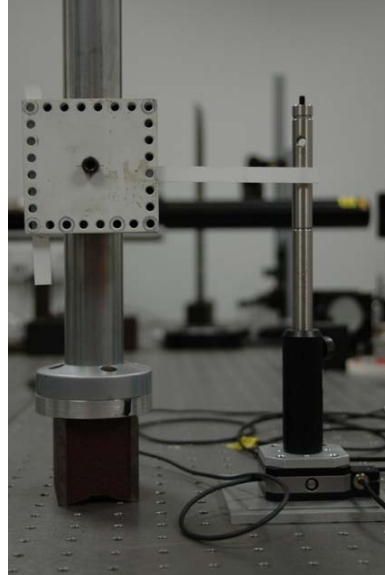
(a)



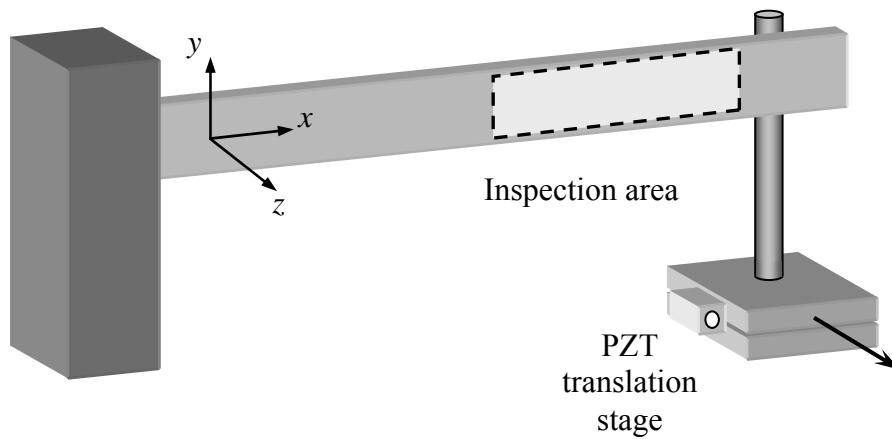
(b)

Figure 4.5 (a) Dimension of a step-change object; (b) top view of the specimen with step-change

The specimen used for the continuously deforming measurement consists of cantilever beam painted white to increase the reflectivity. The cantilever beam is loaded by a computer-controlled piezoelectric transducer (Figure 4.6 (a)). The area to be inspected is shown in Figure 4.6 (b).



(a)



(b)

Figure 4.6 (a) A cantilever beam and its loading device; (b) Schematic description of loading process and inspected area

4.2 Equipment for Static Measurement

4.2.1 High resolution digital still camera

The recording device for the static deformation measurement is shown in Figure 4.7. As Eq. (3.10) implies, a restriction exists for the interference angle between the object wave and the reference wave due to the limited resolution of current digital still camera. Smaller pixel size means better resolution. The Pulnix TM-1402 is employed as the recording medium in static measurement. It is a miniature, high resolution (1.4 megapixels), monochrome, progressive scan CCD camera. Its resolution reaches 1392 x 1040 pixels and the frame rate can be adjusted to 15 or 30 frames per second. The TM-1402CL has a patent-pending look-up table (LUT). Applications include machine vision, medical imaging, ITS, character recognition and more.

4.2.2 Specimen

The advantage of spatial phase retrieval from complex field is demonstrated by the deformation of a circular thin plate. The aluminum plate is shown in Figure 4.8. The deformation is introduced by manually loading of the micrometer.



Figure 4.7 Pulnix TM-1402

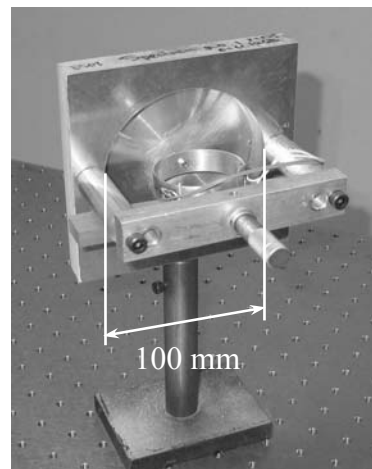


Figure 4.8 A circular plate centered loaded

4.3 Experimental setup

As discussed in the theory chapter, digital lensless Fourier holography displays several advantages over the Fresnel digital holography using plane wave: (a) full usage of the bandwidth of the CCD sensor; (b) shorter recording distance; (c) Simpler reconstruction algorithm. In the following experiments, all experimental setups employ digital lensless Fourier holography.

4.3.1 Multi-illumination method

In the experiment, linear phase change is achieved through translating an illuminating fiber optics at a constant speed as shown in Figure 4.9. A specimen with step change surface as shown in Fig 4.5 is used for surface contour measurement. A He-Ne laser light beam of 632.8 nm wavelength is split into two beams by a fiber coupler. The fibre end with a 90% beam output (object beam) is mounted on a linear translation stage shown in Figure 4.3. The fiber end with a 10% output is used as a reference beam. The object and reference beams are then recombined by a beam splitter. To employ digital lensless Fourier holography, the distance between the object and the beam splitter has to be the same as the distance between the reference fiber end and the beam splitter. The object has a distance of 45 cm from the CCD sensor. The high speed CCD camera is used to record digital holograms at 125 frames per second. Five hundred digital holograms are recorded and 129 consecutive images are selected for processing.

4.3.2 Measurement of continuously deforming object

A He-Ne laser (75 mW, $\lambda = 632.8$ nm) is divided into reference and object beams by a variable beamsplitter, as shown in Figure 4.10. Two spatial filters consisting of a

microscopic lens and a small pinhole are used to produce a spherical wave. A collimating lens is placed in front of one of the pinholes to generate a desired plane object wave. An angle (θ) between the illumination and observation directions is taken as 60° in the experiment. The specimen is a cantilever beam shown in Figure 4.6. In the experiment, a linear loading is applied by using the triangular wave function and the inspection area of the beam is $10\text{ mm} \times 50\text{ mm}$. A high speed CCD camera is used with a sampling rate of 125 frames per second. A total of 564 consecutive digital holograms were captured during the process and 481 holograms are used for processing. The static deformation measurement is also conducted using the same setup as Figure 4.10. The beam in Figure 4.6 (b) is replaced by the plate in Figure 4.8.

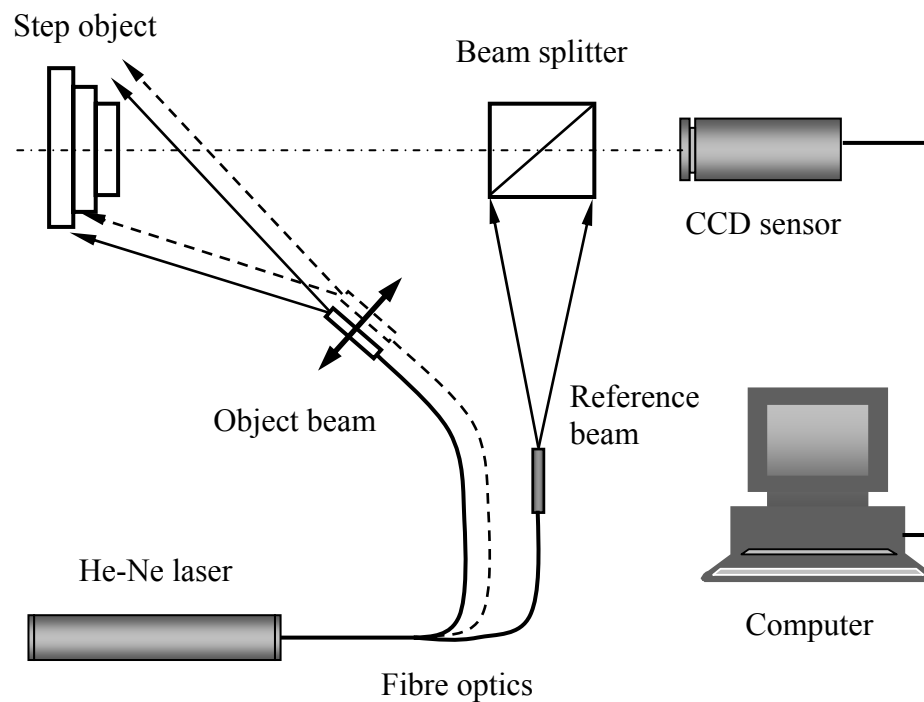


Figure 4.9 Optical arrangement for profile measurement using multi-illumination-point method

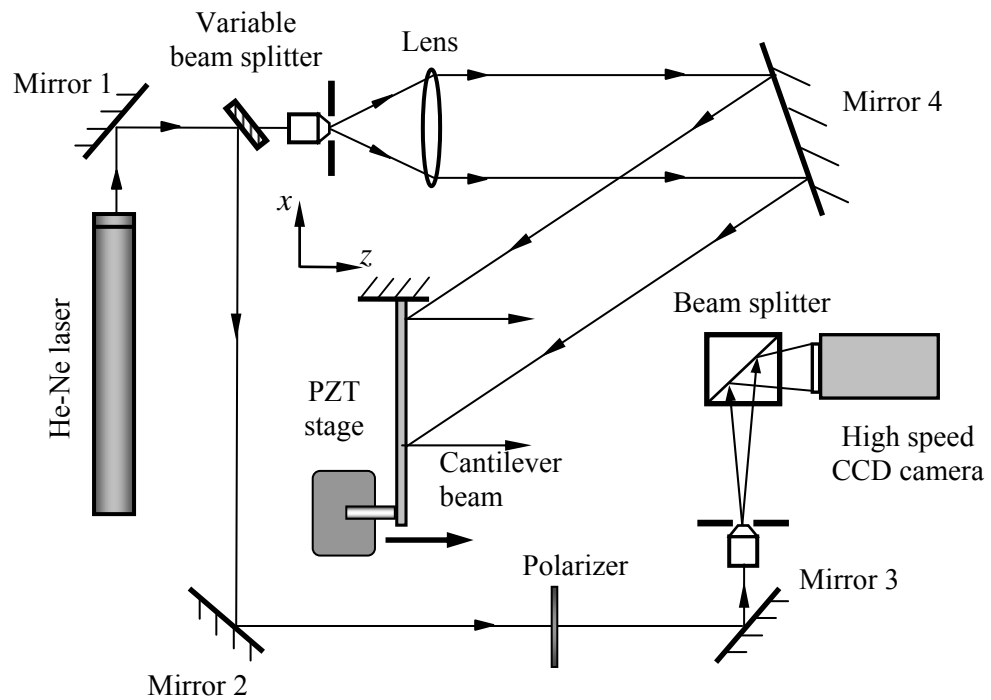


Figure 4.10 Digital holographic setup for dynamic deformation measurement

CHAPTER FIVE

RESULTS AND DISCUSSION

In this chapter, the experimental results are presented in details according to different holographic interferometric applications. The experiments can be categorized into two kinds: static and dynamic. In the static experiments, the basic techniques that will be used in dynamic processing are verified first. The spatial phase retrieval technique based on the proposed CP method is demonstrated in the plate deformation experiment. The results of temporal complex phasor analysis on profiling object surface with step change and instantaneous velocity and displacement measurement on continuously deforming objects are presented. Temporal DPS method is used mainly to generate results for comparison. All temporal CP and DPS algorithms are executed using Visual C++.

5.1 D.C-term removal

As discussed in theory chapter, several techniques are proposed to get rid of the D.C-term from the intensity display of reconstructed image. The objective of this study is to develop new techniques for high speed measurement in digital holographic interferometry, thus, it is quite hard to employ the techniques with extra experiments efforts in our experiments. Therefore, the pure numerical methods are used in our experiment. Although it is claimed that either mean value subtraction or high pass filter technique could do the job well, we find that a combination of these two techniques leads to a better result.

Figure 5.1 shows a typical digital hologram recorded in an off-axis Fresnel digital holography set up using plane wave as reference wave by Pulnix TM-1402. As already mentioned, holography is a clever combination of interference and diffraction. It can be observed from Figure 5.1 that the digital hologram is made of microscopically fine interference patterns produced by the coherent superposition of an object and a reference wave.

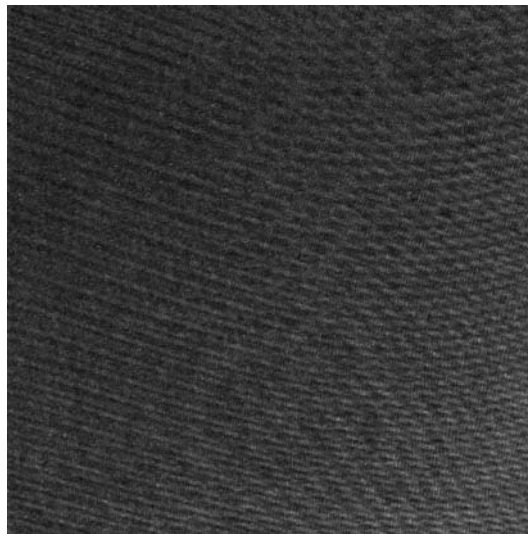


Figure 5.1 A typical digital hologram

The corresponding reconstruction of the digital hologram in Figure 5.1 is displayed in Figure 5.2. Its D.C.-term is eliminated by a combination of mean value subtraction and high-pass filtering techniques. The recorded object is a merlion. However, as shown in Figure 5.3, neither mean value subtraction nor high-pass filtering technique will achieve satisfactory results.

As for digital lensless Fourier holography, a similar result is observed. Figure 5.4 (a) shows a hologram from digital lensless Fourier holography setup while Figure 5.4 (b) is its corresponding reconstruction image with D.C.-term eliminated. Figure 5.5

demonstrates the result processed either by the mean value subtraction or high pass filter. The object here is a plate illuminated by collimated illuminating wave.

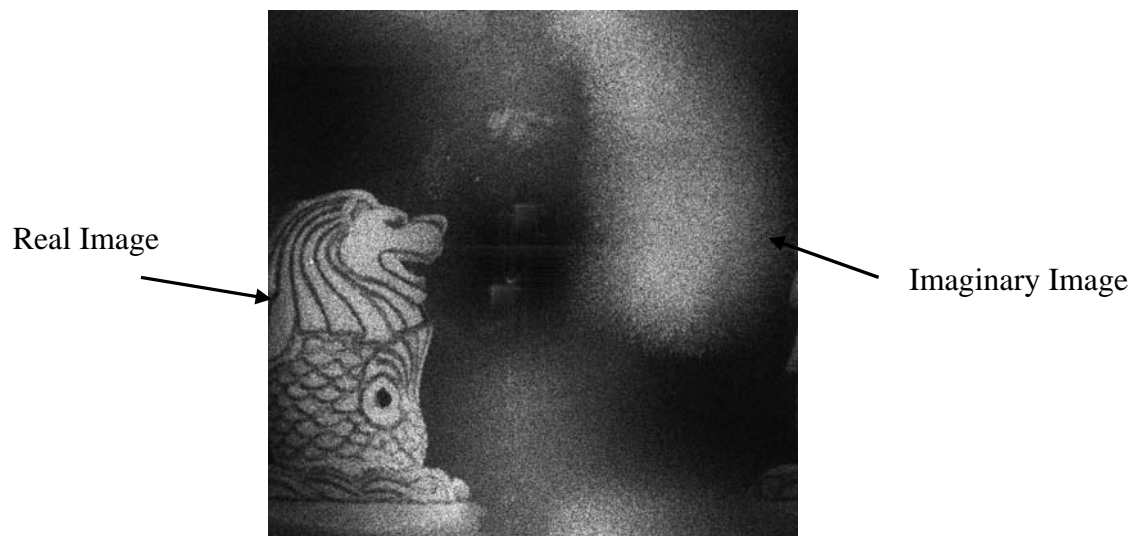


Figure 5.2 Intensity display of a reconstruction with D.C.-term eliminated

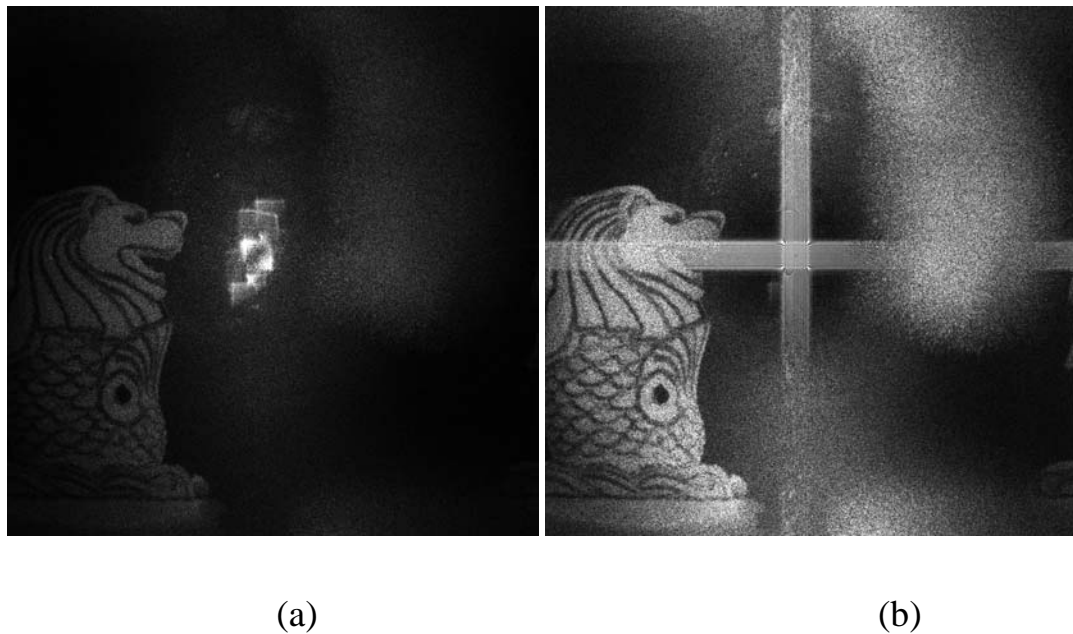
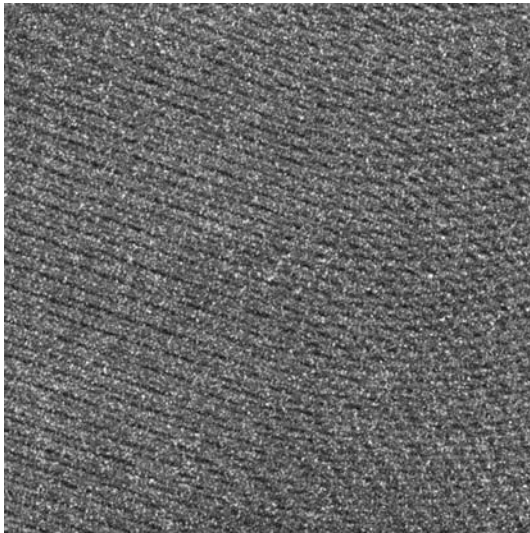
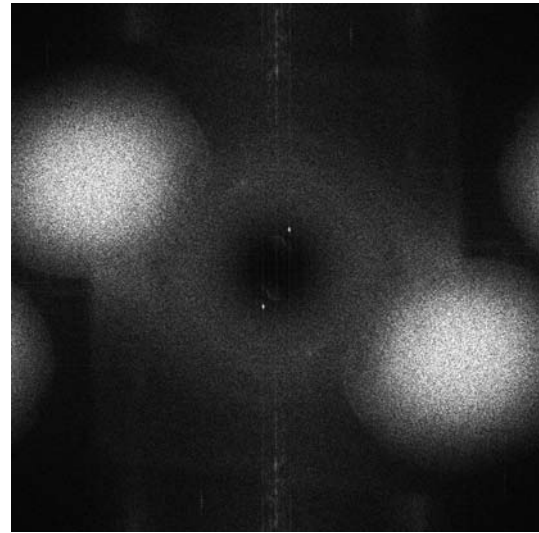


Figure 5.3 Intensity display of reconstruction: (a) with average value subtraction only; (b) with high-pass filter only.

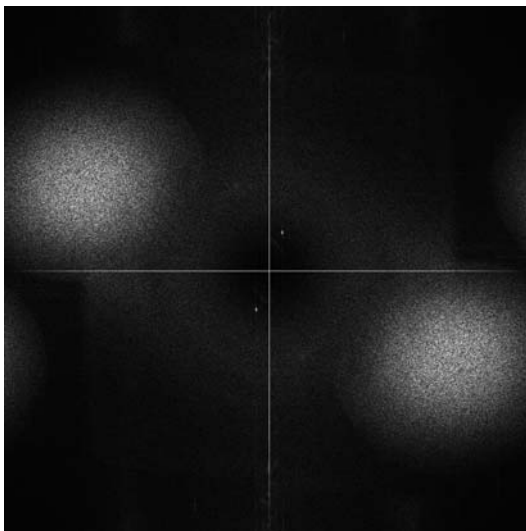


(a)

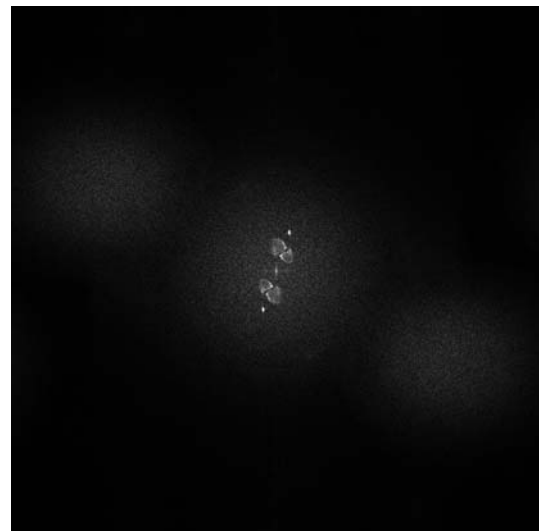


(b)

Figure 5.4 (a) digital hologram in digital lensless Fourier holography; (b) Its corresponding intensity display of reconstruction with D.C.-term eliminated



(a)



(b)

Figure 5.5 Intensity display of reconstruction: (a) with average value subtraction; (b) with high-pass filter only

5.2 Spatial CP method

The deformation measurement is conducted to verify proposed spatial phase retrieval method. The plate undergoes two states, one is undeformed and the other one deformed. The loading is realized by the micrometer just at the center of the plate. One digital hologram is recorded first. After loading, another digital hologram is recorded. The two digital holograms are reconstructed separately, from which two phase distributions are obtained. The interference phase is calculated by Eq. (2.27). The above approach referred to as DPS is commonly used in digital holographic interferometry. Figure 5.6 illustrates DPS process flow using images from plate deformation experiment. The experiment setup is exactly the same as the one shown in Figure 4.10. It is observed that the interference pattern covers only a portion of the whole image. Therefore, the area of interest has to be selected manually to analyze, which is actually the biggest disadvantage of digital holographic interferometry. The procedure of spatial phase unwrapping of digital holographic inference phase maps is shown in Figure 5.7. Due to the speckle noise inherent to laser techniques, a spatial filtering has to be carried out before phase unwrapping to limit the spatial propagation of errors. The filtering technique used here is the sine/cosine transformation low-pass filter.

In Figure 5.7, a 3D plot of the unwrapped interference phase is given. It can be seen that the unwrapped phase goes from -10 to 35 rad, which is actually a relative measurement. It will give rise to problems when calibration is needed, for a point whose movement is 0 has to be found first.

As to the fringes whose signal to noise (SNR) are high, the result of the commonly used method is acceptable, as shown in Figure 5.7. If some areas are

heavily polluted by noise, the sine/cosine transformation low-pass filter will appear clumsy.

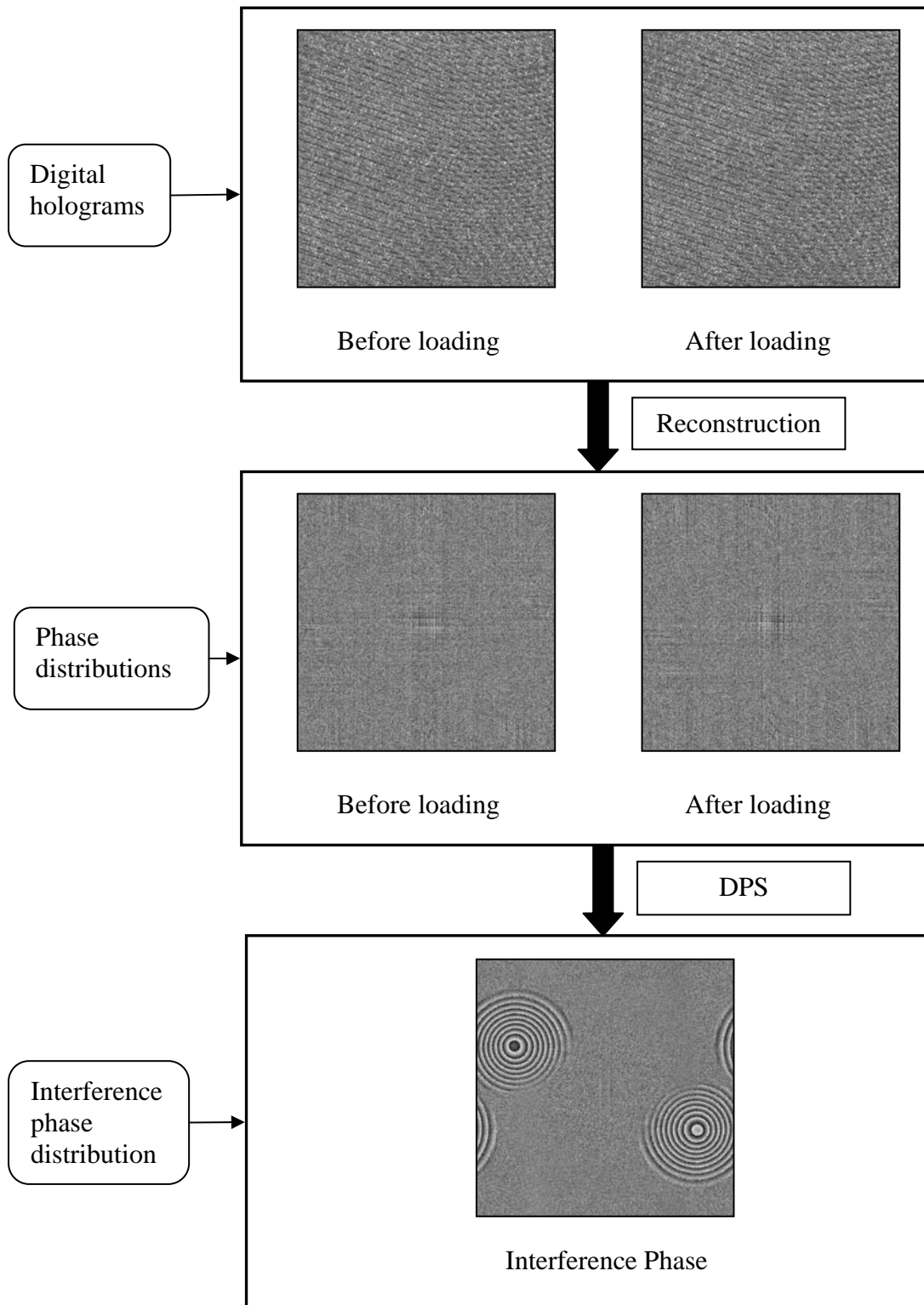


Figure 5.6 Process flow of digital holographic interferometry

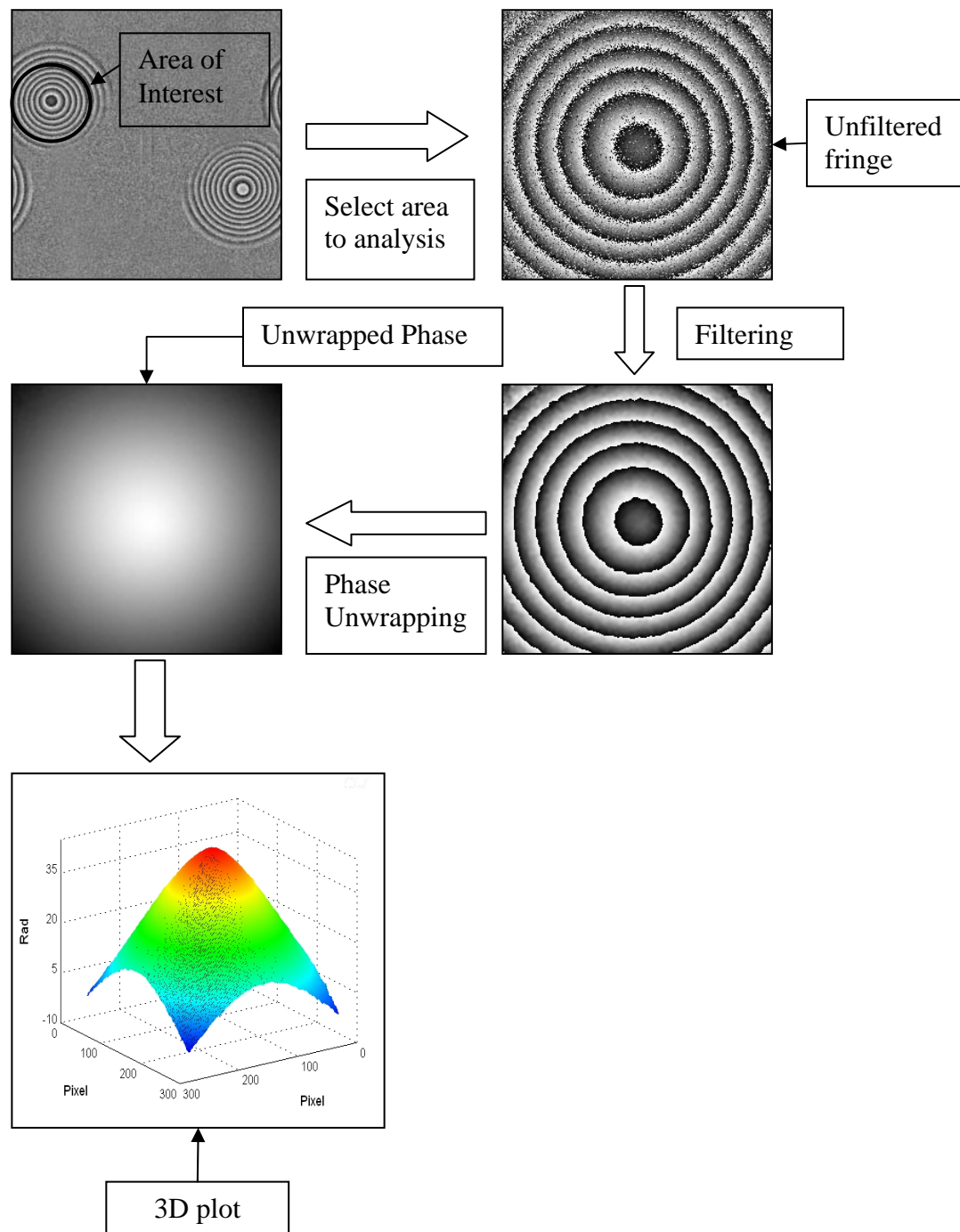


Figure 5.7 Spatial phase unwrapping

A comparison of proposed CP method and DPS method is conducted in Figure 5.8. It is seen that the fringe pattern has better quality at center than at edges. An area of the pattern at the edges is chosen for analyzing. A first check of residues of the area

is first done before any processing. As many as 596 residues are detected from the raw data.

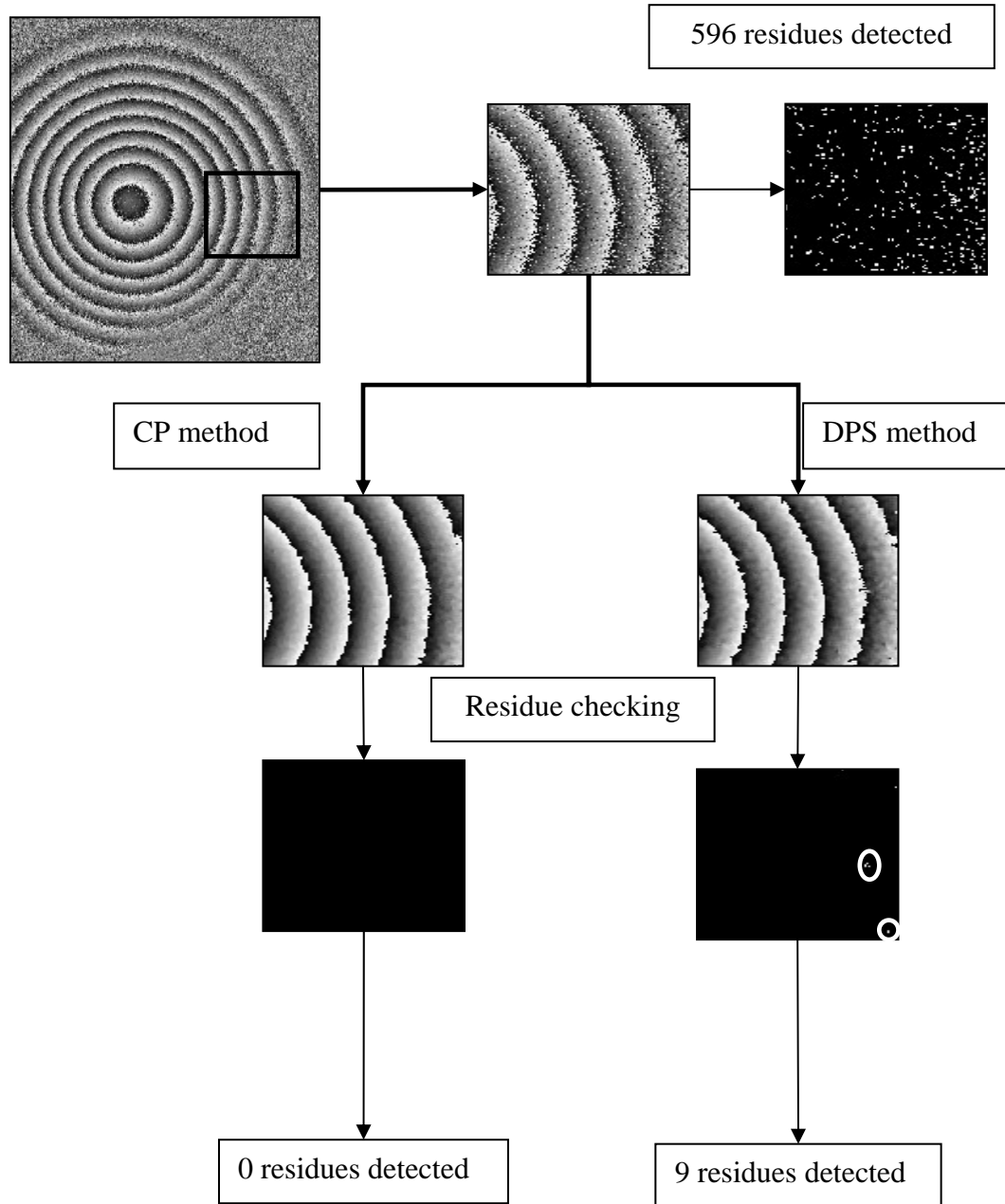


Figure 5.8 Spatial phase retrieval by CP method

In the proposed CP method, a complex phasor map is first produced by the Eq. (3.32). The real part and imaginary part of the complex phasor is low-pass filtered separately and the filtered interference map is determined by Eq. (3.33).

In DPS method, the low-pass filtering is done after the sine/cosine transform. The result by CP method looks obviously better than by DPS method. The residues of both results are checked then. No residues is found in CP method's result while 9 residues are found in the result of DPS method. Such a comparison verifies that the proposed CP method is more effective than DPS method.

5.3 Temporal CP method in dynamic measurement

In temporal phase analysis, the concept is quite different. No spatial processing exist any more if the spatial smoothing before any temporal processing is not accounted. The sequence of complex phasor maps are processed point by point by CP method, while the sequence of interference phase maps are processed in DPS method for comparison.

5.3.1 Surface profiling on an object with step change

As mentioned in chapter 4, 546 digital holograms are recorded by high speed camera while the fiber is moving at constant velocity. Figure 5.9 shows a digital hologram recorded by the high speed camera.

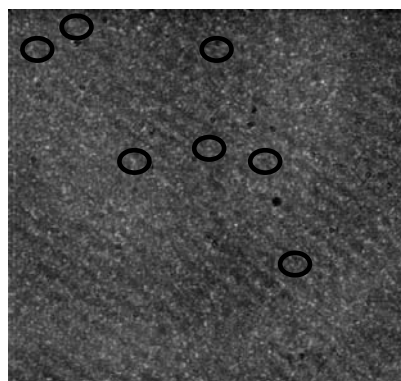


Figure 5.9 Digital hologram in surface profiling experiment (particles are highlighted by circles)

Due to particles on the surface of the CCD sensor, the recorded digital hologram is also polluted. But these particles will not influence the reconstruction image, as shown in Figure 5.10, for each single pixel of digital hologram records the information of whole object.

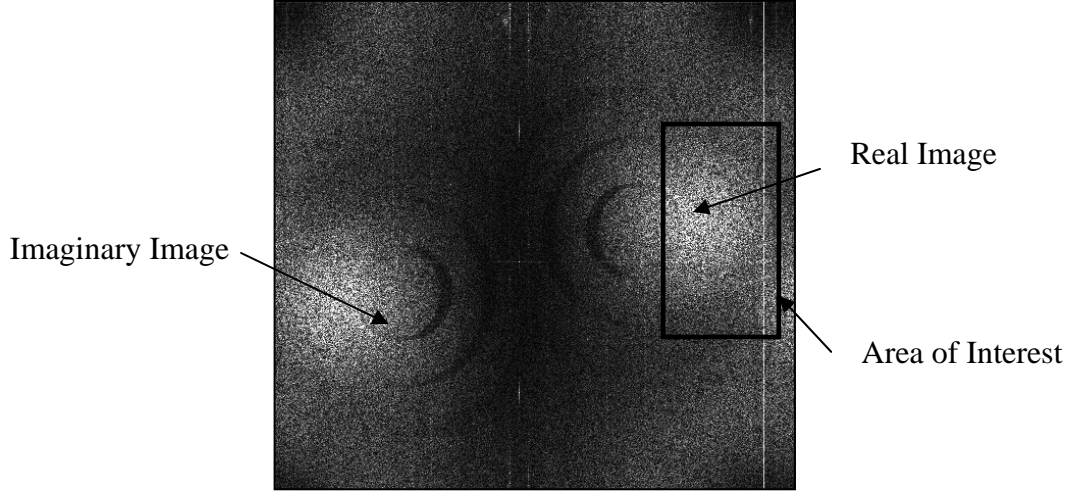


Figure 5.10 Reconstruction of Figure 5.9

The process flow of DPS method is illustrated in Figure 5.11. 129 consecutive images out of 546 recorded images are selected for processing. Such a number is already sufficient to obtain a satisfying result by temporal phase unwrapping. In addition, 128 interference maps are much easier to implement FFT algorithm. As a comparison, the conventional DPS approach is also carried out: a sequence of phase maps is obtained by reconstructing the sequence of digital holograms using 2D FFT algorithm. The interference phase map between instant t_n and t_0 is calculated by $\Delta\varphi_w(n,0) = \varphi_n - \varphi_0$. The number of 2π phase jumps between two successive wrapped interference phases is determined by Eq. (3.27). The total number of phase jumps $\nu(t)$ is calculated by Eq. (3.28) and the phase unwrapping is carried out by Eq. (3.30). For the temporal phase unwrapping is carried out pixelwise, a given point is selected for

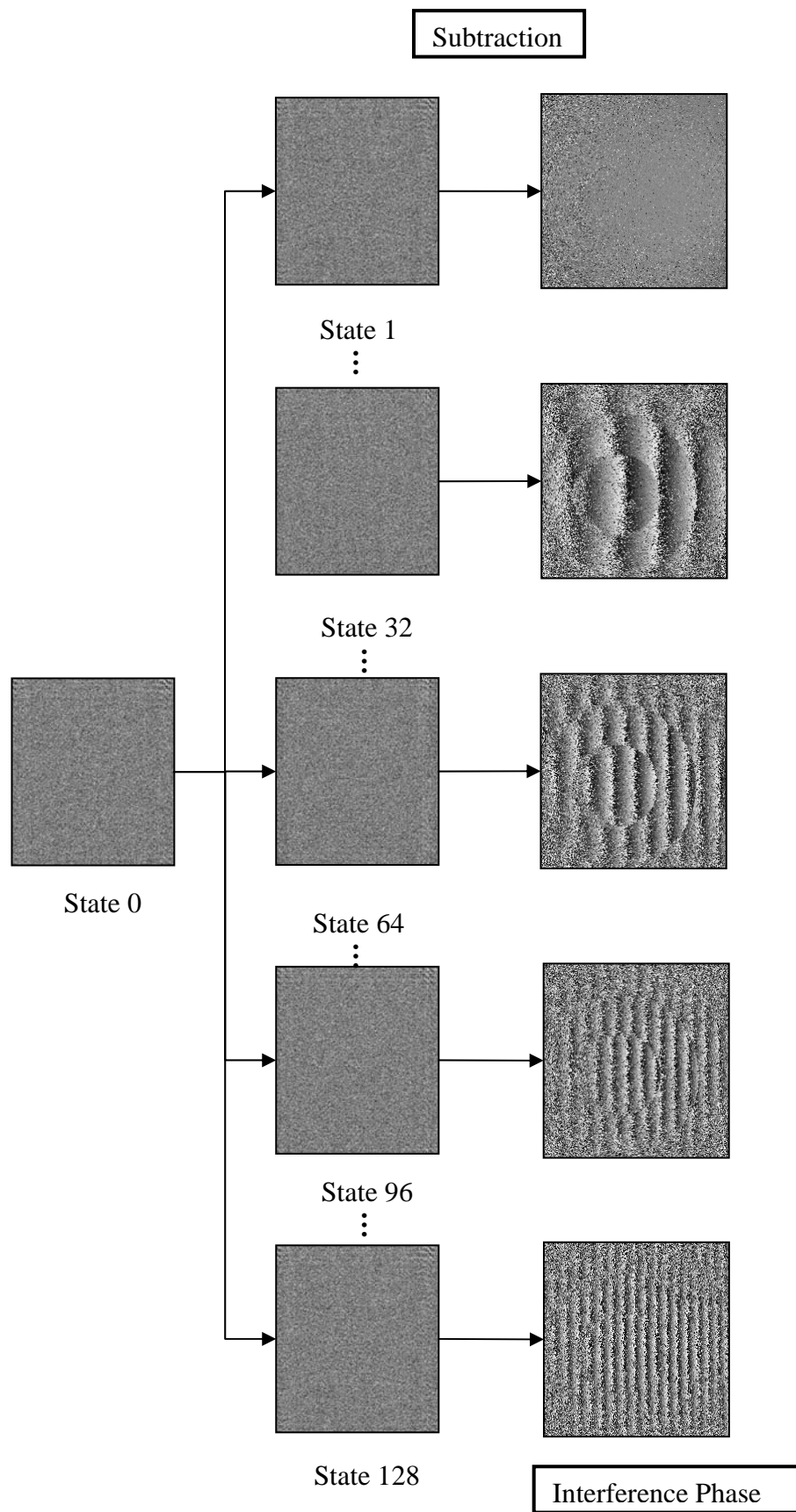


Figure 5.11 DPS method

explanation. Figure 5.12 (a) illustrates how the interference phase of such a pixel varies with time while its unwrapped phase is given in Figure 5.12(b). The unwrapped phase for the area of interest and its corresponding 3D plot is shown in Figure 5.13. It is observed that the surface is polluted by spiky noise. At regions of step changes, the noise is especially high. The reason is that the illumination at these places is usually poor. Therefore, a consideration of intensity value is necessary when phase retrieval is carried out. Further more, the surface of object calculated by the conventional approach is not smoothed.

The experimental data are then processed by proposed CP method to see if better results can be obtained. Those recorded digital holograms are first reconstructed by 2D FFT. Complex phasor maps are obtained using Eq. (3.32) between state 0 and state n . Such a procedure is similar to the one shown in Figure 5.11. The first algorithm tested is temporal Fourier transform algorithm. Also, a given pixel is selected for analysis. Its phase and intensity variation with time are given in Figure 5.14. The sequence of complex phasors is Fourier transformed into frequency domain, the spectrum is demonstrated in Figure 5.15. Then exact position of the peak in frequency is picked up by the proposed temporal Fourier transform algorithm. The peak's position lies at -7.6239 while the estimation is -8. Then the frequency is calculated by Eq. (3.37). Now that we got the phase changing rate (frequency), it is much easier to determine the unwrapped phase. A simple integration will get the job done. The unwrapped phase for this pixel is displayed in Figure 5.16. Such a procedure is repeated until every pixel is covered. The final result is illustrated in Figure 5.17. Compared with Figure 5.13 (a), the unwrapped phase is improved and the spiky noise is eliminated. However, the edges of the steps are still not uniform, as shown in Figure 5.17 (a).

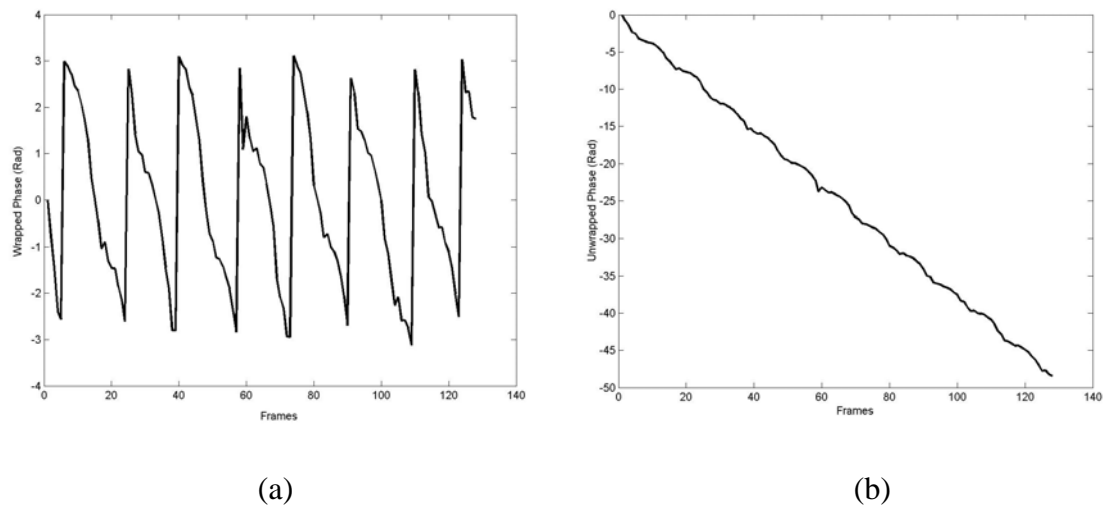


Figure 5.12 (a) Wrapped phase for a given point; (b) Unwrapped phase for a given point

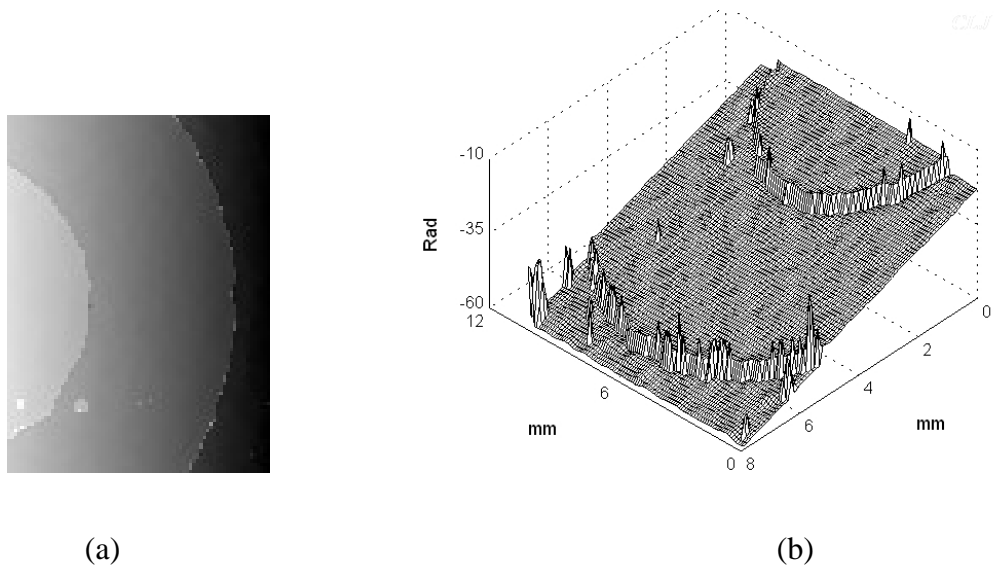


Figure 5.13 (a) Unwrapped phase; (b) corresponding 3D plot.

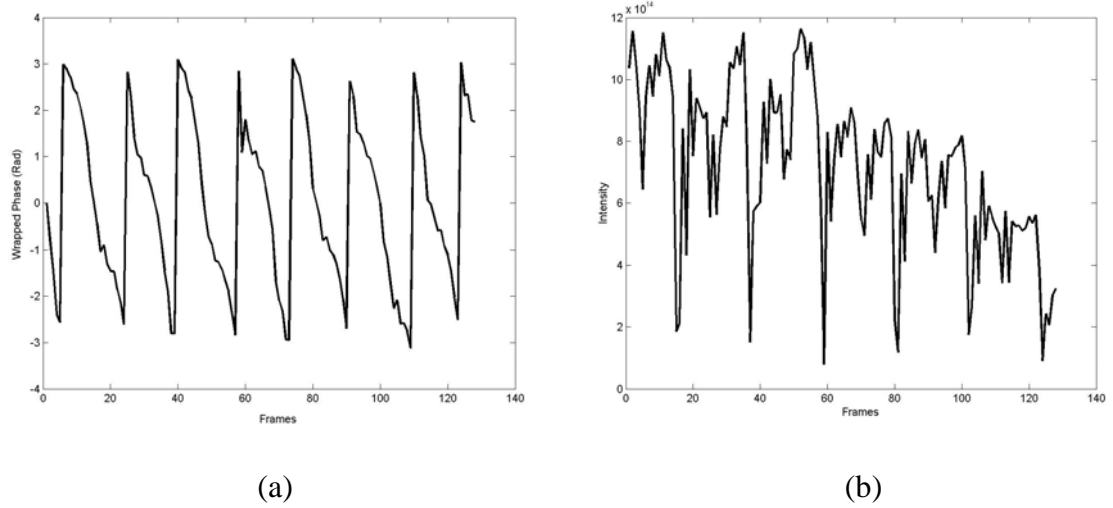


Figure 5.14 (a) Phase variation of a pixel; (b) intensity variation of a pixel

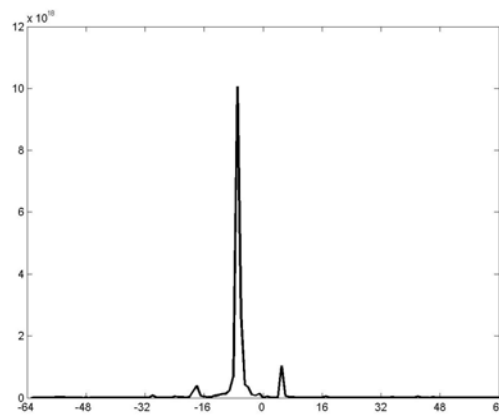


Figure 5.15 Frequency spectrum of a pixel

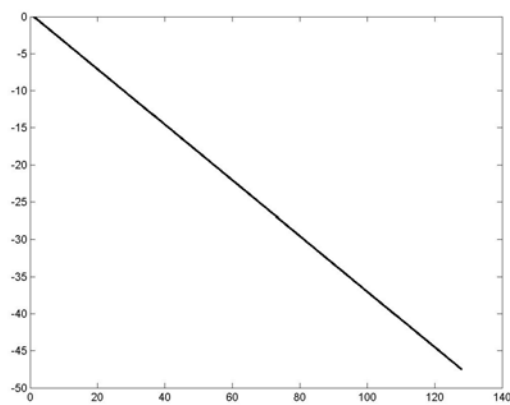


Figure 5.16 Unwrapped phase by integration

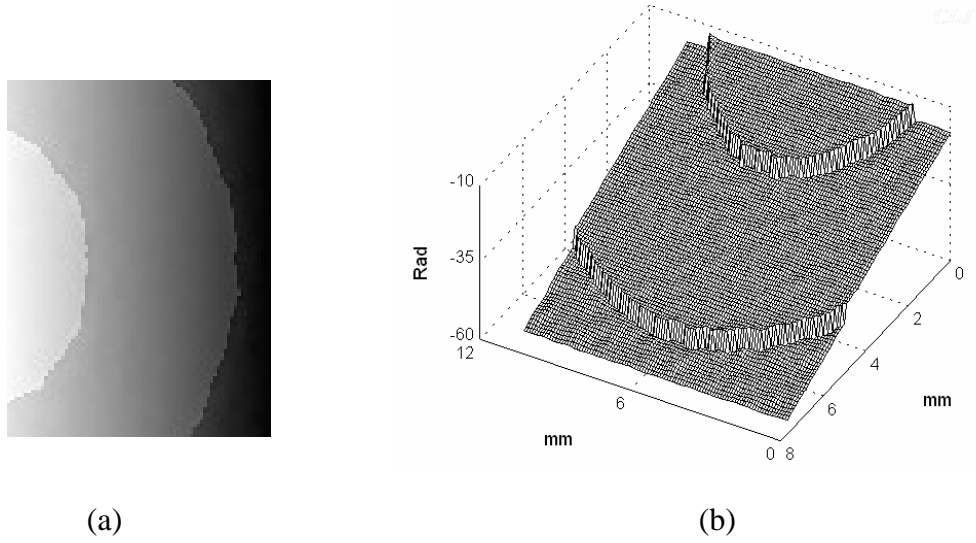


Figure 5.17 Results calculated by temporal Fourier transform algorithm: (a) unwrapped phase; (b) 3D plot

The reason is that temporal Fourier transform algorithm requires linear phase changing rate which is quite hard to achieve in experiment. Although improved, the result still doesn't reach our requirement.

The second algorithm verified is temporal STFT filtering. It has no such limitation as linear phase changing rate. Thus, it has a much wider application. Still, a given pixel is selected. As indicated in Eq. (3.39), the integration limits have to be determined in advance. It is already discussed in Chapter 3 how to calculate such limits: the peak is picked up by the temporal Fourier transform algorithm first. The bandwidth is set as 5. For the given pixel, the integration limits goes from -0.47 to -0.27. The wrapped phase and unwrapped phase for that pixel are given in Figure 5.18. Similarly, the same procedure is done for every pixel. The unwrapped phase and its 3D plot are given in Figure 5.19. Compared with previous two results, we can see temporal STFT filtering algorithm achieves the best result. The uniformity at edges of step is much improved and the surface is much smoother. It again verifies that our proposed CP concept is more effective in eliminating noise than conventional method.

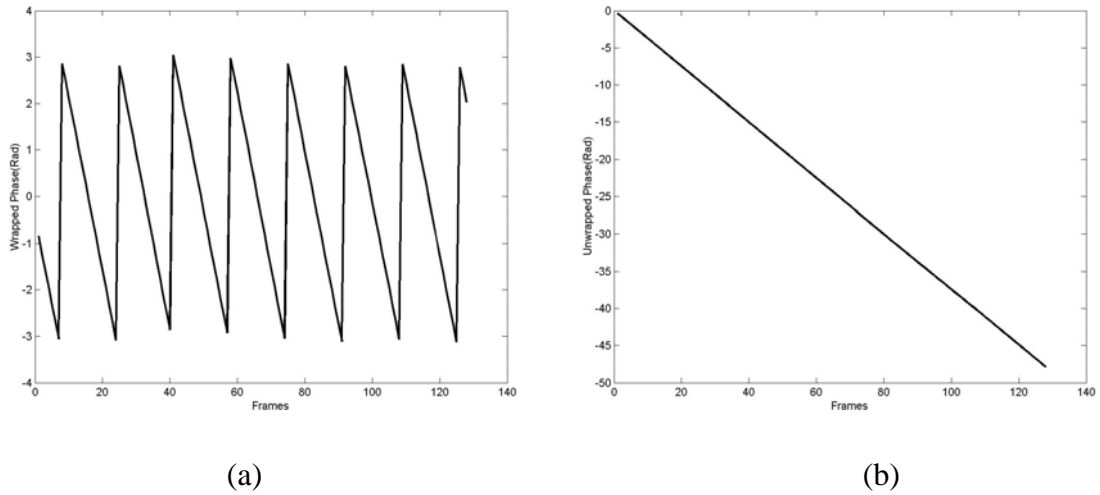


Figure 5.18 Result for a pixel by temporal STFT filtering: (a) Wrapped phase; (b) Unwrapped phase

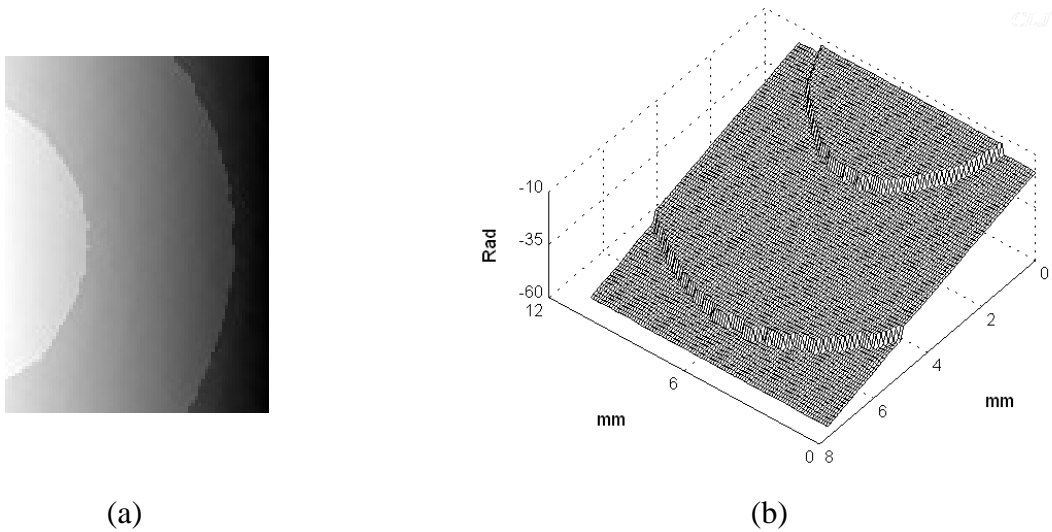


Figure 5.19 Results calculated temporal STFT filtering algorithm: (a) unwrapped phase; (b) 3D plot

Another thing need to notice is how to determine a proper window for each sequence. Although STFT has the uncertainty relationship between the frequency and time resolution, temporal STFT filtering algorithm is just a transformation and inverse transformation process. Choosing a proper window for each sequence is not as critical as the ridge extraction algorithm to be discussed next section. In order to get a faster

and simpler algorithm, the window is fixed for all sequences. In our experiment, the window width is selected as 10 frames for all sequences.

5.3.2 Measurements on continuously deforming object

In the previous section, the object is static while the fiber end moves continuously. The fringes are generated between different states due to the changing reference wave. In this section, the beam undergoes continuously deformation while the reference wave keeps unchanging. The objective is to measure displacement and velocity of each pixel simultaneously, which is impossible to be achieved by conventional spatial and temporal methods.

Velocity is nothing but the first derivative (instantaneous frequency) of displacement. As discussed in Chapter 3, the proposed temporal ridge extraction algorithm is able to retrieve instantaneous frequency. The continuous loading of beam is realized by PX 300 CAP PZT stage, which can generate kinds of wave. In the experiment, triangular wave is chosen to be the wave function. Figure 5.20 shows a triangular wave generated by the PZT stage. Only the increasing part of the triangle wave within a period is needed. The input voltage has to be adjusted carefully to make sure that the fringes are not too dense.

During the continuous loading, 546 digital holograms are recorded, out of which 481 consecutive images are selected for further processing. Figure 5.21 shows a digital hologram recorded during the process and the intensity display of its reconstruction. After all the holograms are reconstructed, the interference maps are obtained by DPS method, as shown in Figure 5.11. Figure 5.22 illustrates how the interference phase maps vary with time. A schematic description of the whole process is given in Figure

5.23. Three points are selected from the inspection area for analysis and comparison. A typical fringe pattern in the experiment is shown in Figure 5.24 and the three selected points are denoted by A, B and C. The unwrapped phase by DPS method for frame 480 is shown in Figure 5.25. Some bad pixels are observed.

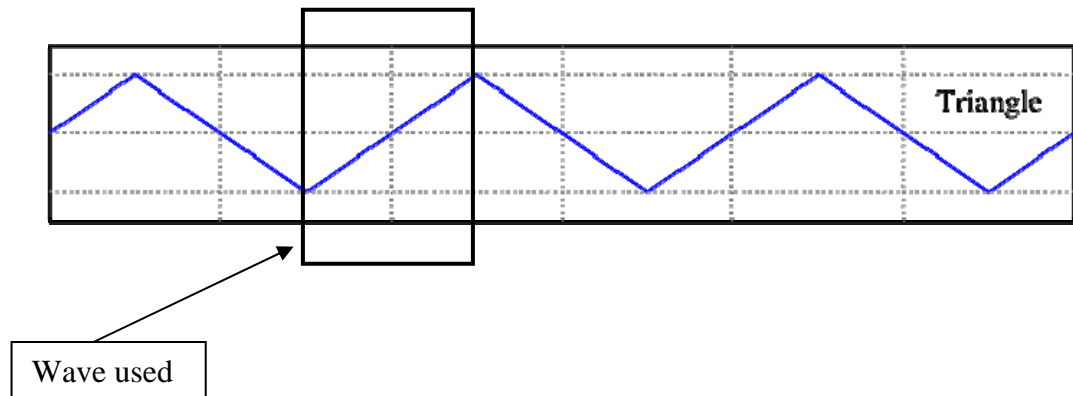


Figure 5.20 Triangular wave by PZT stage

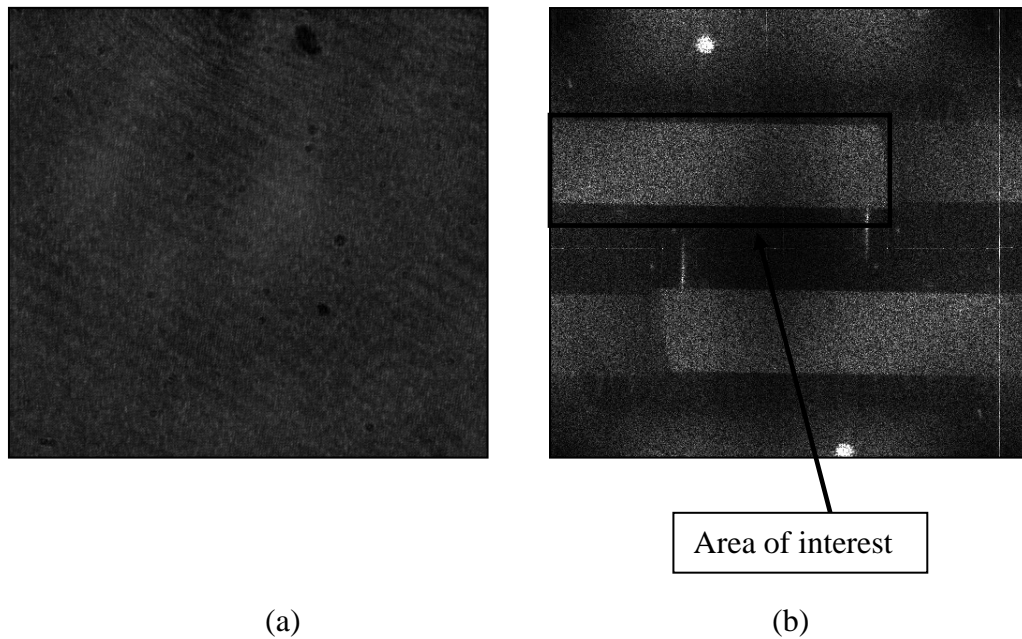


Figure 5.21 Digital hologram and its intensity display of reconstruction

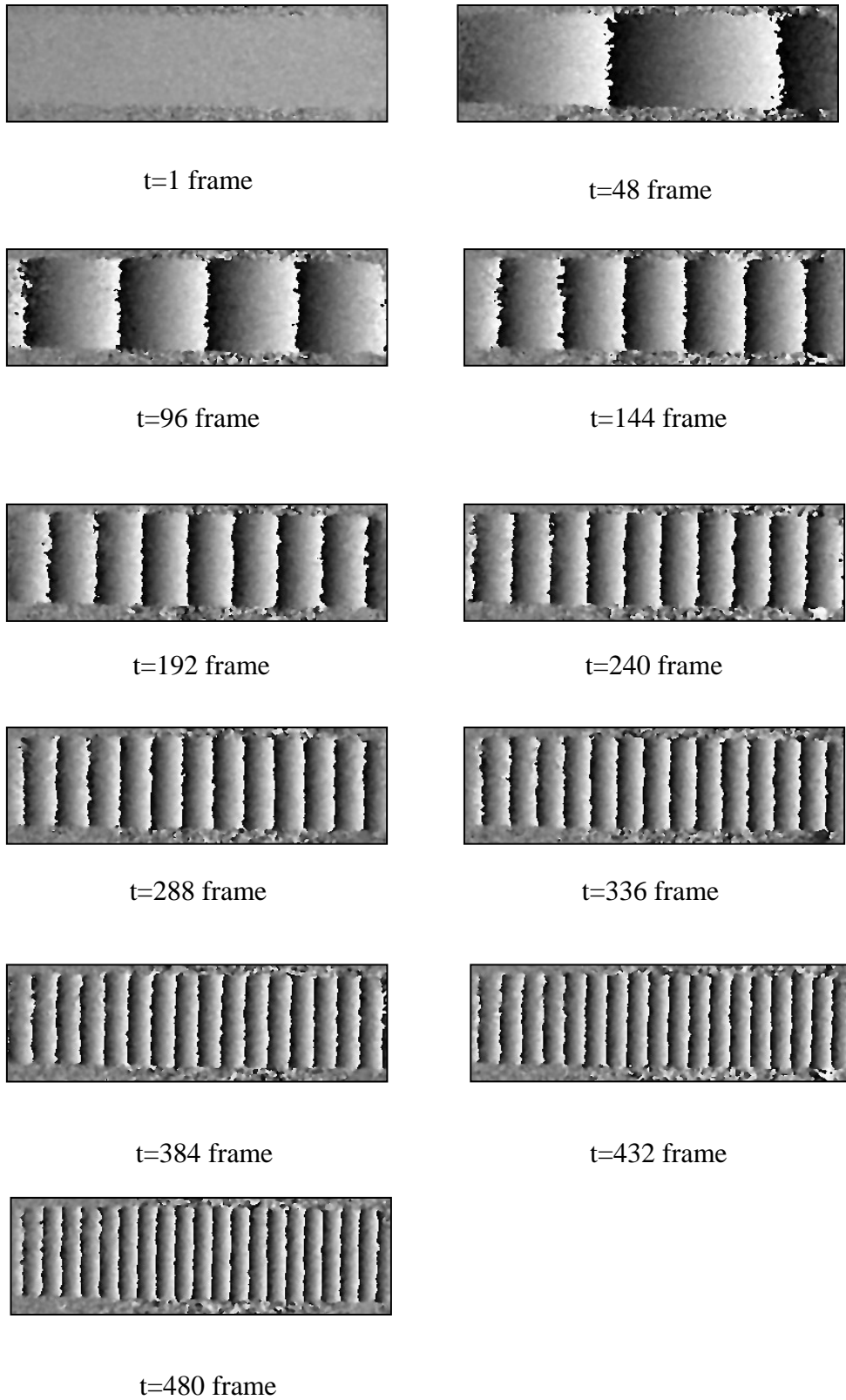


Figure 5.22 Interference phase variations with time

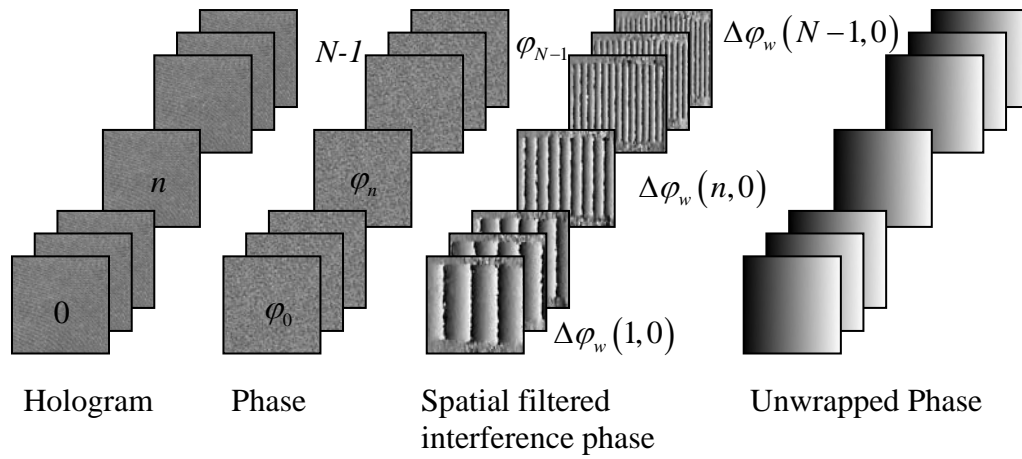


Figure 5.23 Schematic description of temporal phase unwrapping of digital holograms

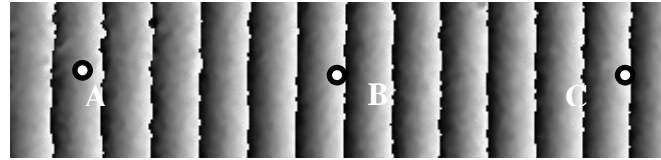


Figure 5.24 A typical interference phase pattern of the cantilever beam

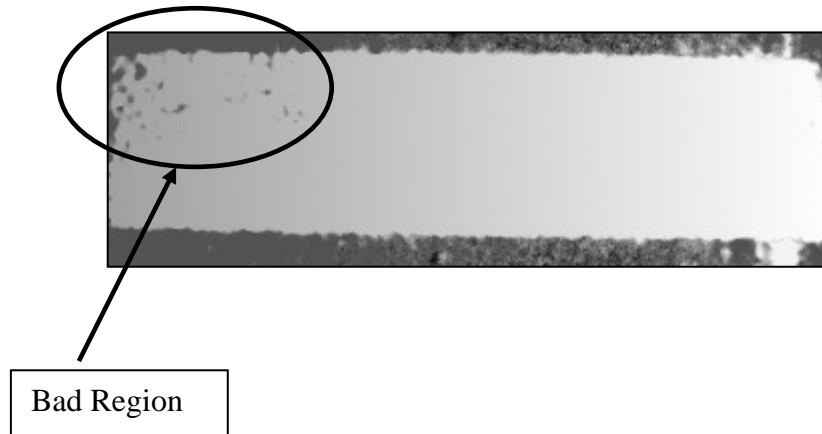


Figure 5.25 Unwrapped phase by DPS method

Numerical differentiation is a commonly used method to obtain the first derivative (instantaneous frequency) of a signal in signal processing. In this study, the first derivative of interference phase of a particular pixel along the time axis is calculated by numerical differentiation:

$$\Delta\varphi'(n) = \Delta\varphi_u(n+1) - \Delta\varphi_u(n) \quad (5.1)$$

where u denotes unwrapped phase. A calibration is needed before the unwrapped interference phase can be changed to the measured physical quantity. For the experimental configuration illustrated in Figure 4.10, the out-of-plane displacement of a particular pixel at each instant t can be calculated with good accuracy (Wagner et al., 1999):

$$d_z(t) = \frac{\lambda\Delta\varphi(t)}{4\pi\cos(\theta/2)} \quad (5.2)$$

where θ is the angle between the illumination and the observation direction. The out-of-plane instantaneous velocity $v_z(t)$ can be expressed as

$$v_z(t) = d'_z(t) = \frac{\lambda\Delta\varphi'(t)}{4\pi\cos(\theta/2)} \quad (5.3)$$

The angle θ employed in experiment is 60° and a constant $k = \lambda/4\pi\cos(\theta/2) = 0.058$ is obtained to calibrate the experimental result. Figure 5.26 (a) shows the instantaneous velocity variation of point B by numerical differentiation of unwrapped interference phase from DPS method. It is seen that the result is in such a mess that no evaluation can be done.

In the proposed ridge extraction algorithm, a sequence of complex phasor maps is first obtained after all the digital holograms are reconstructed. For each pixel, the instantaneous frequency as a function for the sequence of complex phasors is calculated by ridge extraction algorithm. The unwrapped interference phase is then obtained by integration. The process flow is shown in Figure 5.27.

Instantaneous velocities for point A, B, C calculated by the proposed ridge extraction algorithm are given in Figure 5.26 (b). A much better result is obtained and all three points have the same trend with time. Such a result again shows the effectiveness of the proposed method. It offers the possibilities which can not be obtained by conventional method. The window sizes for Point A, B and C are 15.4, 13.4 and 11.5 pixels, respectively.

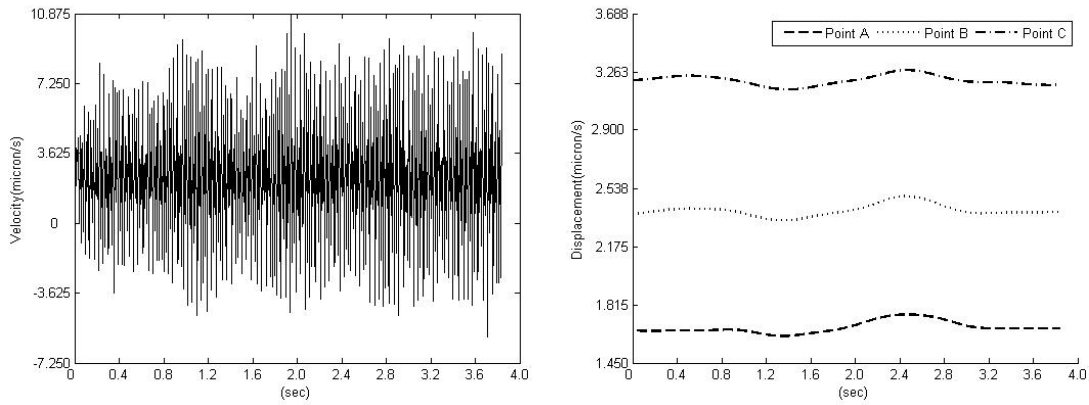


Figure 5.26 (a) Instantaneous velocity of point *B* using numerical differentiation of unwrapped phase difference; (b) Instantaneous velocity of points *A*, *B* and *C* by proposed ridge algorithm

The 2D distribution and 3D plots of instantaneous velocity at different time instants are shown in Figure 5.28.

A change of Eq.(5.1) is as follows:

$$\Delta \varphi'(n) + \Delta \varphi_u(n) = \Delta \varphi_u(n+1) \quad n = 0, 1, \dots, N-1 \quad (5.4)$$

with $\Delta \varphi_u(0) = 0$. Eq. (5.4) is nothing but numerical integration. Thus the phase unwrapping is avoided by integration of the derivatives. The integration of the instantaneous velocity of a given pixel produces displacement. Displacements distribution of point B calculated by both CP and DPS methods are demonstrated in Figure 5.29. In order to observe the results in more detail, displacement variation from

time 0.4s to 0.8s is selected to display. As shown in Figure 5.29(b), the displacement variation calculated by DPS method is full of noise, not as expected straight line at all. This also explains why the result of Figure 5.26 is so poor. The proposed method, however, gives a greatly improved result as shown in Figure 5.29 (d).

Although temporal phase unwrapping method is able to prevent the ill-behaved pixels from spatial propagation, it brings along the problem of propagation of bad data along the time axis. As shown in Figure 5.30 (b), (d) and (f), the accumulation of interference phase errors along the time axis could result in an unbearable error in the region where the signal-to-noise ratio (SNR) is very low. Another observation is that the surface of the cantilever beam by DPS method is becoming smoother with the numbers of interference maps. Therefore, it is hard to get a satisfactory result for interference maps at early stages. However, the surfaces by CP method of different instants are all nearly the same smooth. It therefore offers another possibility to give a good result for any time instance.

5.3.3 A comparison of three temporal CP algorithms

Temporal Fourier transform algorithm has fewer real applications compared to the other two algorithms, since it has a restriction of linear phase changing. However, it plays an important role in the other two algorithms. As already discussed, a Fourier transform is needed to determine the integration limits for temporal STFT filtering algorithm. If temporal Fourier transform algorithm is employed, more precise integration limits are to be expected. Temporal ridge extraction algorithm actually shares the same principle as temporal Fourier transform algorithm. The temporal ridge extraction algorithm is able to pick up the peak of a locally transformed signal while

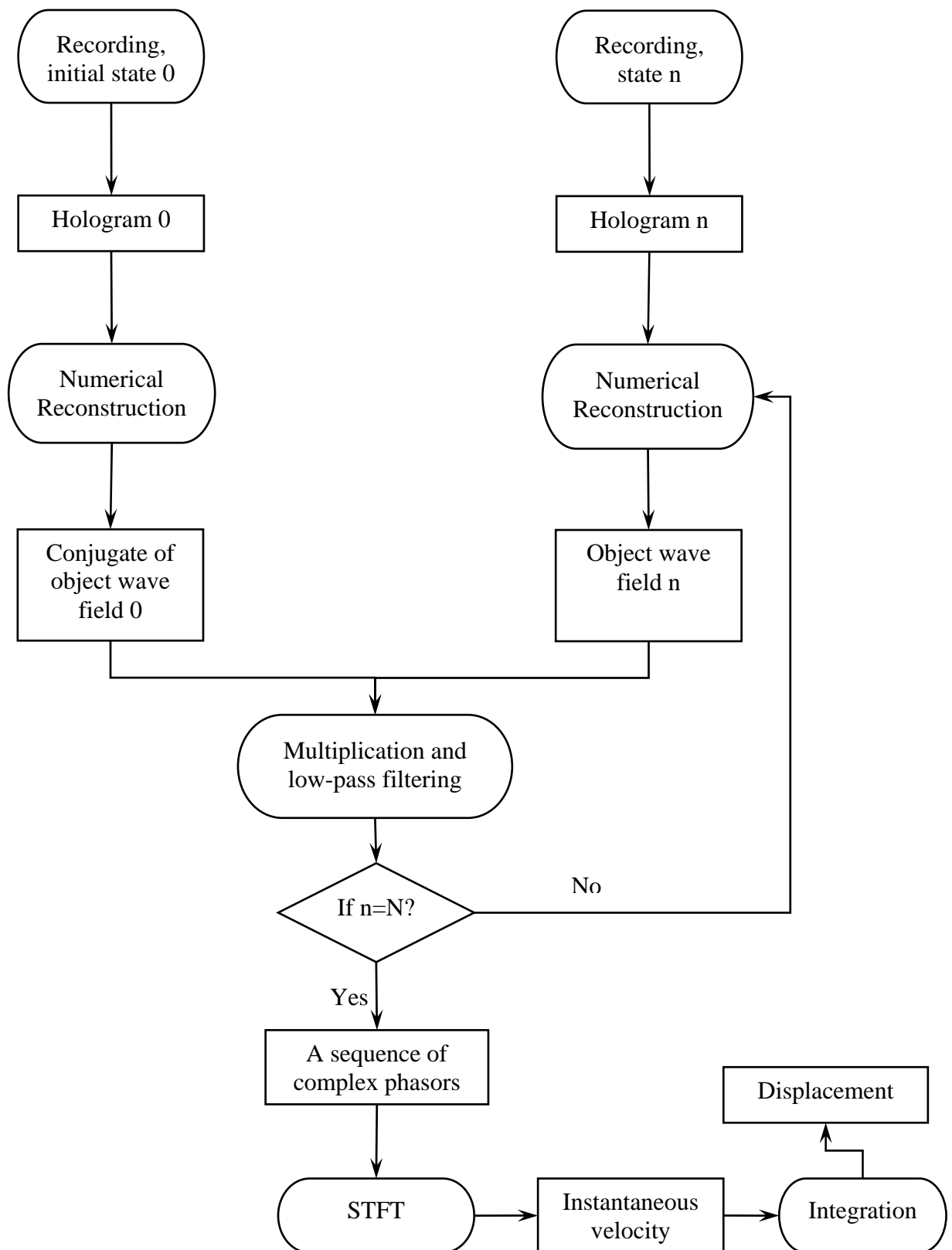


Figure 5.27 Flow chart of instantaneous velocity calculation using CP method

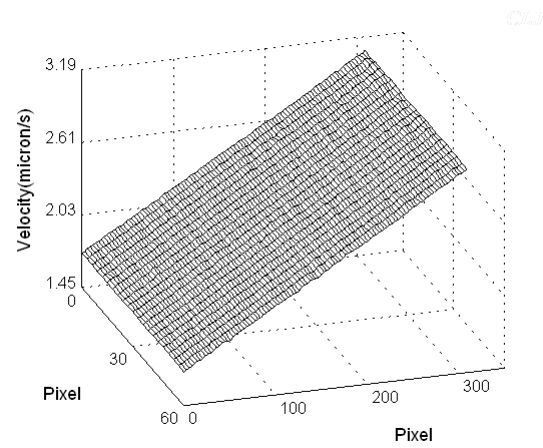
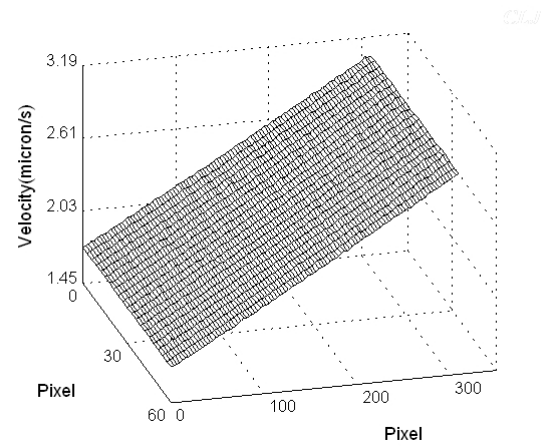
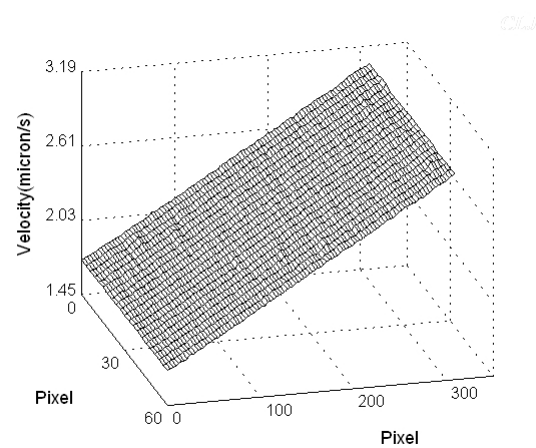
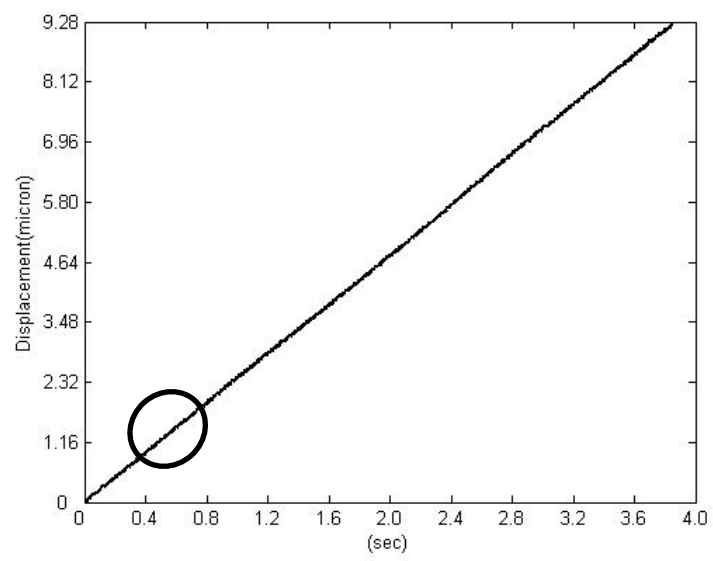
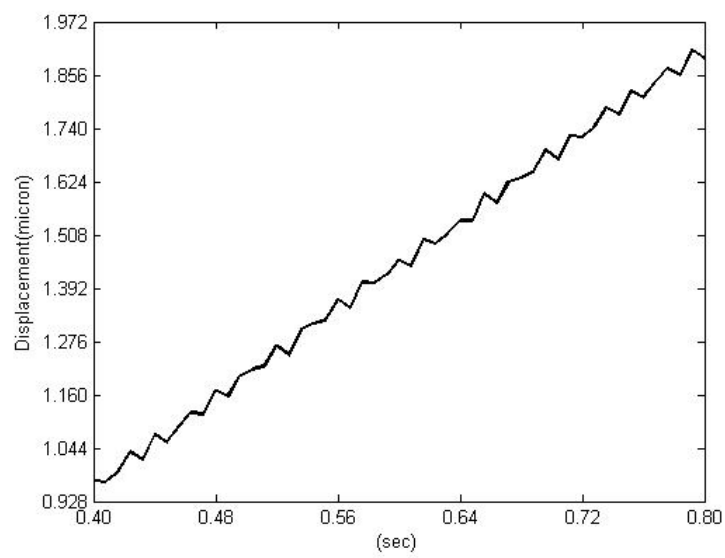
(a) $t = 0.8\text{s}$ (b) $t = 2.0\text{s}$ (c) $t = 3.2\text{s}$

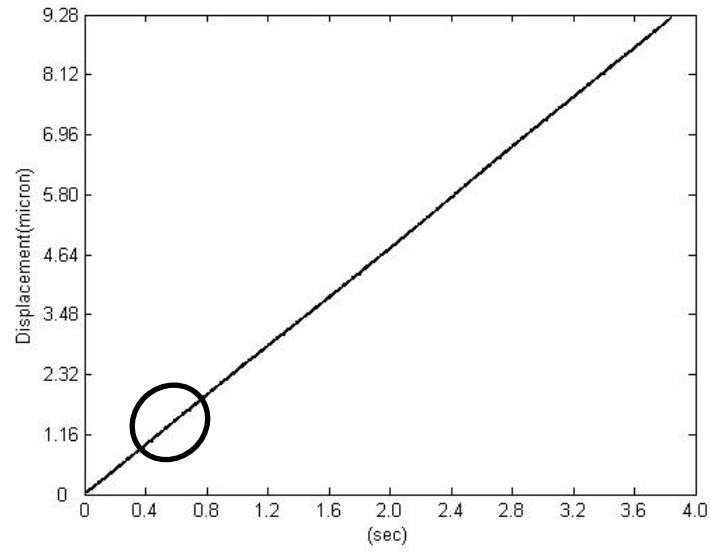
Figure 5.28 2D distribution and 3D plots of instantaneous velocity at various instants



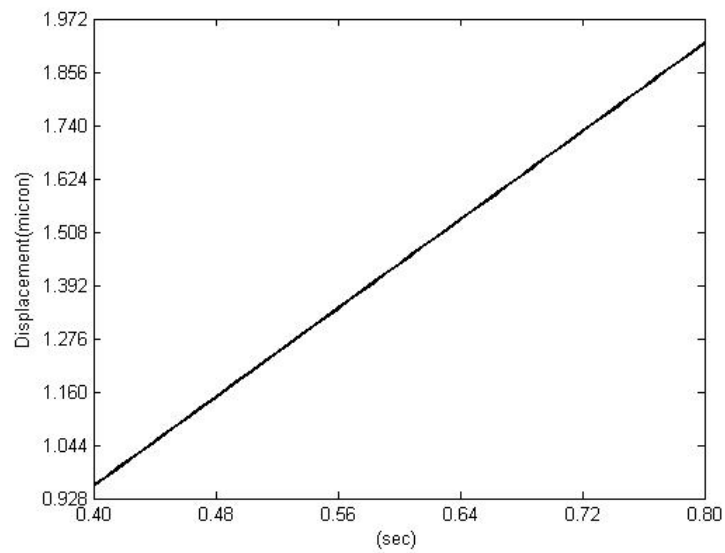
(a)



(b)



(c)



(d)

Figure 5.29 Displacement of point B: (a) by temporal phase unwrapping of wrapped phase difference using DPS method; (b) by temporal phase unwrapping of wrapped phase difference from $t = 0.4\text{s}$ to $t = 0.8\text{s}$ using DPS method; (c) by integration of instantaneous velocity using CP method; (d) by integration of instantaneous velocity from $t = 0.4\text{s}$ to $t = 0.8\text{s}$ using CP method

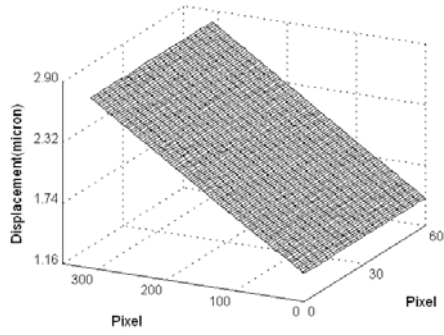
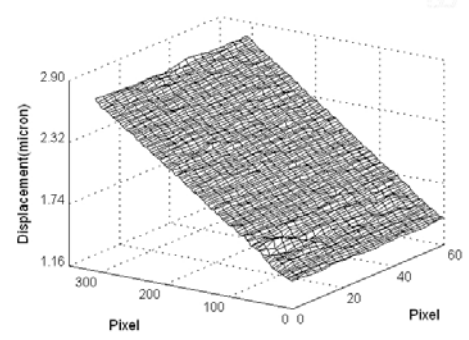
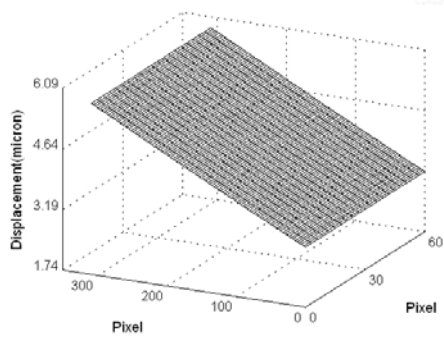
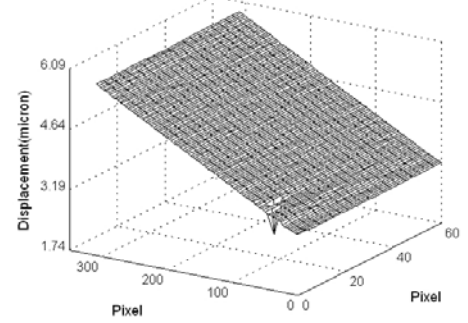
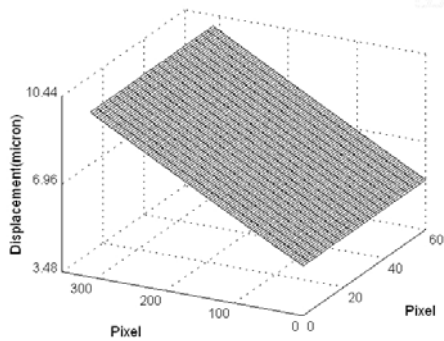
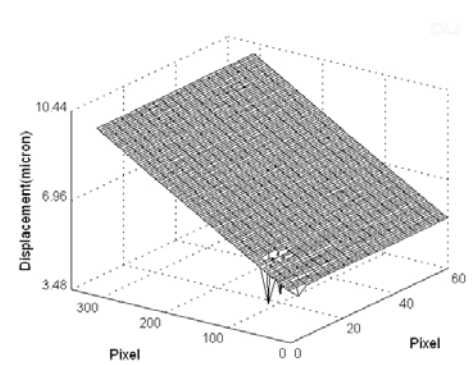
(a) $t = 0.8s$ (b) $t = 0.8s$ (c) $t = 2.0s$ (d) $t = 2.0s$ (e) $t = 3.2s$ (f) $t = 3.2s$

Figure 5.30 3D plot of displacement distribution at various instants. (a), (c), (e) by integration of instantaneous velocity using CP method; (b), (d), (f) by temporal phase unwrapping using DPS method

temporal Fourier transform algorithm only picks up the global peak.

In terms of phase retrieval, temporal STFT filtering algorithm is more suitable than temporal ridge extraction algorithm. There is no such need to consider the uncertainty relationship in temporal STFT filtering algorithm as in temporal ridge extraction algorithm, for it is just a transformation and inverse transformation process. Choosing a proper window is critical for temporal ridge extraction algorithm. How to choose a window is still a hot research topic in signal processing. By integration of the derivatives of interference phase whose window may not be so proper, there is a high chance to obtain a wrong unwrapped phase.

If it is the instantaneous frequency that is needed to measure, temporal ridge extraction algorithm is then the only choice. It offers more attracting possibilities than conventional methods as long as the right choice of time-frequency distribution is made.

Temporal Fourier transform algorithm takes shorter time to execute than the other two algorithms while temporal ridge extraction algorithm takes the longest. All of the programs are executed using Visual C++. If other platforms are employed, the calculation time will be unbearable. A table to show these comparisons is given in Table 5.1.

Table 5.1 A comparison of different temporal algorithms from CP concept

Algorithms	Applications	Calculation burden
Temporal Fourier transform	Fewest	Lightest
Temporal STFT filtering	Suitable for phase retrieval	bearable
Temporal ridge extraction	Instantaneous frequency calculation	Heaviest

CHAPTER SIX

CONCLUSIONS AND FUTURE WORK**6.1 Conclusions**

The main goal of this thesis is to develop new temporal phase analysis approaches permitting more precise measurement in non-static conditions, using digital holographic interferometry. Digital holography offers direct access of the phases of the reconstructed wave, avoiding the troublesome experimental efforts like phase-shifting or carrier technique. Thus it's nearly perfect for the area of dynamic measurement, for each state needs only one recording. The popular approach is to record a sequence of digital holograms during the whole process. Each interference phase distribution is then obtained from the complex reconstructed wave field. The temporal phase unwrapping is carried out along the time axis to get absolute and continuous phase. Such an approach offers the simplest way for dynamic measurement. However, the interference phase of each pixel is given an equal weight when processed without considering the reliability at all. Due to the much shorter exposure time and the electrical noise in dynamic measurement, lower signal-to-noise ratio usually exists. It's quite necessary to propose another processing method to retrieve high quality interference phase. **In this study, a complex phasor method to utilize the intensity and phase information simultaneously is proposed, in which the intensity acts a good measure of the phase value.** The most obvious advantage of processing complex phasors is that the more powerful tools such as Fourier transform or short

time Fourier transform can be employed while at the same time overcoming sign ambiguity.

Under the concept of manipulating complex phasors, three temporal phase analysis techniques are developed in which the complex phasor of each pixel is measured and analyzed as a function of time. The first algorithm is based on Fourier transform while the rest two employs STFT. The first algorithm requires the phase to be linearly changing. It picks up the peak corresponding to the changing rate from the resulting spectrum. In the frequency domain, the noise and signal is well separated, therefore, a well-filtered effect is achieved. In order to overcome the constraint of interference phase linear dependent on time, the rest two algorithms are proposed. The STFT more adaptive to exponential field is a local transform, thus signal in one place will not affect signal of another place. The second algorithm transforms the signal into spectrum and eliminates the coefficient with low amplitude by setting them to 0, the filtered coefficients are transformed back.

One of the important characteristics of STFT is that the instantaneous frequency of a processed signal can be extracted through the ridge. This character is very useful in eliminating noise effect as it is able to separate the signal and noise frequencies at any instant. The third algorithm combines the first algorithm's principle and ridge algorithm to retrieve the first derivative of the interference phase. By integration the first derivative, the interference phase can be obtained without the need of phase unwrapping.

Several applications are presented using temporal complex phasor method: profiling of a surface with step change; velocity and deformation measurement on continuously deforming objects. From a comparison between CP method and DPS

method, it is observed that CP provides better results, especially when SNR is low. The CP method presents a highly noise immunity.

6.2 Future work

The main contribution of this study is the proposal of a novel concept for digital holographic interferometry: CP method. It offers more possibilities than the conventional DPS. Three algorithms developed in this study is just a case in point. In this study, the proposed algorithms have been applied to surface profiling and continuously deforming measurement. However, a more appealing application on vibration measurement has not been studied. The fixed window of the proposed algorithms to process such a complex signal appears not so effective. STFT with adaptive window width has always been a hot researched topic in signal processing. Thus adaptive STFT should have great potential to be applied in digital holographic interferometry. It's nearly possible to process all the problems encountered in digital holographic interferometric applications. Possible future areas can be studied:

1. A simulation can be conducted to verify the future developed algorithms. The propose CP method is only verified by experiments to be effective. Therefore, a simulation is complementary for the proposed method. The simulation includes: Hologram generation, hologram reconstruction, addition of various noises.
2. More complex experiments can be studied such as vibration. Periodic or non-periodic vibration should be studied respectively. Vibration with higher frequency is especially worth of studying, thus having a higher requirement on the processing method.

3. Spatial application of CP method can be tried. In the digital reconstruction process, an intensity distortion problem exists due to the fill factor of the CCD sensor, which can be compensated by a known function. But its effect on the CP method has not been studied. If the effect could be eliminated, a quite promising digital holographic shearography is then possible. It's quite flexible and more information can be retrieved.

REFERENCES

1. Bone, D. J. Fourier fringe analysis: the Two-dimensional phase unwrapping problem. *Appl. Opt*, **30**, pp.3627-3632. 1991.
2. Creath, K. Phase-shifting speckle interferometry. *Appl. Opt*, **24**, pp.3053-3058. 1985.
3. Creath, K., K.M. Crennell and K.J. Gasvik. *Interferogram Analysis: Digital fringe pattern measurement techniques*. Bristol, Philadelphia. Institute of Physics. 1993.
4. Delaprat, N., B. Escudie, P. Guillemain, R. Kronladn-Martinet, P. Tchamitchian and B. Torresani. Asymptotic wavelet and Gabor analysis: extraction of instantaneous frequencies. *IEEE Transactions on Information Theory*, **38**, pp.644-664. 1992.
5. Demetrakopoulos, T.H. and R. Mittra. Digital and optical reconstruction of images from suboptical diffraction patterns. *Appl. Opt*, **13**, pp.665-670. 1974.
6. Demoli, N., J. Mestrovic and I. Sovic. Subtraction digital holography. *Appl. Opt*, **42**, pp.798-804. 2003
7. Durak, L. and O. Arikan. Short-time Fourier transform: two fundamental properties and an optimal implementation. *IEEE Trans: Signal Processing*, **51**, pp.1231-1242. 2003.
8. Flynn, T. J. Two-dimensional phase unwrapping with minimum weighted discontinuity. *J. Opt. Soc. Am. A*, **14**, pp.2692-2701. 1997.
9. Fu, Y., C.J. Tay, C.G. Quan and H. M. Wavelet analysis of speckle patterns with a temporal carrier. *Appl. Opt*, **44**, pp.959-965. 2005.
10. Gabor, D. A new microscopic principle. *Nature*, **161**, pp.777-778. 1948.

-
11. Ghiglia, D. C., G. A. Mastin and L. A. Romero. Cellular-automata method for phase unwrapping. *J. Opt. Soc. Am. A*, **4**, pp.267-280. 1987.
 12. Ghiglia, D. C. and M. D. Pritt. Two-dimensional phase unwrapping. John Wiley & Sons, Inc. 1998.
 13. Goodman, J.W. Introduction to Fourier Optics. McGraw-Hill Companies, Inc., New York. Second Edition. 1996.
 14. Goodman, J.W. and R.W. Lawrence. Digital image formation from electronically detected holograms. *Appl. Phys. Lett*, **11**, pp.77-79. 1967.
 15. Goudemand, N. Application of dynamic phase shifting with wavelet analysis to electronic speckle contouring. *Appl. Opt*, **45**, pp.3704-3733. 2006
 16. Haines, K.A. and B.P. Hildebrand. Surface-deformation measurement using the wavefront reconstruction technique. *Appl. Opt*, **5**, pp.595-602. 1966.
 17. Haines, K.A. and B.P. Hildebrand. Interferometric measurements on diffuse surfaces by holographic techniques. *IEEE. Trans*, **15**, pp.149-161. 1966.
 18. Haines, K.A. and B.P. Hildebrand. Contour generation by wavefront reconstruction. *Phys. Lett*, **19**, pp.10-11. 1965.
 19. Hariharan, P. Optical Holography. Cambridge University Press, Cambridge. 1984.
 20. Heflinger, L.O. and R.F. Wuerker. Holographic contouring via multifrequency lasers. *Appl. Phys. Lett*, **18**, pp.28-30.1969.
 21. Hildebrand, B.P. and K.A. Haines. The generation of three-dimensional contour maps by wavefront reconstruction. *Phys. Lett*, **21**, pp.422-423. 1966.
 22. Horman, M.H. An application of wavefront reconstruction to interferometry. *Appl. Opt*, **4**, pp.333-336. 1965.
 23. Huntley, J. M. and H. O. Saldner. Temporal phase-unwrapping algorithm for automated interferogram analysis. *Appl. Opt*, **32**, pp.3047-3052. 1993.
-

-
24. Huntley, J.M., G.H. Kaufmann, D. Kerr. Phase-shifted dynamic speckle pattern interferometry at 1KHz. *Appl. Opt*, **38**, 6556-653. 1999.
 25. Joenathan, C, B. Franze, P. Haible, and H. J. Tiziani. Speckle interferometry with temporal phase evaluation for measuring large-object deformation. *Appl. Opt*, **37**, pp.2608–2614. 1998.
 26. Joenathan, C, B. Franze, P. Haible, and H. J. Tiziani. Large in-plane displacement measurement in dual-beam speckle interferometry using temporal phase measurement. *J. Mod.Opt*, **45**, pp.1975–1984. 1998.
 27. Just, D., N. Adam, M. Schwabisch and R. Bamler. Comparison of phase unwrapping algorithms for SAR interferograms. In *Proc. of the 1995 International Geoscience and Remote sensing symposium*. Firenze, Italy, July, 1995. pp.767-769.
 28. Kato, J, I. Yamcguchi, T. Matsumera. Multicolor digital holography with an achromatic phase shifter. *Opt. Lett*, **27**, pp.1403-1405. 2002.
 29. Klein, M.V. and T.E. Furtak. *Optics*. 2nd ed. Wiley, New York.
 30. Kreis, T. Digital holographic interference-phase measurement using the Fourier transform method. *J. Opt. Soc. Amer. A*, **3**, pp.847-855. 1986.
 31. Kreis, T. *Handbook of holographic interferometry: optical and digital methods*. Weinheim; [Great Britain]: Wiley-VCH. 2005.
 32. Kreis, T. and W. Jüptner. Principles of digital holography. In: Jüptner W, Osten W (eds) *Proc 3rd International Workshop on Automatic Processing Fringe Patterns*, Akademie, Berlin, 1997. pp.353-363.
 33. Lee, W.H. *Computer-generated Holograms: Techniques and Applications*. *Progress in Optics*, **16**, pp.120-232. 1978.
-

34. Liu, G and P.D. Scott. Phase retrieval and twin-image elimination for in-line Fresnel holograms. *J. Opt. Soc. Am. A*, **4**, pp.159-165. 1987.
35. Mallat, S. *A Wavelet Tour of Signal Processing*, 2nd ed., Academic: San Diego. 1999.
36. Onural, L and M.T. Ozgen. Extraction of three-dimensional object-location information directly from in-line holograms using Wigner analysis. *J. opt. Soc. Am. A*, **9**, pp.252-160. 1992.
37. Onural, L and P.D. Scott. Digital decoding of in-line holograms. *Opt. Eng*, **26**, pp.1124-1132. 1987.
38. Pedrini, G, P. Froning, P. Fessler, and H.J. Tiziani. Transient vibration measurements using multipulse digital holography. *Opt & Laser. Tech*, **29**, pp.505-511. 1997
39. Pedrini, G, P.H. Froening, H.J. Tiziani, and M.E. Gusev. Pulsed digital holography for high-speed contouring that uses a two-wavelength method. *Appl. Opt*, **38**, pp.3460–3467. 1999.
40. Pedrini, G, I. Alexeenko, W. Osten, and H.J. Tiziani. Temporal phase unwrapping of digital hologram sequences. *Appl. Opt*, **42**, pp.5846-5854. 2003.
41. Perez-Lopez, C, F.M. Santoyo, G. Pedrini, S. Schedin, H.J. Tiziani. Pulsed digital holographic interferometry for dynamic measurement of rotating objects with an optical derotator. *Appl. Opt*, **40**, pp.5106–5110. 2001.
42. Powell, R.L. and K.A. Stetson. Interferometric vibration analysis by wavefront reconstruction. *J. Opt. Soc. Am*, **55**, pp.1593-1598. 1965.
43. Priti, C., M. Giali, and N. Leuratti. SAR interferometry: A 2D phase unwrapping technique based on phase and absolute values information. *Proc. Of 1990*

-
- International Geoscience and Remote Sensing Symposium. IEEE. Piscataway, NJ. 1990. pp.2043-2046.
44. Robinson, D. W. and G. T. Reid. Interferogram analysis: digital fringe pattern measurement techniques. Bristol, Philadelphia. Institute of Physics. 1993.
45. Qian, Kemao. Windowed Fourier transform for fringe analysis. *Appl. Opt.*, **43**, pp.2695-2702. 2004.
46. Qian, Kemao . Two-dimensional windowed Fourier transform for fringe pattern analysis: Principles, applications and implementations. *Opt & Laser Technology*, **45**, pp.304-317. 2007.
47. Qian, Kemao, S.H. Soon, A. Asundi. A simple phase unwrapping approach based on filtering by windowed Fourier transform. *Opt & Laser Technology*, **37**, pp.458-462. 2005.
48. Schedin, S, G. Pedrini, H.J. Tiziani, A.K. Aggarwal, and M.E. Gusev. Highly sensitive pulsed digital holography for built-in defect analysis with a laser excitation. *Appl. Opt.*, **40**, pp.100–103. 2001.
49. Schnars, U. Direct phase determination in hologram interferometry with use of digitally recorded holograms. *J. Opt. Soc. Am. A*, **11**, pp.2011-2015. 1994.
50. Schnars, U and W. Jüptner. Direct recording of holograms by a CCD-target and numerical reconstruction. *Appl. Opt.*, **33**, pp.179-181. 1994.
51. Schnars, U and W. Jüptner. Digital Holography: Digital Hologram Recording, Numerical Reconstruction, and Related Techniques. New York: Springer. 2005.
52. Seebacher, S, W. Osten, W. Jüptner. Measuring shape and deformation of small objects using digital holography. *Proc. SPIE*, **3479**, pp.104-115.1998.
-

-
53. Sollid, J.E. and J.B. Swint. A determination of the optimum beam ratio to produce maximum contrast photographic reconstructions from double-exposure holographic interferograms. *Appl. Opt.*, **9**, pp.2717-2719. 1970.
54. Skarman, B, J. Becker, K, Wozniak. Simultaneous 3D-PIV and temperature measurements using a new CCD-based holographic interferometer. *Flow Measurement and Instrumentation*. **7**, pp.1-6. 1996.
55. Sweeney, D.W. and C.M. Vest. Reconstruction of three dimensional refractive index fields from multidirectional interferometric data. *Appl. Opt.*, **12**, pp.2649-2663. 1973.
56. Takaki, Y, H. Kawai and H. Ohzu. Hybrid holographic microscopy free of conjugate and zero-order images. *Appl. Opt.*, **38**, pp. 4990-4996. 1999.
57. Taketa, M, H. Ina and S. Kobayashi. Fourier-transform method of fringe-pattern analysis for computer-based topography and interferometry. *J. Opt. Soc. Am.*, **72**, pp.156-160. 1982.
58. Tonin, R and D.A. Bies. Analysis of 3-D vibration from time-averages holograms. *Appl.Opt.*, **17**, pp.3713-3721. 1978.
59. Vest, C.M. *Holographic Interferometry*. John Wiley and Sons. 1979.
60. Wagner, C, S. Seebacher, W. Osten and W. Jüptner. Digital recording and numerical reconstruction of lensless Fourier holograms in optical metrology. *Appl. Opt.*, **38**, pp.4812-4820. 1999.
61. Xu, Y, C.M. Vest, and J.D. Murray. Holographic interferometry used to demonstrate a theory of pattern formation in animal coats. *Appl. Opt.*, **22**, pp.3479-3483. 1983.
62. Xu, L, J. Miao and A. Asundi. Properties of digital holography based on in-line configuration. *Opt. Eng.*, **39**, pp. 3214-3219. 1999.
-

63. Yamaguchi, I and T. Zhang. Phase-shifting digital holography. *Opt. Lett*, **27**, pp.1108-1110. 1997.
64. Yamaguchi, I, J. Kato, S. Ohta, J. Mizuno. Image formation in phase-shifting digital holography and applications to microscopy. *Appl. Opt*, **40**, pp.6177-6186. 2001.
65. Yamaguchi, I, T. Matsumura, J. Kato. Phase shifting color digital holography. *Opt. Lett*, **27**, pp.1108-1110. 2002.
66. Yaroslavski, L.P., N.V. Merzlyakov and M.A. Kronrod. Reconstruction of holograms with a computer. *Sov. Phys. Tech. Rhys. USA*, **17**, pp.333-334. 1972.
67. Zhang, T and I. Yamaguchi. Three-dimensional microscopy with phase-shifting digital holography. *Opt. Lett*, **23**, pp.1221-1223. 1998.

APPENDIX

APPENDIX A SHORT TIME FOURIER TRANSFORM RIDGES

We start from the definition of analytic instantaneous frequency. A cosine modulation

$$f(t) = I_M \cos(\omega t + \varphi_0) = I_M \cos \varphi(t) \quad (\text{A.1})$$

has a frequency ω that is the derivative of the phase $\varphi(t) = \omega t + \varphi_0$. To generalize this notion, real signals f are written as an amplitude I_M modulated with a time varying phase φ :

$$f(t) = I_M(t) \cos \varphi(t) \quad \text{with} \quad I_M(t) \geq 0 \quad (\text{A.2})$$

The instantaneous frequency is defined as a positive derivative of the phase:

$$\omega(t) = \varphi'(t) \geq 0 \quad (\text{A.3})$$

The derivative can be chosen to be positive by adapting the sign of $\varphi(t)$. One must be careful because there are many possible choices of $I_M(t)$ and $\varphi(t)$, which implies that $\omega(t)$ is not uniquely defined relative to f .

In short time Fourier transform, the spectrogram $P_S f(b, \zeta) = |Sf(b, \zeta)|^2$ measures the energy of f in a time-frequency neighborhood of (b, ζ) . The ridge algorithm computes instantaneous frequencies from the local maxima of $P_S f(b, \zeta)$. The short time Fourier transform is computed with a symmetric window $g(t) = g(-t)$ whose support is equal to $[-1/2, 1/2]$. The Fourier transform \hat{g} is a real symmetric

function and $|\hat{g}(\omega)| \leq \hat{g}(0)$ for all $\omega \in R$. The maximum $\hat{g}(0) = \int_{-1/2}^{1/2} g(t) dt$ is on the order of 1. Generally, the window g is normalized so that $\|g\| = 1$. For a fixed scale a , $g_a(t) = a^{-1/2} g(t/a)$ has a support of size a and a unit norm. The corresponding windowed Fourier atoms are

$$g_{a,b,\zeta}(t) = g_a(t-b)e^{i\zeta t} \quad (\text{A.4})$$

and the windowed Fourier transform is defined by

$$Sf(b, \zeta) = \langle f, g_{a,b,\zeta} \rangle = \int_{-\infty}^{+\infty} f(t) g_a(t-b) e^{-i\zeta t} dt \quad (\text{A.5})$$

The following theorem relates $Sf(b, \zeta)$ to the instantaneous frequency of f .

Theorem

Let $f(t) = I_M(t) \cos \varphi(t)$. If $\zeta \geq 0$ then

$$\langle f, g_{a,b,\zeta} \rangle = \frac{\sqrt{a}}{2} I_M(b) \exp(i[\varphi(b) - b\zeta]) (\hat{g}(a[\zeta - \varphi'(b)]) + \varepsilon(b, \zeta)) \quad (\text{A.6})$$

The corrective term satisfies

$$|\varepsilon(b, \zeta)| \leq \varepsilon_{I,1} + \varepsilon_{I,2} + \varepsilon_{\varphi,2} + \sup_{|\omega| \geq a\varphi'(b)} |\hat{g}(\omega)| \quad (\text{A.7})$$

with

$$\varepsilon_{I,1} \leq \frac{a|I'_M(b)|}{|I_M(b)|}; \quad \varepsilon_{I,2} \leq \sup_{|t-b| \leq a/2} \frac{a^2|I''_M(b)|}{|I_M(b)|} \quad (\text{A.8})$$

and if $a|I'_M(b)|I_M(b)^{-1} \leq 1$ then

$$\varepsilon_{\varphi,2} \leq \sup_{|t-b| \leq a/2} a^2 |\varphi''(t)| \quad (\text{A.9})$$

if $\zeta = \varphi'(b)$ then

$$\varepsilon_{I,1} = \frac{a|I'_M(b)|}{|I_M(b)|} |\hat{g}'(2a\varphi'(b))| \quad (\text{A.10})$$

The proof of above theorem is presented by Mallat (1998). Delprat et al. (1992) give a different proof of a similar result when $g(t)$ is a Gaussian, using a stationary phase approximation. If the corrective term $\varepsilon(b, \zeta)$ can be neglected, Eq. (A.6) enables us to measure $I_M(b)$ and $\varphi'(b)$ from $Sf(b, \zeta)$. This implies that the decomposition $f(t) = I_M(t) \cos \varphi(t)$ is uniquely defined. By reviewing the proof of the theorem mentioned above, one can verify that I_M and φ' are the analytic amplitude and instantaneous frequencies of f . Eqs. (A.8) and (A.9) show that the three corrective terms $\varepsilon_{I,1}$, $\varepsilon_{I,2}$ and $\varepsilon_{\varphi,2}$ are small if $I_M(t)$ and $\varphi'(t)$ have small relative variations over the support of the window g_a . Let $\Delta\omega$ be the bandwidth of \hat{g} defined by

$$|\hat{g}(\omega)| \ll 1 \quad \text{for } |\omega| \geq \Delta\omega. \quad (\text{A.11})$$

The term $\sup_{|\omega| \geq a\varphi'(b)} |\hat{g}(\omega)|$ of $\varepsilon(b, \zeta)$ is negligible if

$$\varphi'(b) \geq \frac{\Delta\omega}{a} \quad (\text{A.12})$$

Ridge Points of Short Time Fourier transform

Let us suppose that $I_M(t)$ and $\varphi'(t)$ have small variations over intervals of size a and $\varphi'(b) \geq \frac{\Delta\omega}{a}$ so that the corrective term $\varepsilon(b, \zeta)$ can be neglected. Since $|\hat{g}(\omega)|$ is maximum at $\omega=0$, Eq. (A.6) shows that for each b the spectrogram $|Sf(b, \zeta)|^2 = \left| \langle f, g_{a,b,\zeta} \rangle \right|^2$ is maximum at $\zeta(b) = \varphi'(b)$. The corresponding time-frequency points $(b, \zeta(b))$ are called *ridges*. At ridge points, Eq. (a.6) becomes

$$Sf(b, \zeta) = \frac{\sqrt{a}}{2} I_M(b) \exp(i[\varphi(b) - b\zeta]) (\hat{g}(0) + \varepsilon(b, \zeta)) \quad (\text{A.13})$$

Theorem above proves that the $\varepsilon(b, \zeta)$ is smaller at a ridge point because the first order term $\varepsilon_{I,1}$ becomes negligible in Eq. (A.10). This is shown by verifying that $|\hat{g}(2a\varphi'(b))|$ is negligible when $a\varphi'(b) \geq \Delta\omega$. At ridge points, the second order term $\varepsilon_{I,2}$ and $\varepsilon_{\varphi,2}$ are predominant in $\varepsilon(b, \zeta)$.

The ridge frequency gives the instantaneous frequency $\zeta(b) = \varphi'(b)$ and the amplitude is calculated by

$$I_M(b) = \frac{2|Sf(b, \zeta(b))|}{\sqrt{a}|\hat{g}(0)|} \quad (\text{A.14})$$

Let $\Phi_S(b, \zeta)$ be the complex phase of $Sf(b, \zeta)$. If we neglect the corrective term, the Eq. (A.13) proves that ridges are also points of stationary phase:

$$\frac{\partial \Phi_S(b, \zeta)}{\partial b} = \varphi'(b) - \zeta = 0 \quad (\text{A.15})$$

APPENDIX B C++ SOURCE CODE FOR TEMPORAL RIDGE ALGORITHM

```

void CTmpUnwrapping::WFRiges(fftw_complex *InputArray, double *dbRiges,
double dbSigma, double dbPrecision, double *dbIntensity, double dbscale)
{
    double* dbWindow=new double[iPoints];

    fftw_complex* ArrayforWFR=(fftw_complex*) fftw_malloc(sizeof(fftw_complex)
    * iPoints);

    for(int m=0;m<iPoints;m++)
    {
        double dbsum=0;

        for(int n=0;n<iPoints;n++)
        {
            double dbminus=(double)(n-m)/dbscale;
            double temp=-dbminus*dbminus/(2*dbSigma*dbSigma);

            dbWindow[n]=exp(temp)/sqrt(dbscale);
            dbsum=dbsum+dbWindow[n]*dbWindow[n];
        }

        dbsum=sqrt(dbsum);

        for(n=0; n<iPoints;n++)
        {
            ArrayforWFR[n][0]=InputArray[n][0]*dbWindow[n]/dbsum;
            ArrayforWFR[n][1]=InputArray[n][1]*dbWindow[n]/dbsum;
        }

        double dbTemp=DBrent(ArrayforWFR,iPoints,0.00001);

        double dbTmpIntn;

        CaculateParameters(ArrayforWFR,&dbTmpIntn,NULL,NULL,dbTemp,iPo
        ints);

        if((-dbTmpIntn)>dbIntensity[m])
        {
            dbRiges[m]=2*Pai*dbTemp/iPoints;
            dbIntensity[m]=-dbTmpIntn;
        }
    }
}

```

```

    }
}

```

```

double CTmpUnwrapping::DBrent(fftw_complex* InputArray,unsigned int N,const
double tol)
{

```

```

    double iInitialGuess=AInitialGuess(InputArray);

```

```

    if(iInitialGuess>=N/2)
        iInitialGuess=iInitialGuess-N;

```

```

    const int ItMax=100;

```

```

    const double ZEPS=numeric_limits<double>::epsilon()*1.0e-3;

```

```

    bool ok1,ok2;

```

```

    int iter;

```

```

    double a,b,d=0.0,d1,d2,du,dv,dw,dx,e=0.0,ax,bx,cx;

```

```

    double fu,fv,fw,fx,ddfx,olde,tol1,tol2,u,u1,u2,v,w,x,xm;

```

```

    ax=(double)iInitialGuess-1;

```

```

    bx=(double)iInitialGuess;

```

```

    cx=(double)iInitialGuess+1;

```

```

    a=(ax<cx ? ax:cx);

```

```

    b=(ax>cx ? ax:cx);

```

```

    x=w=v=bx;

```

```

    CaculateParameters(InputArray,&fx,&dx,&ddfx,bx,N);

```

```

    fw=fv=fx;

```

```

    dw=dv=dx;

```

```

    for(iter=0;iter<ItMax;iter++)
    {

```

```

        xm=0.5*(a+b);

```

```

        tol1=tol*fabs(x)+ZEPS;
    }

```

```

tol2=2.0*tol1;

if(fabs(x-xm)<=(tol2-0.5*(b-a)))
    return x;

if(fabs(e)>tol1)
{
    d1=2.0*(b-a);
    d2=d1;
    if(dw!=dx) d1=(w-x)*dx/(dx-dw);

    if(dv!=dx) d2=(v-x)*dx/(dx-dv);

    u1=x+d1;

    u2=x+d2;

    ok1=(a-u1)*(u1-b)>0.0 && dx*d1<=0.0;

    ok2=(a-u2)*(u2-b)>0.0 && dx*d2<=0.0;

    olde=e;

    e=d;

    if(ok1||ok2)
    {
        if(ok1&&ok2)
            d=(fabs(d1)<fabs(d2)?d1:d2);
        else
        {
            if(ok1)
                d=d1;
            else
                d=d2;
        }

        if(fabs(d)<=fabs(0.5*olde))
        {
            u=x+d;
            if(u-a<tol2 || b-u< tol2)
                d=SIGN(tol1,xm-x);

        }
        else
        {
            d=0.5*(e=(dx>=0.0?a-x:b-x));
        }
    }
}

```

```

        else
        {
            d=0.5*(e=(dx>=0.0?a-x:b-x));
        }
    }
else
{
    d=0.5*(e=(dx>=0.0?a-x:b-x));
}

if(fabs(d)>=tol1)
{
    u=x+d;
    CaculateParameters(InputArray,&fu,NULL,NULL,u,N);
}
else
{
    u=x+SIGN(tol1,d);
    CaculateParameters(InputArray,&fu,NULL,NULL,u,N);
    if(fu>fx)
    {
        return x;
    }
}

CaculateParameters(InputArray,NULL,&du,NULL,u,N);
if(fu<=fx)
{
    if(u>=x)
        a=x;
    else
        b=x;
    mov3(v,fv,dv,w,fw,dw);
    mov3(w,fw,dw,x,fx,dx);
    mov3(x,fx,dx,u,fu,du);
}
else
{
    if(u<x)
        a=u;
    else
        b=u;
    if(fu<=fw || w==x)
    {
        mov3(v,fv,dv,w,fw,dw);
    }
}

```

```

        mov3(w,fw,dw,u,fu,du);
    }
    else if(fu<fv || v==x ||v==w)
    {
        mov3(v,fv,dv,u,fu,du);
    }
}
}
::MessageBox(NULL,"Cannot Find the real solution","Fatal Error!",MB_OK);
return 0.0;
}

double CTmpUnwrapping::TBP(fftw_complex *InputArray)
{
    double thetat,thetaf,dbT=0,dbsumxsqu=0,dbNumorator=0,dbB=0;

    for (int x=0;x<iPoints;x++)
    {
        double dbIntnofSig=InputArray[x][0]*InputArray[x][0] +
            InputArray[x][1]*InputArray[x][1];

        dbsumxsqu+=dbIntnofSig;
        double temp=x*dbIntnofSig;
        dbNumorator+=temp;

        dbT+=(x*temp);
    }

    thetat=dbNumorator/dbsumxsqu;

    dbT=dbT/dbsumxsqu;

    dbT=sqrt(dbT-thetat*thetat);

    dbNumorator=0;

    p=fftw_plan_dft_1d(iPoints,reinterpret_cast<fftw_complex*>(InputArray), \
        reinterpret_cast<fftw_complex*>(clxArrayOfOutput),FFTW_FORWARD,FF
        TW_ESTIMATE);

    fftw_execute(p);

    dbNumorator=0;

    int iHalf=iPoints/2;
    const double dbK=1/iPoints;

```

```
for (x=0;x<iPoints;x++)
{
    double iIndex;
    if(x<iHalf)
        iIndex=x;
    else
        iIndex=(double)x-iPoints;

    double dbItntfre=0;

    dbItntfre=clxArrayOfOutput[x][0]*clxArrayOfOutput[x][0]+clxArrayOf
    Output[x][1]*clxArrayOfOutput[x][1];

    double temp=iIndex*dbItntfre;
    dbNumerator+=temp;

    dbB+=(iIndex*temp);

}

thetaf=dbNumerator/(dbsumxsqu*iPoints*iPoints);

dbB=dbB/(dbsumxsqu*iPoints*iPoints*iPoints);

dbB=sqrt(dbB-thetaf*thetaf);

return sqrt(dbT/(dbB*Pai));

}
```

APPENDIX C LIST OF PUBLICATIONS DURING M.ENG PERIOD**Journal papers**

1. Chenggen Quan, Cho Jui Tay, and Hao Chen, “Temporal phase retrieval from complex field in digital holographic interferometry”, Optics Letters, **32**, pp.1602-1604. 2007.
2. H. Chen, C. Quan, C.J. Tay, “Instantaneous velocity measurement of dynamic deformation by digital holographic interferometry”, Optics Communications (In press)